POLITECNICO DI MILANO

School of Industrial and Information Engineering

Department of Physics

MSc in Engineering Physics

DEVELOPMENT OF A MAGNETIC ON-CHIP DIAGNOSTIC TEST FOR MALARIA

Supervisor:
Prof. Riccardo BERTACCO

Co-supervisor:
Marco GIACOMETTI
Dr. Marco MONTICELLI

Author:
Livia Beatrice CALLEGARI

ID Number:
851153

Contents

List of Figures

List of Tables

Abstract

Despite millions of people are infected by malaria every year, there is still a strong need of compact, low-cost and easy to use diagnosis system, allowing for a rapid and specific disease detection. This need is also reported in the guidelines of the World Health Organization (WHO) for malaria diagnosis: "WHO recommends prompt parasite-based diagnosis in all patients suspected of malaria before treatment is administered. Malaria rapid diagnostic tests have the potential to greatly improve the quality of management of malaria infections, especially in remote areas with limited access to good quality microscopy services."

This thesis project deals with the development of a lab-on-chip diagnostic test for malaria that combines magnetic separation and electrical impedance detection. Malaria parasite modifies the magnetic properties of infected red blood cells (RBCs) and produces characteristic hemozoin nanocrystals. These malaria biomarkers exhibit paramagnetic properties, allowing for magnetophoretic separation, both of isolated crystals and infected RBCs containing them, from the other blood components. The concept of the proposed diagnostic test is based on the specific attraction of hemozoin crystals and infected RBCs towards a chip surface, where they are detected by an electrical measurement. Long-range attraction is achieved with external permanent magnets, while a concentration on the electrodes occurs due to micrometric nickel pillars fabricated underneath. Then, since the presence of particles within a solution modifies its conductivity, the amount of hemozoin crystals and infected RBCs in the analyzed blood sample can be quantified through an impedance variation detection.

During this thesis, the feasibility of this detection device has been demonstrated. After an initial design and optimization phase, carried out with numerical simulations, a fabrication process for the device has been developed. Moreover, magnetic and electrical properties of hemozoin crystals have been characterized. Finally, preliminary magnetic capture experiments, performed on hemozoin crystals and modified red blood cells displaying a para-

magnetic behavior similar to that of infected ones, confirmed the possibility to efficiently capture and concentrate targeted particles. During another thesis project running in parallel, the feasibility of the impedance detection has been also experimentally demonstrated, down to the targeted limit of detection, for infected RBCs.

This thesis work is part of the TID MEKII project and has been realized under the supervision of Prof. Riccardo Bertacco, head of the *Nanomagnetism* group of the Department of Physics. Most of the experimental work has been carried out at *Polifab*, the micro- and nano-fabrication facility of Politecnico di Milano. The detection platform has been developed in collaboration with the $I\,^3N$ group of Politecnico di Milano leaded by Prof. Marco Sampietro, that performed design, fabrication and characterization of the electrical part. The bovine blood samples used in the experiments were provided and treated by $\mu BS\ Lab$ of Politecnico di Milano, leaded by Prof. Gianfranco B. Fiore.

Sommario

Nonostante milioni di persone vengano infettate ogni anno dalla malaria, tuttora c'è una forte necessità di sistemi diagnostici compatti, a basso costo e facili da utilizzare, in grado di rilevare in modo rapido e specifico la malattia. Tale necessità è riportata nelle linee guida per la diagnosi della malaria fornite dall'Organizzazione Mondiale della Sanità (OMS): "L'OMS raccomanda una diagnosi tempestiva e mirata per tutti i pazienti in cui si sospetta l'infezione malarica prima della somministrazione del trattamento. I test diagnostici rapidi per la malaria hanno il potenziale per migliorare notevolmente il modo in cui vengono gestite le infezioni legate a questa malattia, specialmente nelle aree isolate con accesso limitato a microscopi di buona qualità."

Questo progetto di tesi si occupa dello sviluppo di un test diagnostico miniaturizzato per la malaria, in cui si combinano separazione magnetica e rilevazione tramite una misura di impedenza elettrica. Il parassita responsabile la malaria modifica le proprietà magnetiche dei globuli rossi infetti a causa della formazione di un nano-cristallo caratteristico, l'emozoina, che funge da indicatore della malaria. L'emozoina mostra proprietà paramagnetiche, rendendo possibile una separazione magnetoforetica dei cristalli stessi o dei globuli rossi infetti che li contengono dagli altri componenti del sangue. L'idea del sistema diagnostico proposto è basata su un'attrazione specifica di cristalli di emozoina e globuli rossi infetti verso la superficie di un chip, su cui vengono rilevati con degli elettrodi. L'attrazione a lungo raggio è ottenuta con magneti permanenti esterni, mentre la concentrazione sugli elettrodi avviene grazie a dei pilastri micrometrici di nichel fabbricati al di sotto dei contatti elettrici. La presenza di particelle all'interno di una soluzione ne modifica la conducibilità, rendendo possibile la misura della quantità di cristalli di emozoina e globuli rossi infetti presenti nel campione di sangue analizzato, attraverso una misura della variazione di impedenza elettrica.

Durante il lavoro di tesi è stata dimostrata la possibilità di realizzare un dispositivo diagnostico di questo tipo. Dopo una fase iniziale di progettazione e ottimizzazione, svolta con l'ausilio di simulazioni numeriche, è stato sviluppato un processo di fabbricazione per realizzare il dispositivo. Inoltre, sono state caratterizzate le proprietà magnetiche ed elettriche dei cristalli di emozoina. Infine, sono stati svolti esperimenti preliminari di cattura magnetica, utilizzando sia cristalli di emozoina che globuli rossi trattati in modo da mostrare un comportamento paramagnetico simile a quello delle cellule infette. I risultati sperimentali hanno confermato la capacità del dispositivo di catturare e concentrare efficacemente le cellule modificate e i nano-cristalli. Durante un altro progetto di tesi svolto in parallelo, è stata dimostrata la capacità del dispositivo di svolgere un'efficace rilevazione elettrica, raggiungendo il livello di sensibilità prefissato, per quanto riguarda i globuli rossi infetti.

Questa tesi è parte del progetto TID MEKII ed è stata realizzata sotto la supervisione del Prof. Riccardo Bertacco, responsabile del gruppo di *Nanomagnetismo* del Dipartimento di Fisica. La maggior parte del lavoro sperimentale è stata svolta presso *Polifab*, la facility di micro- e nano-fabbricazione del Politecnico di Milano. La piattaforma di rilevazione è stata sviluppata in collaborazione con il gruppo I^3N del Politecnico di Milano, guidato dal Prof. Marco Sampietro, che si è occupato di progettare, fabbricare e caratterizzare le componenti elettriche del dispositivo. I campioni di sangue bovino usati durante gli esperimenti sono stati forniti e trattati dal *μBS Lab* del Politecnico di Milano, guidato dal Prof. Gianfranco B. Fiore.

Chapter 1

Introduction

1.1 Malaria: pathogenesis and social impact

Malaria is a life-threatening disease caused by protozoan parasites of the genus *Plasmodium* that are transmitted to people through the bites of infected female *Anopheles* mosquitoes[1,2]. Five parasite species are reported for their infections in humans, namely, *Plasmodium falciparum* (the most virulent and fatal species), *Plasmodium vivax*, *Plasmodium malariae*, *Plasmodium ovale* and *Plasmodium knowlesi*[1]. According to World Health Organization (WHO), 3.2 billion people are at risk for malaria and among them 1.2 billion are at high risk[2–4]. In 2015, 212 million new cases and 429000 deaths were estimated[2,3]. Approximately 90% of these deaths occurred in sub-Saharan Africa and over 70% were of children under 5 years[2,3]. Malaria distribution around the world according to data presented in WHO World Malaria Report 2014 is show in Figure 1.1.

However, increased efforts are dramatically reducing the disease burden in many places. Between 2010 and 2015, the rate of new cases among populations at risk fell by 21% globally[2]. In that same period, mortality rates among populations at risk fell by 29% globally among all age groups and by 35% among children under 5 years[2]. Unfortunately, despite these improvements malaria still remains endemic in 91 countries and territories[2]. Great efforts need to be done not only to prevent disease diffusion and treat infected people, but also to develop proper diagnostic systems. Indeed, treatment in the early stage of the disease is usually very effective, but diagnostic tests currently available are not able to guarantee a completely successful screening of the population. On the other hand, the over-treatment of the disease due to false positives in some diagnostic tests (especially RDTs, see section 1.2.1) may increase the risk of drug resistance of the parasite.
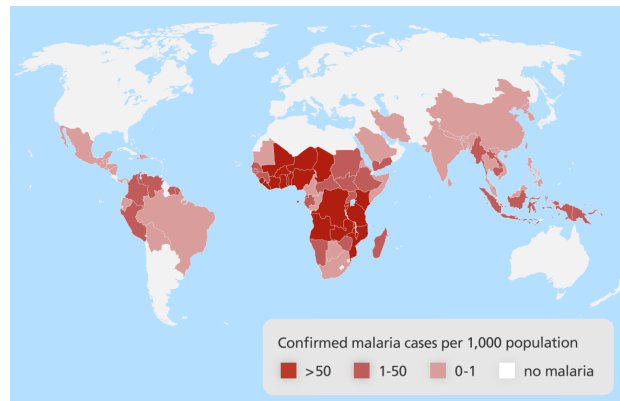
Figure 1.1: Map that shows the distribution of malaria around the world, according to the data presented in World Malaria Report 2014 [5].

1.1.1 Disease development and treatment

Human malaria occurs by transmission of *Plasmodium* sporozoites via a bite from an infected *Anopheline* mosquito. The *sporozoites* travel in the bloodstream, moving from the salivary glands of the mosquito to the liver of the host, where they invade hepatocytes. Within these cells the sporozoites transform and multiply via asexual reproduction (hepatic schizogony) until mature tissue *schizonts* are formed, each containing thousands of daughter *merozoites*. This initial stage is asymptomatic. After 6-8 days of development, depending on the *Plasmodium* species, fully mature liver schizonts rupture their host hepatocytes to release merozoites into the bloodstream.

Then, merozoites invade red blood cells (RBCs) to perpetuate the asexual life cycle (erythrocytic schizogony or asexual stage). This phase of the infection lasts 24–72 hours depending on the parasite species and is characterized by three stages: *ring form* (due to the characteristic appearance of the parasite), *trophozoite* and *schizont*. In this period the first symptoms associated with the malaria attack (such as fever, headache and chills) appear. During the intra-erythrocytic development, the parasite degrades hemoglobin (the principal component of red blood cells) inside its digestive vacuole. This process leads to parasite growth and asexual replication, while accumulating free heme. This molecule, highly toxic to the parasite, is converted in an insoluble form, known as *hemozoin* or malaria pigment. Actually, the parasite digests the erythrocyte hemoglobin not only for nutrition or detoxification purposes, but also in order to prevent RBCs from early lysis, which could take place if the parasite did not offset the increase in cells volume [6].
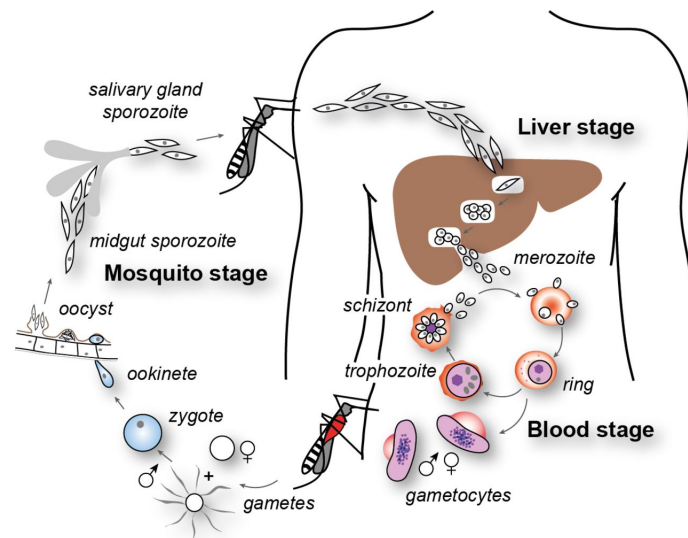
Figure 1.2: Main steps of the malaria parasite evolution inside humans and mosquitoes [10].

Many merozoites accumulate inside an infected RBC and, when it ultimately ruptures, they are released into the bloodstream and infect other erythrocytes. Some of the merozoites circulating in the blood will develop into male and female *gametocytes*, that can be ingested by a female mosquito during a blood meal on the infected human. Gametocytes enable sexual reproduction to occur in the mosquito midgut, producing sporozoites that accumulate in the mosquito salivary glands (sporogonic cycle) [4,6–9]. The main steps of the parasite evolution are represented in Figure 1.2.

Since the disease is spread by mosquitoes, the main approach used to prevent and reduce malaria transmission is vector control, whose most effective forms are the use of insecticide-treated mosquito nets and indoor residual spraying of insecticides. In addition, preventive treatment strategies with some antimalarial drugs are advisable for the most vulnerable groups, i.e. pregnant women, infants and children under 5 years [2]. Nowadays the best available therapy, particularly for *P. falciparum* malaria, is artemisinin-based combination therapy (ACT); it replaced the previous generations of medicines, such as chloroquine and sulfadoxine-pyrimethamine (SP), after a resistance of the parasites to these drugs spread in the 1950s [2]. Unfortunately, resistance to antimalarial medicines is a recurring problem. Indeed, in recent years, parasite resistance to artemisinin has been detected in five countries of the Greater Mekong subregion [2,11]. Therefore, research efforts are needed to find alternative treatments for malaria that avoid the prob-

lem of drug resistance altogether. One approach for the development of new treatments against malaria is to study the *Plasmodium* distinctive molecule hemozoin. Indeed, since sequestration of heme into hemozoin is an essential process in the malaria *Plasmodium* lifecycle, this molecule has become an attractive target for new drugs that could interfere with the biocrystallization of hemozoin and would help fighting the disease [12,13].

1.1.2 Malaria pigment

Because of its importance to the parasite survival inside the erythrocyte, hemozoin has been the subject of intensive physico-chemical and crystal studies. Hemozoin, which appears as a set of rod-like shaped black-brown crystals, has a crystal structure identical to that of a synthetic biomineral, β-hematin, as indicated by spectroscopic and crystallographic analyses [14]. However, there are differences between synthetic and natural hemozoin: while natural hemozoin is composed of smaller crystals measuring 50-500 nm, synthetic β-hematin crystals can range from 50 nm to 20 μm, depending on the solvent used to form them [6]. SEM images of natural hemozoin and β-hematin crystals are shown in Figure 1.3, together with a scheme of hemozoin chemical structure.
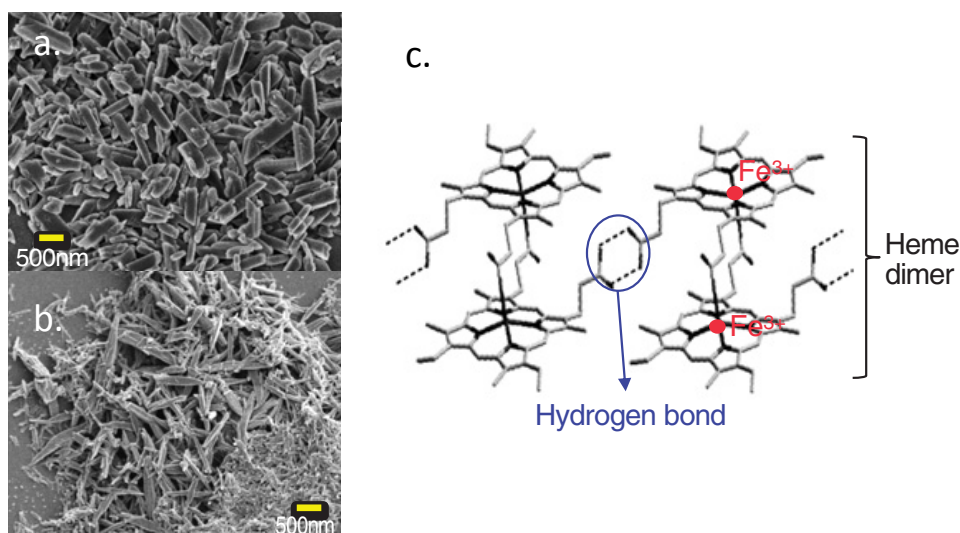
Figure 1.3: a. SEM picture of purified natural hemozoin crystals from *P.falciparum.* **b.** SEM picture of synthetic β-hematin crystals, purified from ultra-pure hemin chloride. **c.** Chemical structure of hemozoin crystals [15].

Hemozoin consists of a polymer of heme groups linked by bonds between the oxygen from the carboxylate ($RCOO^-$) of one heme and the central ferric ion (Fe^{3+}) of the next heme; these dimers are then aggregated into an ordered insoluble crystal by hydrogen bonds[6,16]. The process that yields to hemozoin production modifies the valence of Fe atoms, thus causing a relevant change in magnetic properties. Indeed, Fe^{2+} present in oxyhemoglobin has no unpaired electrons and is diamagnetic[17], while Fe^{3+} in hemozoin has five unpaired electrons per heme group and is paramagnetic[6,16,18–20]. So a transformation of Fe atoms from a low-spin state (S=0) to a high-spin state (S=5/2) occurs. Hemozoin crystals exhibit also optical dichroism, i.e. they absorb light more strongly along their length than across their width. Indeed, the anisotropic crystal structure of hematin leads to anisotropy in its refractive index, causing light to propagate differently through the crystal, depending on the propagation direction relative to the crystal lattice[6].

As mentioned in section 1.1.1, during the intra-erythrocyte phase an increasing fraction of hemoglobin is converted to hemozoin, with a maximum final value around 80%[9,16]. Number and size of the hemozoin crystals inside a red blood cell depend on the stage of the parasite development, with the least amount detected in the ring stage and the highest in the schizont stage[9]. The presence of hemozoin crystals inside the erythrocyte not only modifies many of its chemical and mechanical properties (e.g. they reduce RBC cell membrane deformability[7]), but it also affects magnetic properties of the infected cell. Indeed, due to the presence of paramagnetic particles inside them, also erythrocytes containing parasites will have a paramagnetic behavior, more intense in the late-stage (trophozoites and schizonts) with respect to the early-stage (ring-stage) due to the different hemozoin content[9,21].

Magnetic properties of hemozoin crystals and infected RBCs (i-RBCs), which will be analyzed in more detail in section 2.2.2, have been and can be further exploited to separate these particles and concentrate them in a specific region, thus favoring a diagnosis of the disease, as discussed in the following section.

1.2   Methods for malaria diagnosis

Transmission prevention and disease treatment are not the only tools available against malaria, also an early and accurate diagnosis is fundamental. Available methods for disease detection involve the identification of malaria parasites or their antigens in patient blood. Although this may seem simple, the diagnostic efficacy is subjected to many factors, e.g. different forms

of the five *Plasmodium* species, different stages of erythrocytic schizogony, persisting viable or non-viable parasitemia (common mainly in endemic regions) and sequestration of the parasites in the deeper tissues (i.e. they accumulate in organs tissue and are not present in the peripheral blood normally tested)[22]. Moreover, the first symptoms of the disease usually appear 10–15 days after the infective mosquito bite and may be mild and difficult to recognize as due to malaria. Additionally, in areas where the disease is endemic, even asymptomatic infections can occur, since people may develop partial immunity. Detecting the disease can be difficult also where malaria is no longer endemic, since clinicians may be not familiar with it and forget to consider it among the potential diagnosis[22]. Thus, the nonspecific nature of its clinical signs and symptoms may result in over-treatment of malaria or non-treatment of other diseases in malaria-endemic areas, and misdiagnosis in non-endemic areas. However, if not treated in a short time, malaria (in particular if caused by *P. falciparum*) can progress to severe illness, often leading to death. Therefore, it is crucial to administer antimalarial drugs as soon as possible, but only if the disease is actually present. Despite WHO recommends that all cases of suspected malaria should be confirmed using parasite-based diagnostic tests before administering treatment, national surveys between 2013 and 2015 suggest approximately 31% of suspected malaria cases in sub-Saharan Africa were not verified with such tests, resulting in over-use of antimalarial drugs and poor disease monitoring[3].

Being able to perform an accurate, possibly pan-plasmodic and rapid detection would be a great improvement for this problem. Furthermore, considering the main malaria diffusion areas (Africa and tropical regions), where medical staff is often undertrained and underequipped, diagnostic systems should be also easy to use and low-cost in order to have the possibility of a widespread distribution. The conventional techniques currently in use for malaria diagnosis are microscopic detection using stained blood smears (the *gold standard*), Rapid Diagnostic Tests (RDTs) and Polymerase Chain Reaction (PCR). They will be presented in the next section, together with recently developed methods that exploit magnetic and optical properties of hemozoin crystals and infected erythrocytes to design different detection systems. Then, the new idea for a detection platform related to the TID MEKII project will be illustrated.
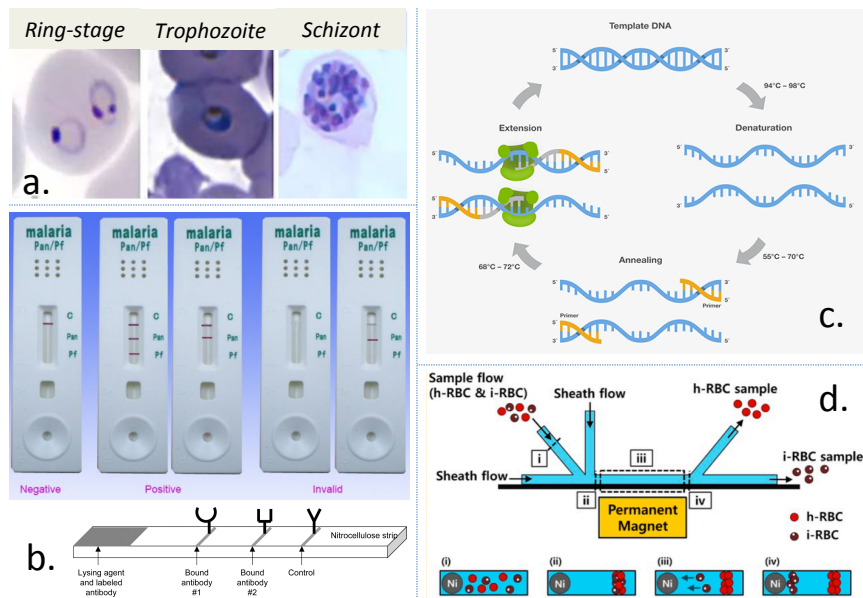
Figure 1.4: Examples of malaria diagnostic techniques. **a.** Optical microscope images of Giemsa-stained infected RBCs at different stages[1]. **b.** Photo of some real RDTs with different outcomes and a sketch of the working principle of the test[23]. **c.** General scheme of operation of PCR[24]. **d.** Schematic diagram of i-RBC separation with a HGMS technique[21].

1.2.1 State of the art and gold standard

Microscope detection

The *gold standard* for malaria diagnosis is the examination with an optical microscope of stained blood samples[25,26], usually coming from fingers or earlobes since parasite density is greater in capillary-rich areas[27]. Two different kinds of samples can be analyzed, thick and thin blood smears. The former provides enhanced sensitivity and is useful for quantification of malaria parasites, the latter is less sensitive but allows a much easier morphological identification of the species that are present[22,27]. Therefore, due to the different information provided by the two blood films, most laboratories involved in the quantification and identification of malaria parasites by microscopy analyze both of them[27]. The staining process, usually performed with Giemsa stain, can be complex and require up to 60 minutes[27]; stained i-RBCs at different stages are shown in Figure 1.4a. Then, diagnosis is performed counting parasites in different areas of the sample, although there is no accepted single standard method in current use by all investigators for the quantification[27,28].

Microscopic analysis is widely used because of its ability to diagnose and differentiate each species of malaria with a good sensitivity and in a relatively low-cost way, but it suffers from many drawbacks. Staining process and interpretation of the results are labor intensive, time consuming, and require considerable expertise and skillful well-trained healthcare workers, particularly for an accurate parasite identification at low parasitemia or in mixed malarial infections[4,22]. Low parasitemia can occur in the early stages of the disease development but also in later stages in case of *P.falciparum* infection, since parasites may be sequestered in deep capillaries (spleen, liver, bone marrow) and thus their equivalent number in the analyzed peripheral blood is reduced. Additionally, some *Plasmodium* species have a similar morphology, so a clear distinction may be difficult even for specialists. An expert microscopist with a proper equipment can detect up to 5–10 parasites/μl, but typically only 50–100 parasites/μl are detected, even less in limited resource settings[4,22]. Recently, some researchers[29,30] have introduced an image processing technique for microscopy that quantifies and classifies infected erythrocytes, to avoid human error. However, the main cause of error, that is due to a low parasite density, was not resolved by this approach.

In an attempt to enhance the detection of malaria parasites in blood films with a microscope, alternative methods have been introduced. Staining parasites with fluorescent dyes that have an affinity for the nucleic acid in their nucleus and illuminating with a proper light will make the nucleus strongly fluorescent, thus parasite presence (but not their species) can be detected using a fluorescence microscope[22,27]. However, such an instrument can be not easily available in many areas and an adeguate training is needed anyway. Other microscopy techniques used for malaria diagnosis have included cross-polarization microscopy and dark-field microscopy[28,31], that exploit imaging contrast enhancement due to hemozoin to improve diagnostic capability of blood smear observation. Indeed, since hemozoin crystals are optically birefringent (i.e. they cause a rotation of the plane of polarized light that pass through the crystals based on the anisotropies), it is much easier to observe them under polarized light microscopy as compared to traditional white light microscopy. However, implementation of this kind of microscopy lacks widespread adoption because of complexity and high-cost of the setup, which is usually bulky as well. Trying to overcome these limitations, Pirnstill et al. developed a cell-phone based transmission polarized light microscope system[31].

Rapid Diagnostic Tests (RDTs)

Rapid Diagnostic Test (RDTs) for malaria are fast (5–20 minutes), easy to perform and do not require electricity or specific laboratory equipment. They detect malaria antigen in a small amount of blood (usually 5–15 μl), exploiting immunochromatography[22,27]. Blood migrates along a test strip, impregnated with monoclonal antibodies directed against the target parasite antigen; when an antigen is captured by the corresponding antibody, a visible colored line is produced on the strip. Commercial tests are manufactured with different combinations of target antigens to suit the local malaria epidemiology. The most currently targeted are HRP-2, a *P. falciparum*-specific protein, and some enzymes related to the parasite, like pLDH and aldolase[22,27,32]. Some real RDTs and a sketch of the immunochromatography working principle are shown in Figure 1.4b.

Limits of detection of these tests rely on an amount of antigen equivalent to 200 parasites/μl of blood[4,28,32]. Most RDTs have achieved goods sensitivities (>95%) for *P. falciparum*, but not for other parasite species and not in low parasitemia. Additionally, several factors in the manufacturing process as well as environmental conditions may affect performance and sensitivity, e.g. manufacturers usually recommend 4°-30°C as the optimal temperature range, but in practice exposure to higher temperatures frequently occurs in tropical regions. Furthermore, RDTs are relatively expensive and prone to false-positive responses due to the persistence of malaria antigens in the blood for up to 2 weeks after the parasite has been cleared from the patient's circulation[4,28]. Thus, despite being really easy to use and fast, their use is limited, mainly due to their low sensitivity. Trying to improve it, in the past few years WHO has encouraged the development of new RDTs with more accurate detection capabilities[3].

Polymerase Chain Reaction (PCR)

PCR-based techniques, a relatively recent development in the molecular diagnosis of malaria, have proven to be among the most specific and sensitive diagnostic methods, particularly for malaria cases with low parasitemia or mixed infection. Indeed, the limit of detection is 1–5 parasites/μl of blood for all five human infecting *Plasmodium* species, the best sensitivity value currently achieved in malaria detection; also specificity (i.e. the ability to distinguish different species) is really high[4,22,27]. Polymerase chain reaction is a technique commonly used in molecular biology to amplify a single copy or a few copies of a segment of DNA, generating thousands to millions of copies of that particular sequence. A DNA polymerase (the origin of the

technique's name) and primers (short DNA fragments) containing sequences complementary to the target region enable selective and repeated amplification. As PCR progresses, the DNA generated is itself used as a template for replication, thus setting in motion a chain reaction. The basic operating principles of this technique are illustrated in Figure 1.4c. The most widely used target for malaria detection is the small subunit 18S ribosomal RNA gene (18S rDNA)[4].

Due to their relation with parasite DNA, PCR-based methods are particularly useful also for studies of mutations and parasite genes involved in drug resistance[27]. Although PCR appears to have overcome the two major problems of malaria diagnosis (i.e. sensitivity and specificity), its diffusion is limited by complex methodologies, high cost, and the need for specially trained technicians[4,22,27,33,34].

Many on-field tests[32,35–39] of these conventional techniques (microscopy, RDTs and PCR) in regions where malaria is endemic are reported and their results are in agreement with the previous analysis.

Magnetic techniques

A magnetic object inside a non uniform magnetic field experiences a force, as explained in detail in section 2.3. This property can be exploited to move magnetic particles suspended in a fluid, with a technique called high gradient magnetic separation (HGMS). This kind of magnetophoretic manipulation has been used for externally controlling matter inside microfluidic channels, through the use of an external permanent magnet that magnetizes a micrometric ferromagnetic component (e.g. nickel or permalloy wire) placed close or inside the channel, thus creating an intense magnetic field gradient[40]. There are different cases of application of this method for trapping or separation of superparamagnetic beads[41–44], cells labeled with magnetic tags[45,46] or blood cells[47–49]. For example, Han et al.[48,49] showed how to separate red blood cells (treated to become paramagnetic) from white blood cells (diamagnetic), using an external permanent magnet and a nickel wire.

Due to the magnetic properties of hemozoin crystals and infected red blood cells, a label-free magnetophoretic separation can be exploited also in malaria diagnosis[50]. Since detection is difficult mainly in low parasitemia cases, improvements can be achieved by separating[21,51] hemozoin and i-RBCs and concentrating[52–54] them in a small area, where they can be more easily examined under an optical microscope. Nam et al.[21] were able to separate late-stage i-RBCs (trophozoites and schizonts) with a recovery rate of approximately 98.3% and early-stage (ring-stage) i-RBCs, less para-

magnetic, with a recovery rate of 73%. They used a PDMS microfluidic channel integrated with a ferromagnetic wire fixed on a glass slide, as shown in Figure 1.4d. Even though the design by Nam et al. separates the parasites, it does not concentrate them on a slide for easier examination under the microscope, so further steps would be needed. As an alternative, Vyas et al.[53] used a microfluidic channel with multiple iron wires positioned on top of and underneath it, at a small angle with respect to its axis. The strong magnetic field gradient produced by the wires allows not only to separate i-RBCs, but also to concentrate them in a specific region, small enough to fit within the microscope field of view at magnifications typically required to identify malaria parasites. Simulations show that it is possible to separate and concentrate i-RBCs in less than 5 minutes, even in cases of very low parasitemia (1–10 parasites/μl of blood) using blood sample volumes around 3 μl. Magnetophoretic concentration is more efficient and less aggressive with respect to the conventional separation techniques, that typically expose RBCs to chemicals and osmotic stress. Also dielectrophoretic separation has been investigated as a possible solutions, but with poor results due to the slight difference in electrical properties of infected and not infected RBCs[4]. Despite the improvements provided by magnetic concentration, an optical microscope is still required to detect and count the parasites. In addition to the drawbacks related to microscopic detection previously examined, complexity and relatively high cost of microfluidic systems need to be considered.

Also some magneto-optic methods[20,55–57] for detecting malaria exploiting birefringence and anisotropy of hemozoin crystals have been developed, reaching in some cases rapidity and sensitivity levels comparable with the conventional techniques. However, experimental setup is usually really complex and expensive, since lasers and/or intense oscillating fields are required. Thus, an on-field application of these techniques does not seem feasible.

None of the currently used malaria detection method is optimal, many drawbacks are still present even in the *gold standard*. Exploiting magnetic properties of hemozoin and infected RBCs could lead to more effective diagnostic systems, possibly using a device able to reduce or eliminate the complexity related to microfluidics and visual counting through optical microscopy. Following this principle, a new device has been designed and partially implemented during this thesis work, as described in the next section.

1.2.2   The concept of Tid Mekii project

The idea of the Tid Mekii project is to develop a compact, low-cost and easy to use diagnostic system, which allows a pan-plasmodic and rapid detection, as sensitive and accurate as the *gold standard*. The device combines magnetic separation and electrical impedance detection. Indeed, thanks to their paramagnetic properties, infected RBCs and hemozoin crystals can be attracted using a magnetic field gradient and concentrated close to the surface of measurement electrodes; then, impedance variation caused by the particles can be detected. Following a lab-on-chip approach, all the diagnosis operations should be performed thanks to a disposable chip, composed by an array of micrometric nickel pillars with gold electrodes above. The blood drop that needs to be tested is placed on a glass substrate, which is then put in close contact to the chip surface, at a distance defined by an outer ring; this ring identifies also the blood volume where detection takes place. The chip is placed face-down, so that magnetic attraction towards the nickel pillars opposes the gravity. The required magnetic field gradient is provided macroscopically by a system of permanent magnets and microscopically by the nickel pillars, magnetized due to the external field. In the reversed configuration, i-RBCs and hemozoin crystals are attracted upwards towards the electrodes, while non-infected erythrocytes and the other blood cells (i.e. white blood cells and platelets) sediment towards the glass substrate, as shown in Figure 1.5. When the attracted particles reach the electrodes on the chip surface, they cause an electrical impedance variation, that can be detected through the electronic reading module (transimpedance amplifier and lock-in amplifier, see section 2.4), USB-connected to the chip.
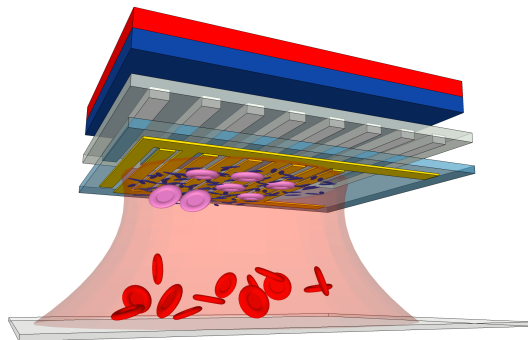
Figure 1.5: Scheme of the separation process: i-RBCs (pink) and hemozoin crystals (black) are attracted towards the chip, while non-infected RBCs (red) sediment.

This device can be used to identify the presence of both infected red blood cells, with hemozoin crystals inside, and free hemozoin crystals. Detecting i-RBCs allows a direct evaluation of the parasitemia (the number of infected erythrocytes) and can be performed also in the early phase of the disease, before the first asexual reproductive cycle is concluded and RBCs rupture, releasing hemozoin crystals. An earlier detection would be preferable but the attraction of infected RBCs is more challenging because they are less paramagnetic than isolated hemozoin crystals (see section 2.2.2), particularly in the first stages of the intra-erythrocytic development, when the fraction of hemoglobin already transformed in hemozoin is reduced. Moreover, people usually go to the hospital only after the first symptoms appeared, so when hemozoin crystals are already spread in the bloodstream. On the other hand, hemozoin crystals are present in a larger number (about 20 per i-RBC) and are more easily captured, but their reduced dimensions make the impedance detection harder. Therefore, the device should be properly designed to optimize both magnetic capture and impedance detection, achieving the best possible diagnosis conditions.

The aim of the project is to reach a sensitivity level up to 10 i-RBC/μl in the early stage of the disease and up to 5 pg/μl of hemozoin crystals after the rupture of the first RBCs' membrane, comparable with the one theoretically achieved with the *gold standard*. The analysis should also be fast (on the order of 10 minutes) and with a low cost, <1€ per disposable chip and around 100€ for the electronic reading module, exploiting a connection with an external laptop to visualize datas. Since the device is intended for an use in tropical areas with no skilled staff, it must be easy to use: almost everything should be automatic, the operator needs only to put the blood drop on the chip. The proposed design makes it possible to satisfy this requirement. Indeed, nor microfluidic channels (used in the majority of concentration methods) nor intense oscillating magnetic fields are required, and the electronic setup allows to reach high sensitivity with a relatively simple and low cost detection system. A patent has been recently deposited for the concept of the diagnostic device developed in the aforementioned Tid Mekii project[58].

1.3 Summary and outlook of the thesis

This thesis work is part of the Tid Mekii project, which aims at the development of an accurate, rapid, easy to use and low-cost detection system for malaria *Plasmodium*, as described in the previous section. The experimental activity has been performed in *PoliFab* laboratory under the supervision of

Prof. Riccardo Bertacco, head of the *Nanomagnetism* group of the Department of Physics. The detection platform has been developed in collaboration with the I^3N group of Politecnico di Milano, leaded by Prof. Marco Sampietro, that designed, fabricated and characterized the electrical part of the device. The bovine blood samples used in the experiments were provided and treated by μBS Lab of Politecnico di Milano, leaded by Prof. Gianfranco B. Fiore.

Despite the complexity of the presented work, involving different areas of knowledge and competences, during this thesis the feasibility of the TID MEKII concept has been demonstrated. In particular, after an initial design and optimization phase carried out with simulations performed in *COMSOL Multiphysics*[59], the device fabrication process was developed. Moreover, magnetic and electrical properties of hemozoin crystals were characterized. Finally, preliminary magnetic capture experiments on hemozoin crystals and red blood cells have been carried out. These experiments confirm the possibility to efficiently capture and concentrate targeted particles, i.e. both i-RBCs and hemozoin, on top of nickel concentrators. At the same time, the capability to detect the desired concentration of i-RBCs and hemozoin by electrical impedance measurements has been demonstrated in the framework of another thesis work, by the group of Prof. Marco Sampietro. These results constitute the basis for the next step: the design and realization of the first chips, integrating both concentrators and electrodes, for the validation of the TID MEKII concept with bovine blood models of infected human blood.

Here an overview of the chapters is presented:

- **Chapter 1: Introduction.** This chapter illustrates the main aspects of malaria, focusing also on diagnostic methods currently used, and a summary of this thesis work.

- **Chapter 2: Theory.** The theoretical aspects needed to understand the working principle of micromagnetic devices are presented, together with a description of the forces acting on a particle in a fluid and the basic principles of an impedance measurement, to allow a better comprehension of the diagnosis mechanism.

- **Chapter 3: Feasibility study and simulations.** The main phases of the feasibility study carried out to properly design the complete device are presented, with a main focus on the numerical simulations related to magnetic capture.

- **Chapter 4: Experimental methods.** This chapter shows the experimental techniques used in this work: microfabrication methods, mag-

netic and electrical characterization techniques, experimental setup used for capture experiments and, finally, the protocol to treat bovine red blood cells to produce an animal model of human blood infected by *Plasmodium*.

- **Chapter 5: Experimental results.** In this chapter the main experimental results are presented. First, a magnetic and electrical characterization of synthetic hemozoin crystals, to determine the real properties to be used for the design of the diagnostic chips, is presented. Then, the optimization of the fabrication process for the chip realization is reported. Subsequently, magnetic capture experiments performed with these devices and different kinds of particles, including magnetic beads, bovine models of i-RBsC and hemozoin crystals, are described. Finally, for the sake of completeness, the main results of impedance measurements are shown.

- **Chapter 6: Conclusions and Perspectives.** This section summarizes the main results of this thesis and outlines the future perspectives of the TID MEKII project.

Chapter 2

Theory

This chapter presents the theoretical background needed to understand the working principles of the detection device developed in this thesis work. In the first part, the behavior of (ferro)magnetic materials with dimensions in the micrometric range is illustrated. Then, the physical behavior of magnetic particles is considered, followed by a description of the forces acting on them when they are in a fluid. Finally, basic concepts of an impedance measurement are introduced for a better comprehension of the device detection mechanism.

2.1 Micromagnetics

The behavior of a magnetic object is described through the relation between the magnetization vector $\mathbf{M(r)}$ and the magnetic field $\mathbf{H}$, i.e. $\mathbf{M(H)}$. Many physical processes contribute to determine the magnetic configuration of a certain (ferro)magnetic body, so a precise evaluation of this expression is not simple. In a thermodynamic approach, the equilibrium configuration of $\mathbf{M(r)}$ arises from the minimization of the free energy functional, in which four energetic terms need in general to be considered: exchange interaction, magnetostatic energy, magnetic anisotropy and Zeeman energy. The main complication of this kind of approach is related to the dependence of each contribution (in particular anisotropy and exchange) on the materials atomic structure. Therefore, the energy minimization should be carried out in an infinite dimensional space, taking into account the spatial coordinates of each atom.

Micromagnetics is a theory developed to overcome this difficulty. It relies on the idea that a magnetic material can be divided into small volume elements ΔV, where the magnetization is considered uniform[60]. These vol-

ume elements must be small compared to the typical length over which the magnetization varies significantly (the so called *exchange length*, see section 2.1.1) and at the same time large enough to contain a sufficient number of atoms to be able to apply statistics and thermodynamics rules. Then, the free energy is expressed according to the continuum approximation, i.e. considering $\mathbf{M(r)}$ a smoothly varying function. In addition, the relaxation time for reaching thermal equilibrium in each volume element is assumed to be sensibly shorter than the relaxation time for the entire system. The physical mechanisms involved in the magnetization process of a magnetic object and the resulting expressions for each energetic term involved in the free energy functional are described in the following sections.

2.1.1   Exchange energy

Exchange interaction is a quantum mechanic effect related to the interaction between magnetic spins, which promotes parallel (in ferromagnetic materials) or anti-parallel (in antiferromagnets) orientations of spins along interatomic distances. It is usually expressed through the Heisenberg Hamiltonian:

$$\hat{H}_{exchange} = -\sum_{i,j=1}^{N} J_{ij}\mathbf{S}_i \cdot \mathbf{S}_j \tag{2.1}$$

where $\mathbf{S}_i$ is the spin angular momentum operator of the ion located at the i-th site of a lattice and J_{ij} measures the strength of the exchange coupling between the moments i and j. Since this interaction is short-range and decreases rapidly with increasing distance between atoms, the sum can be calculated taking into account only the interactions between the nearest neighbors. Replacing the quantum operators with classical vectors and considering a small angle between neighboring spins, the exchange energy expression can be written as:

$$E_{exchange} = \int_V \frac{A}{2}\left[(\nabla m_x)^2 + (\nabla m_y)^2 + (\nabla m_z)^2\right]dV \tag{2.2}$$

where m is defined as the ratio between M and the saturation magnetization M_S and A (measured in J/m) is the *exchange stiffness* constant, which indicates the strength of the exchange interaction. Considering a cubic lattice A is defined as:

$$A = \frac{2JS^2c}{a} \tag{2.3}$$

where a is the distance between nearest neighbors and c is a parameter depending on the atomic structure of the material.

The exchange stiffness A is related to a fundamental length scale in micromagnetics called *exchange length*; it is defined as the shortest length scale over which the magnetization rotates, considering only exchange and magnetostatic energy, and can be expressed as follows:

$$l_{ex} = \sqrt{\frac{A}{\mu_0 M_s^2}} \tag{2.4}$$

2.1.2 Magnetostatic energy

Magnetostatic energy represents the dipolar energy stored in a given configuration $\mathbf{M(r)}$ of a macroscopic material. It depends on the magnetostatic interaction between local magnetic moments, so it is essentially the dipole-dipole interaction energy of the system. Compared to exchange, it is a long range contribution. Considering a magnetic body in a certain region of space, the magnetostatic energy can be expressed as:

$$E_{magstat} = -\frac{1}{2}\mu_0 \int_V \mathbf{M} \cdot \mathbf{H}_d \, dV \tag{2.5}$$

where the integration is performed over the entire magnetic material. $\mathbf{H}_d$ is the so called *demagnetizing field*, i.e. the field produced by the magnetic body due to its magnetization. For a magnetic material with a second order surface, it can be written as:

$$\mathbf{H}_d = -N\mathbf{M} \tag{2.6}$$

where N is the demagnetizing tensor, strongly affected by the shape of the material, and $\mathbf{M}$ the magnetization of the object. The magnetostatic energy is at the origin of the shape anisotropy. For a peculiar shape of the body, analytically expressed by N, the magnetostatic energy is minimized when the magnetization tends to stay parallel to the direction of elongation of the body. Thus, in a thin film $\mathbf{M}$ tends to lie in the plane, while in a stripe it tends to align with the major axis.

2.1.3 Magnetic anisotropy energy

Magnetic properties are direction-dependent for many magnetic materials. A relevant cause of the so called *magnetic anisotropy* is the magnetocrystalline anisotropy, that arises as a consequence of the coupling between spin

and orbital motion of electrons in the crystal lattice. Indeed, this produces stable directions of spontaneous magnetization, or easy axis, along which the magnetization preferably aligns. When $\mathbf{M}$ is not aligned along one of these directions, an energy cost is present, that represents the work required to align the magnetization along a direction different from the easy axis.

If we consider a uniform magnetization $\mathbf{M} = M_s\mathbf{m}$ within each volume ΔV, the energy density $e_{AN}(\mathbf{m})$ can be represented as a surface in space, where $e_{AN}(\mathbf{m})$ is the distance from the origin of the point of the surface lying along the direction of $\mathbf{m}$. In this representation, the direction of the easy axis can be found considering the minima in the energy surface. For uniaxial anisotropy, the anisotropy energy density can be written as a series of trigonometric functions:

$$e_{AN} = K_0 + K_1 sin^2\theta + K_2 sin^4\theta + \dots \tag{2.7}$$

where θ is the angle between the anisotropy axis and $\mathbf{M}$. K_0, K_1, K_2 are called *anisotropy constants* and are measured in $J \cdot m^{-3}$. Usually the series is truncated at $sin^2\theta$ term. When $K_1 > 0$ easy axis anisotropy occurs (i.e. magnetization lies along a preferred axis), whereas for $K_1 < 0$ easy plane anisotropy is present (i.e. magnetization has a preferred plane). The anisotropy field, a relevant quantity that expresses the strength of the magnetic anisotropy, is the field required to saturate the magnetization along the hard-axis. It is defined as:

$$H_{AN} = \frac{2K_1}{\mu_0 M_S} \tag{2.8}$$

2.1.4   Zeeman energy

Zeeman energy term describes the interaction of magnetic moments with an external magnetic field $\mathbf{H}_a$ applied to the system. In this situation magnetic moments try to reduce their energy by aligning parallel to the external field. This energy term is expressed as:

$$E_{Zeeman} = -\mu_0 \int_V \mathbf{M} \cdot \mathbf{H}_a \, dV \tag{2.9}$$

2.1.5   Final magnetic configuration

Adding up the energy contributions due to exchange interaction, demagnetization, magnetic anisotropy and external field, the total free energy of a magnetic system can be written as[60]:

$$E_{TOT} = \int_V \left\{ \frac{A}{2} \left[(\nabla m_x)^2 + (\nabla m_y)^2 + (\nabla m_z)^2 \right] \right.$$
$$\left. + e_{AN} - \frac{1}{2} \mu_0 \, \mathbf{M} \cdot \mathbf{H}_d - \mu_0 \, \mathbf{M} \cdot \mathbf{H}_a \right\} dV \tag{2.10}$$

where $m = M/M_s$, $\mathbf{H}_d$ and $\mathbf{H}_a$ are respectively the demagnetizing field and the external magnetic field.

The local minima of this expression correspond to the equilibrium configuration of a certain magnetic object, i.e. the metastable states for $\mathbf{M}$. The solution may not be straightforward because the terms that contribute to the total energy of the system can compete towards different minima configurations. Exchange coupling promotes magnetization states where $\mathbf{M}$ is aligned within the entire volume; magnetocrystalline anisotropy instead favors the alignment of $\mathbf{M}$ along easy axis or easy planes within the magnetic object; magnetostatic energy promotes micromagnetic configurations in which $\mathbf{M}$ follows close paths within the magnetic body in order to reduce the stray field outside; Zeeman energy favors the alignment of $\mathbf{M}$ along the external field. Thus, according to the relative weight of the contributions, different configurations can arise, i.e. different magnetic domains (portions of the body with uniform magnetization) can be formed. Indeed, domain formation decreases magnetostatic energy, but it has also a cost related to exchange and magnetic anisotropy energy. In 1935 Landau and Lifschitz showed theoretically that the existence of magnetic domains is a consequence of E_{TOT} functional minimization[61].

2.2 Magnetic particles

A relevant magnetic property of a material is its volume magnetic susceptibility χ, which describes the material's response to an applied magnetic field $\mathbf{H}$, i.e. its magnetization, with the relation $\mathbf{M}=\chi\mathbf{H}$. In presence of a magnetic material the total flux density $\mathbf{B}$ results to be:

$$\mathbf{B} = \mu_0(\mathbf{H} + \mathbf{M}) = \mu_0(1 + \chi)\mathbf{H} = \mu_0\mu_r\mathbf{H} \tag{2.11}$$

where $\mu_0 = 4\pi \cdot 10^{-7}$ Tm/A is the permeability constant in vacuum and $\mu_r = 1 + \chi$ the relative permeability of the object.

Depending on the interaction of the material with an external magnetic field, different magnetic behaviors can be identified. Diamagnetic materials have a negative χ (i.e. $\mu_r{<}1$) and are repelled by external magnetic fields.

Conversely, paramagnetic materials have a slightly positive χ (i.e. μ_r>1) and are weakly attracted by the external fields. In the low field limit the magnetic susceptibility does not depend on the applied field, but then with increasing applied field the magnetization departs from linearity and it becomes a Langevin function of the applied field, reaching saturation at high fields[62]. Both diamagnetic and paramagnetic materials do not possess a permanent magnetization in the absence of an externally applied magnetic field. Ferromagnetic materials have positive χ with a much higher value (i.e. μ_r >>1) but the susceptibility is not a single value function of **H**, due to the phenomenon of hysteresis, leading to permanent magnetization even without an external magnetic field. Moreover, reducing the dimensions of a ferromagnetic body below a certain size, as in the case of nanoparticles, a different magnetic effect called *superparamagnetism* can arise.

2.2.1 Superparamagnetic beads

A superparamagnetic particle behaves as a macrospin (where spins are aligned by exchange interaction) with total magnetic moment fluctuating over time, such that the net average magnetic moment is zero for long enough observation windows. In a small magnetic particle of volume V with a uniaxial anisotropy (anisotropy constant K_1), thermal fluctuations can cause a continuos magnetization reversal between two different magnetization states, i.e. parallel or antiparallel to the easy-axis. This occurs if the thermal energy k_BT, where k_B is the Boltzmann constant, is larger than the activation energy K_1V for flipping the magnetization from parallel to antiparallel. The average time between two thermally activated transitions τ is:

$$\tau = \tau_0 \, exp\left(\frac{K_1V}{k_BT}\right) \tag{2.12}$$

where τ_0 ranges between $\approx 10^{-9}$ s and $\approx 10^{-11}$ s for single particles, and T is the absolute temperature. Thus, the energy barrier (K_1V) decreases with the particle size and, conversely, an enhancement of the flipping rate occurs. Superparamagnetism is a size-effect depending either on the observation time t and on the temperature T. Indeed, magnetic particles are blocked, i.e. display a ferromagnetic behavior, for an observation time much smaller than τ, which corresponds to a temperature below the blocking temperature T_B, defined as the temperature at which τ is equal to t. Then, above T_B, the particles are in a superparamagnetic state until the Curie temperature T_C is reached, when their behavior becomes paramagnetic. In the superparamagnetic state, in absence of external magnetic field, the resulting fluctuations in

the direction of the magnetization cause the total magnetic moment average to zero, which means that superparamagnetic particles have no remanent magnetization. Conversely, when inserted in a field, the total magnetic moment of the particle will tend to align to the field lines.

The susceptibility of superparamagnetic particles is much higher than that of a paramagnet because it is related to the magnetic moment of all the ferromagnetic atoms aligned due to exchange interaction, while in paramagnets only the magnetic moment of a single ion is involved. The high susceptibility value, together with a negligible hysteresis and no remanence, make these particles suitable for several biological applications where formation of clusters should be avoided and a prompt reaction to an applied field is required. Indeed, they can be isolated from a solution using a magnetic field gradient and re-suspended again when the field is removed.

A magnetic nanoparticle is usually composed by a superparamagnetic core surrounded by a non-magnetic coating, required to allow functionalizations with biomolecules of interest. Magnetic cores made of Iron oxides such as maghemite (Fe_2O_3) or magnetite (Fe_3O_4) are widely used for biological experiments, due to their reduced toxicity[63]. Typically, these particles have a size that ranges between 5 and 50 nm in diameter. However, with such dimensions the magnetic moments are relatively small, making the application of relevant forces extremely challenging. Additionally, manipulating single superparamagnetic nanoparticles is complex due to thermal agitation related to Brownian motion (see section 2.3). To preserve superparamagnetic properties, achieving at the same time a larger magnetic moment and volume, bigger magnetic beads (0.1 to 5 μm in diameter) are used. They are fabricated embedding several superparamagnetic cores in a polymer matrix, that acts as a non-magnetic shell.

In this thesis work, *nanomag-CLD-redF* (Micromod-Germany) superparamagnetic beads with a polymeric matrix of dextran were used. They have a 300 nm diameter and are functionalized with $COOH^-$ and a fluorescent marker in the far-red (excitation: 552 nm, emission: 580 nm). According to the data available for other superparamagnetic particles with similar dimension and composition, a susceptibility in the order of 1 has been considered, although a specific data for the particles we used is not available.

2.2.2 Hemozoin crystals and red blood cells

The unpaired electrons (five per heme group) of the partially occupied iron $3d$ orbitals are responsible for hemozoin paramagnetism[6,16,18–20]. Despite hemozoin magnetic behavior has been investigated, not many susceptibility

measures are available in literature. This is one of the reasons why we performed an independent characterization of synthetic crystals, as described in section 5.1.1. The value of hemozoin volume magnetic susceptibility χ calculated by Coronado et al. [6], starting from experimental results acquired by Hackett et al. [16], is $\chi=320\cdot10^{-6}$. Recently, Inyushin et al. [64] suggested that hemozoin is superparamagnetic instead, with a much higher calculated susceptibility value, i.e. $\chi=3845$. However, as discussed in section 5.1.1, our independent measurements on synthetic crystals produced by the same company do not confirm the superparamagnetic behavior reported by Inyushin and coworkers. The susceptibility turns out to be very similar to that reported by Coronado et al., with strong implications on the design of the diagnostic test.

The magnetic susceptibility of red blood cells depends on the oxidation state of the hemoglobin molecules inside them[17,65]. Oxygenated erythrocytes (i.e. in a normal state) exhibit a weak diamagnetic behavior, as their net magnetic susceptibility relative to plasma is $\Delta\chi_{ox-RBC}$=-0.18$\cdot10^{-6}$ [65–68], where plasma susceptibility is χ_P=-7.7$\cdot10^{-6}$ [48,49]. Thus, when inserted in a magnetic field, they experience a repulsive force form the magnet producing the field. Conversely, due to the presence of hemozoin crystals inside them, infected RBCs have a paramagnetic behavior, with a positive $\Delta\chi$ that increases during the evolution of the disease[9,68], as more hemoglobin is converted to hemozoin (up to a maximum of 80% [9]). Indeed, the value of the net magnetic susceptibility relative to plasma $\Delta\chi_{i-RBC}$ is 0.82$\cdot10^{-6}$ in the *ring*-stage[4,9,68], 0.91$\cdot10^{-6}$ in the *trophozoite* one[4,9,68] and 1.80$\cdot10^{-6}$ in the *schizont* phase[4,9,16,64,66–68]. Thus, i-RBCs are always attracted by magnetic fields due to their paramagnetic properties, but with a different intensity according to the infection phase.

Furthermore, hemozoin heme electron configuration with five unpaired electrons (S=5/2) corresponds to *ferri-heme*, which is a part of methemoglobin (metHb), i.e. the oxidized form of hemoglobin. Paramagnetic properties of this molecule are known since 1936[17,66,69] and more recently Moore et al. [9,67] proved that cells containing sufficient metHb concentrations or mature parasites have a similar behavior when inserted in a region with a magnetic field, i.e. they migrate in the direction of increasing field strength. Upon exposure of RBCs to particular oxidizing drugs, hemoglobin is oxidized into metHb[21,70,71], as discussed in section 4.4. Note that the net magnetic susceptibility relative to plasma of RBCs where all the hemoglobin has been transformed in metHb is $\Delta\chi_{metHb-RBC}$=3.9$\cdot10^{-6}$ [21,67], more than twice the tabulated value for i-RBCs, but this value can be reduced if the treatment is not 100% effective.

Particle	$\Delta\chi$ ($\cdot 10^{-6}$)
Hemozoin crystals	320
ox-RBCs	-0.18
Early ring i-RBCs	0.82
Late trophozoite i-RBCs	0.91
Schizont i-RBCs	1.80
metHb-RBCs	3.90

Table 2.1: Magnetic susceptibilities relative to water of hemozoin crystals[6] and RBCs[4,9,16,21,64–68].

The net susceptibility values of hemozoin crystals and RBCs (oxygenated, treated and infected) are summarized in Table 2.1. Magnetic and electrical properties of synthetic hemozoin crystals (InvivoGen-USA) were characterized, as discussed in section 5.1 and section 5.4. Moreover, the same crystals and bovine RBCs treated to obtain metHb, according to the protocol presented in section 4.4, were used in magnetic capture experiments described in section 5.3.

2.3   Forces on a magnetic particle in a fluid

According to the concept of the proposed diagnostic test for malaria, magnetic particles are subjected to a gravitational force (partially opposed by buoyancy force) a magnetic force and a fluid drag force.

The net contribution due to gravity and buoyancy force is:

$$\mathbf{F}_{G-B} = V_p \left(\rho_p - \rho_{fluid}\right) \mathbf{g} \tag{2.13}$$

where $V_p = \frac{4}{3}\pi R_p{}^3$ is the volume of the particle (modeled as a sphere of radius R_p), ρ_p is the particle mass density, ρ_{fluid} is the mass density of the surrounding fluid, and $\mathbf{g}$ is the gravity acceleration.

As discussed in section 2.2, a paramagnetic particle in a spatially varying magnetic field will be attracted towards the region of larger field, while a diamagnetic one will be repelled. With the approximation that the length scale over which the magnetic field changes is larger than the particle diameter and assuming a linear susceptibility of the particle material, the magnetic force can be written as:

$$\mathbf{F}_M = \frac{\mu_0}{2} V_p \, \Delta\chi_p \, \nabla H^2(\mathbf{x}_c) \tag{2.14}$$

where μ_0 is the vacuum permeability constant, V_p is the particle volume, $\Delta\chi_p=\chi_p-\chi_{fluid}$ is the net magnetic susceptibility of the particle with respect to the fluid and $H(\mathbf{x}_c)$ is the field that would be present if the magnetic particle was not there, evaluated in the position of the particle center $\mathbf{x}_c$.

Considering small Reynolds numbers ($Re << 1000$) and assuming that the fluids are incompressible, the drag force acting on a spherical particle of radius R_p, moving at a speed $\mathbf{v}$ in a fluid flowing with a certain velocity $\mathbf{u}$, can be expressed as:

$$\mathbf{F}_D = 6\pi\,\eta_{fluid}\,R_p\,(\mathbf{u}-\mathbf{v}) = b\,(\mathbf{u}-\mathbf{v}) \tag{2.15}$$

where η_{fluid} is the fluid viscosity and b is a drag coefficient, which highlights the linear dependence between the velocity of the body and the drag force. The system used in this project does not involve fluids in motion, thus $\mathbf{u}=0$ and the drag contribution can be expressed just as $\mathbf{F}_D$=-b $\mathbf{v}$.

In the designed detection system a reversed configuration is considered, i.e. magnetic particles are attracted upwards towards the nickel pillars. Therefore, the magnetic force has to overcome the sedimentation (i.e. the net contribution of gravity and buoyancy force) and the drag force. Conversely, in magnetic capture experiments described in section 5.3 a direct configuration is used. Since magnetic particles are attracted downwards towards the nickel pillars, magnetic force is directed as the sedimentation. Simplified schemes of the forces acting on a magnetic particle in both configurations are shown in Figure 2.1. The analysis will be performed only in the reversed configuration; analogous calculations for the direct case are straightforward.
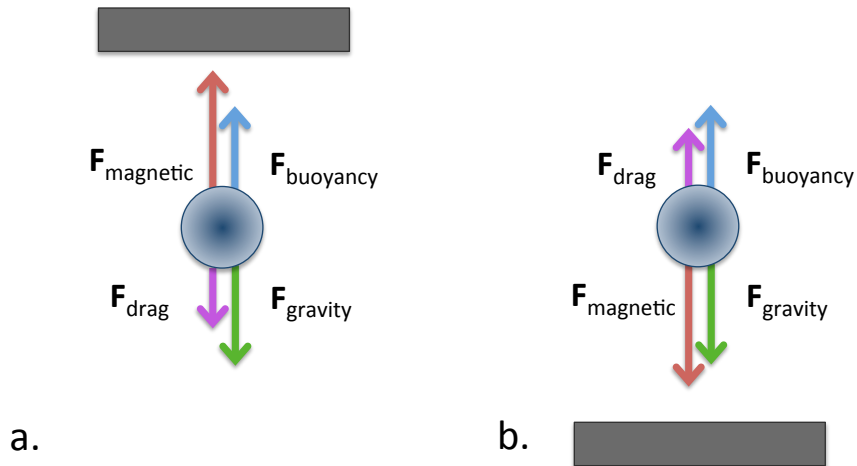
Figure 2.1: Force diagrams for reversed (**a.**) and direct (**b.**) configurations. The grey boxes represent the chip.

Considering all contributions, it is possible to write the resulting motion equation using Newton's second law:

$$\frac{\mu_0}{2} V_p \, \Delta\chi_p \, \nabla H^2(\mathbf{x}_c) - V_p \, (\rho_p - \rho_{fluid}) \, \mathbf{g} - b \, \mathbf{v} = \rho_p \, V_p \, \frac{d\mathbf{v}}{dt} \qquad (2.16)$$

This is the equation of an accelerated motion inside a viscous medium $(\dot{\mathbf{v}} + \frac{1}{\tau}\mathbf{v} = \mathbf{a})$, with $\tau = \rho_p V_p / b$ and $\mathbf{a} = (\mathbf{F}_M - \mathbf{F}_{G-B})/\rho_p V_p$. Considering the properties of hemozoin crystals, red blood cells and blood (see section 3.2.5), the time required to reach a steady-state situation is really small ($\tau < 1\mu$s). Therefore, for uniform values of the magnetic force, i.e. for ∇H^2 slowly varying in the region of motion, it can be assumed as a good approximation that the magnetic particles (i.e. hemozoin crystals and i-RBCs) move with their constant steady-state velocity $\bar{\mathbf{v}}$. Thus, the right-hand side of the equation becomes zero and the velocity of a magnetic particle can be expressed as:

$$\bar{\mathbf{v}} = \frac{\mathbf{F}_M - \mathbf{F}_{G-B}}{b} = \frac{\frac{\mu_0}{2} V_p \Delta\chi_p \nabla H^2(\mathbf{x}_c) - V_p(\rho_p - \rho_{fluid})\mathbf{g}}{6\pi\eta_{fluid}R_p} =$$
$$= \frac{2}{9} \frac{R_p{}^2}{\eta_{fluid}} \left[\frac{\mu_0}{2} \Delta\chi_p \nabla H^2(\mathbf{x}_c) - (\rho_p - \rho_{fluid})\mathbf{g} \right] \qquad (2.17)$$

Thus, in order to make magnetic particles move towards the chip in the reversed configuration, i.e. to have a positive $\bar{\mathbf{v}}$, the following condition on $\nabla H^2(\mathbf{x}_c)$ needs to be fulfilled:

$$\nabla H^2(\mathbf{x}_c) > \frac{2\,(\rho_p - \rho_{fluid})\,\mathbf{g}}{\mu_0\,\Delta\chi_p} \qquad (2.18)$$

Furthermore, particles in a fluid experience diffusion arising from the random collisions with fluid molecules; the resulting random motion is called *Brownian motion*. The diffusion coefficient D of a particle can be expressed by the Stokes-Einstein relation[72]:

$$D = \frac{k_B T}{b} \qquad (2.19)$$

where k_B is the Boltzmann constant, T is the absolute temperature and b is the drag coefficient. The average distance travelled by a particle in a time t due to diffusion, called diffusion length l_{diff}, is:

$$l_{diff} = \sqrt{Dt} \qquad (2.20)$$

The value of the diffusion length indicates how significantly Brownian motion affects the particle position, in absence of external forces. Due to the inverse dependance on R_p and η_{fluid}, this contribution increases for smaller particles and less viscous fluids. For example, the diffusion length in water after 1 s is $\sim$1.2 μm for 300 nm beads, $\sim$1.1 μm for hemozoin crystals (considering an average dimension of 350 nm) and $\sim$300 nm for red blood cells (average radius 2.78 μm); the corresponding values in a more viscous fluid like blood are almost halved. Therefore, the effect of Brownian motion is more relevant for hemozoin crystals and magnetic beads than for erythrocytes. For this reason it has been included in the initial physical model used to describe particle motion in the feasibility study, especially for hemozoin crystals. However, numerical simulations show that in our configuration the final result is not strongly affected by this contribution.

2.4   Principles of impedance detection
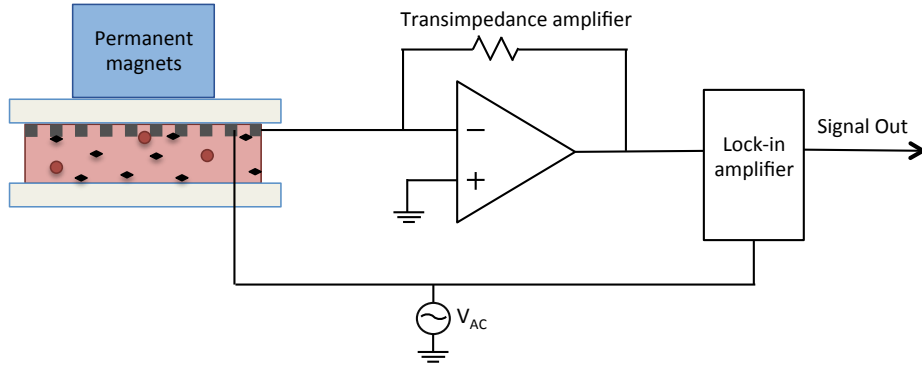
Figure 2.2: Scheme of the main elements of the electrical circuit used to measure impedance variation, connected with the detection device.

Electrical impedance spectroscopy (EIS) involves the electrical excitation of a device with a subsequent measure of its response, in order to determine its impedance, according to generalized Ohm's first law[73,74]. Impedance detection has been exploited in systems where the element under test was trapped or moving in microfluidic channels; the possibility to use it directly on blood samples has been also reported[75,76]. This label-free, real-time and non-invasive approach has been considered in TID MEKII project for quantifying the concentration of malaria infection markers, i.e. hemozoin crystals and infected red blood cells. High sensitivity and effectiveness have been demonstrated by using interdigitated electrodes to measure the amount
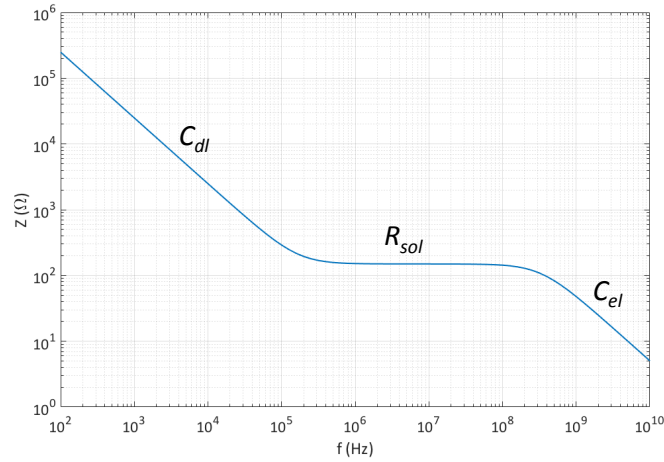
Figure 2.3: Frequency spectrum of the electrodes. Data are obtained with electrical simulations in *COMSOL Multiphysics*.

of particles deposited on top of them. In order to characterize the electrodes, an electronic system like the one depicted in Figure 2.2 has been used. A sinusoidal voltage modulated at 2 MHz was provided with a lock-in amplifier (HF2LI, Zurich Instruments) and the current flowing through the electrodes was converted into a voltage with a transimpedance amplifier (HF2TA, Zurich Instruments). The resulting signal was then demodulated by the lock-in amplifier.

The impedance spectrum of the electrodes, represented in Figure 2.3, is characterized by two capacitive regions, at low and high frequencies, and a resistive plateau. The double layer capacitance C_{dl}, the most dominant contribution at low frequencies, in related to the accumulation of two layers of charged particles with opposing polarity at the interface between a conductive electrode and an adjacent liquid electrolyte, when a voltage is applied. The two layers of charged particles are separated by a single layer of solvent molecules, that adheres to the surface of the electrode and acts like a dielectric in a conventional capacitor. Conversely, at high frequencies, impedance is mainly related to the capacitance of the electrodes C_{el}. Between these two regions, a resistive plateau with an impedance corresponding to the resistance of the electrodes due to the presence of the solution (R_{sol}) is present. The value of R_{sol} is related to the shape and size of the electrodes, as well as, of course, the conductivity (σ_{sol}) of the solution on top of them. For example, considering N interdigitated electrodes with length L, width W and spacing S, an approximated form of R_{sol}[73] can be obtained as:

$$R_{sol} \approx \frac{2}{\sigma_{sol} \cdot (N-1) \cdot L} \sqrt[3]{\frac{S}{N}} \tag{2.21}$$

This relation holds for $0.1 < S/W < 10$ (i.e. in most of the currently employed geometries) and was validated with electrical simulations performed in *COMSOL Multiphysics*. The simulated values are very close to those obtained with Eq. (2.21) for a sufficiently high number of electrodes, i.e. $N > 6$. In a first phase of the project interdigitated electrodes were considered, but then a different geometry was designed to optimize the detection, considering the actual shape of the region of the nickel concentrators where particles are captured. Since for this new configuration of the electrodes, described in section 5.4, there is no analytical expression for R_{sol}, the value was calculated with numerical simulations, using a model previously validated with interdigitated electrodes.

For the quantitative estimate of the number of malaria biomarkers on top of the electrodes, the relevant quantity to measure is not the absolute impedance value but its variation due to the presence of magnetically captured particles (i.e. hemozoin crystals and i-RBCs) close to the electrodes. The associated double layer capacitance variation is small and not easily controllable, while measuring changes in the electrodes capacitance requires very high frequencies ($\sim$ GHz), thus a much more complex and expensive electrical setup. Therefore, detection should focus on the variation of the resistance of the electrodes R_{sol} due to the captured particles, which can be measured exciting the system with a voltage at a frequency corresponding to the resistive plateau (i.e. around MHz). Moreover, the percentage variation $\Delta R/R_0$ should be considered instead of the absolute difference because the noise and the minimum detectable variation depend on the value of the resistance. An expression for the percentage variation can be obtained starting from the Maxwell's mixture equation[77–79]:

$$\sigma_{mix} = \sigma_m \left(1 + 3 \frac{V_p}{V_{el}} \frac{\sigma_p - \sigma_m}{\sigma_p + 2\sigma_M} \right) \tag{2.22}$$

where σ_{mix} is the total mixture conductivity, σ_m is conductivity of the medium, σ_p is the conductivity of the particle, V_p is the particle volume and V_{el} is the sensitive volume of the electrodes. This expression is valid for $V_p \ll V_{el}$. If $\sigma_p \to 0$, i.e. if the analyzed particles are insulating, Eq. (2.22) becomes:

$$\sigma_{mix} \approx \sigma_m \left(1 - \frac{3}{2}\Phi \right) \tag{2.23}$$

where $\Phi = V_p/V_{el}$ is the volumetric fraction. While the deeply studied RBCs have an insulating behavior, no data are available for hemozoin crystals. However, measurements performed in DC with a Current Sensing AFM (see section 5.1.2) and at 2 MHz with the aforementioned electrical setup, described in section 5.4, suggest that also these particles are insulating in low frequency regime and more insulating than PBS (Phosphate Buffer Saline) in high frequency regime, so it is possible to use the simplified version of the formula, as a first approximation. Moreover, considering a small volumetric fraction, it is possible to rewrite Eq. (2.23) in terms of resistivity as:

$$\rho_{mix} \approx \rho_m \left(1 + \frac{3}{2}\Phi\right) \tag{2.24}$$

Since ρ_{mix} and ρ_m are related to R_{mix} and R_0 (i.e. the resistance of the whole mixture and the initial resistance without particles) through the same proportionality constant, resistance percentage variation can be expressed as:

$$\frac{\Delta R}{R_0} = \frac{R_{mix} - R_0}{R_0} = \frac{3}{2}\Phi = \frac{3}{2}\frac{N_p V_{sp}}{V_{el}} \tag{2.25}$$

where N_p is the number of particles and V_{sp} is the volume of a single particle.

The variation of the resistance due to the presence of the particles in the designed detection system is low, as discussed in section 3.1, thus discerning the actual signal from noise and external disturbs is extremely problematic and demanding, mainly due to the medium fluctuations, such as temperature variation and medium evaporation (leading to an increase of ions concentration). However, since these fluctuations are approximately regular across a single droplet, they can be removed performing a differential measurement: the signal from reference electrodes can be subtracted from the one coming from actual measurement electrodes, thus eliminating the common contributions. To these purpose, half of the chip area is occupied by measurement electrodes, upon which particles should be concentrated due to the nickel microstructures fabricated underneath, while the other half is reserved to reference electrodes, where ideally no particle should be present due to the absence of nickel concentrators.

Chapter 3

Feasibility study and simulations

Malaria diagnostic chip conceived in the TID MEKII project is based on two physical phenomena, magnetic capture of malaria biomarkers (i.e. hemozoin crystals and infected RBCs) and quantification of their concentration through an impedance variation detection. In this chapter the main phases of the feasibility study carried out to properly design the complete device are presented. First, an estimate of the constrains related to the limit of detection of micrometric electrodes is illustrated. Then, the parameters and the main results of numerical simulations performed to design the magnetic attraction system are described. Finally, the integration of both contributions is considered.

3.1 Electrical detection limit

The impedance variation exploited for quantifying the concentration of hemozoin crystals and i-RBCs is proportional to their volumetric fraction, as discussed in section 2.4. The minimum possible in-liquid $\Delta R/R_0$ measurable with usual electronic systems is around 0.1%. This estimate has been obtained for electrodes with $R_{sol} \approx 100\Omega$, a modulation frequency around 2 MHz, a 0.5 Hz bandwidth for the low pass filter within the lock-in amplifier and an amplification of the transimpedance amplifier around 100. Thus, considering also that the limit of detection (LOD) the TID MEKII project aims to achieve is $\sim$10 i-RBC/μl, the maximum portion of the chip area that can be occupied by the sensitive surface of active electrodes can be estimated.

The order of magnitude of the chip area is 1 cm^2 and with a 500 μm-thick droplet the total analyzed blood volume is 50 μl. However, only half

of it (i.e. 25 μl) will be on the actual measurement electrodes because the remaining part of the chip surface is occupied by reference electrodes, as discussed in section 2.4. Thus, in the conditions of the limit of detection, the number of infected erythrocytes N_{i-RBC} to detect is 250. Since there are around 20 hemozoin crystals per infected erythrocyte, the corresponding N_{HC} is 5000. Considering the volumes of these particles ($V_{i-RBC}=90\mu\text{m}^3$, $V_{HC}=0.022\mu\text{m}^3$) and the minimum measurable $\Delta R/R_0$ (i.e. $\sim0.1\%$), with Eq. (2.25) we can estimate the maximum sensing volume of the electrodes (V_{el}) on the chip that allows to detect the number of i-RBCs corresponding to the LOD. The resulting volumes are $3.38\cdot10^7\mu\text{m}^3$ for i-RBCs and $1.65\cdot10^5\mu\text{m}^3$ for hemozoin crystals.

The sensitive volume is the portion of space above the electrodes where the presence of a particle can be detected; the height of this region H is usually similar to the electrodes width W[80]. If we consider circular electrodes like the one represented in Figure 3.1, with spacing S, width W and height of the sensitive volume H all equal to 2 μm, the maximum sensitive area of the electrodes (A_{el}) will be $1.69\cdot10^2\mu\text{m}^2$ for i-RBCs and $8.25\cdot10^2\mu\text{m}^3$ for hemozoin crystals. Therefore, it is fundamental to attract these particles in localized regions, corresponding to the sensitive area of the electrodes, represented as a shaded region in Figure 3.1. The magnetic system designed to reach this result is presented in the following section.
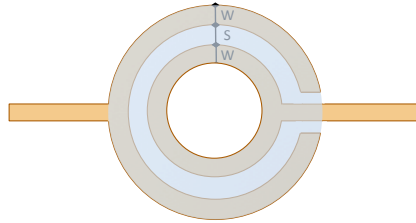
Figure 3.1: Sketch of the geometry of one of the electrodes used to detect magnetically captured particles. The shaded region indicates the sensitive area of the electrode.

3.2 Magnetic simulations

In the design phase of the device, simulations were performed using *COMSOL Multiphysics*[59], a cross-platform finite element analysis, solver and multiphysics simulation software. Through numerical simulations it was possible to study different geometries and figure out which ones would better fit the requirements we were looking for. At the beginning, the idea was

to implement magnetic concentration and impedance detection in the same layer, through electrodes made of a magnetic material. Then, a different design was implemented, where magnetic and electrical parts were separated. Indeed, in this configuration a more specific optimization is possible, that allows to obtain better results from both processes. The main results of electrical simulations, carried out by Prof. Marco Sampietro's group, have been reported in section 2.4, while magnetic simulations will be described in detail in the following sections.

3.2.1 Preliminary analysis

COMSOL Multiphysics allows to model different physical problems combining several modules. In simulations concerning magnetic attraction two of them were used: *Magnetic fields, no currents*, to investigate magnetostatic behavior of the ferromagnetic structures (i.e. nickel concentrators and external permanent magnets), and *Particle tracing*, to study the motion of particles subjected to different forces (gravity, buoyancy, drag and magnetophoretic forces in this case). Brownian motion is not included in the simulation platform designed to find the optimal geometry because, according to simulations performed with simple patterns, it does not cause relevant changes on the motion of the analyzed particles, i.e. hemozoin crystals and infected RBCs.

The aim of the magnetic concentrators layer is to capture on the chip surface the magnetic particles present in the analyzed blood sample and concentrate them in specific areas, such that their strongly increased local number is able to cause an intense impedance variation and thus a measurable electrical signal. So far, a total active chip area in the order of 0.5 cm^2 and a 500 μm-thick blood drop have been considered, thus a magnetic system that allows attraction over several hundreds of μm in vertical direction is required as well.

A sufficiently high $\nabla H^2(\mathbf{x}_c)$ is required to attract magnetic particles, as explained in section 2.3. The minimum value needed for lifting hemozoin crystals is $\sim 2 \cdot 10^{13}$ A^2/m^3, while the minimum for i-RBCs is $\sim 9 \cdot 10^{14}$ A^2/m^3. Different examples of trapping and manipulation of magnetic particles can be found in literature[40,42,81,82], where micro- and nano-structures are used to produce locally-intense gradients (e.g. exploiting magnetic domain walls). However, the effect of structures like these is localized in space and not sufficient to interact with magnetic particles that are hundreds of μm away. Therefore, a multi-dimensional approach was considered in the proposed device, using the ∇H^2 provided by macroscopic permanent magnets for a

long-range attraction and the one produced by nickel microstructures for short-range localized capture. Since magnetic field gradient increases as the size of the magnetic source downscales, the interactions between the particles of interest and the magnetic field can be significantly enhanced close to the chip substrate due to the micro-concentrators. These two elements have very different size scales (cm for permanent magnets, μm for nickel concentrators), so their magnetic properties and effects on particles motion are analyzed in separate simulations, with some approximation for the region of space where they coexist with comparable magnitude.

3.2.2 External permanent magnets

A finite-dimension cylindrical permanent magnet generates a slightly non-uniform magnetic field due to edge effects, thus providing a certain ∇H^2. To enhance this phenomenon, a different configuration for the magnets, shown in Figure 3.2, has been developed: a central cylinder surrounded by a polar array of parallelepipeds, magnetized in opposite direction with respect to the cylinder. Magnetic field lines arising from the cylinder bend and close on parallelepipeds, thus increasing non-uniformity. According to simulations, this new configuration lead to an almost 90% enhancement of the vertical component of ∇H^2 provided in the region where the analyzed blood sample is located. The obtained value using Neodymium Iron Boron ($Nd_2Fe_{14}B$) permanent magnets in this configuration is $\nabla H^2{}_z \sim 2 \cdot 10^{14}$ A^2/m^3. Moreover, the z-component is four orders of magnitude larger than the radial one ($\nabla H^2{}_r$, in the (x, y) plane), so external magnets contribute to vertical attraction but not significantly to concentration.
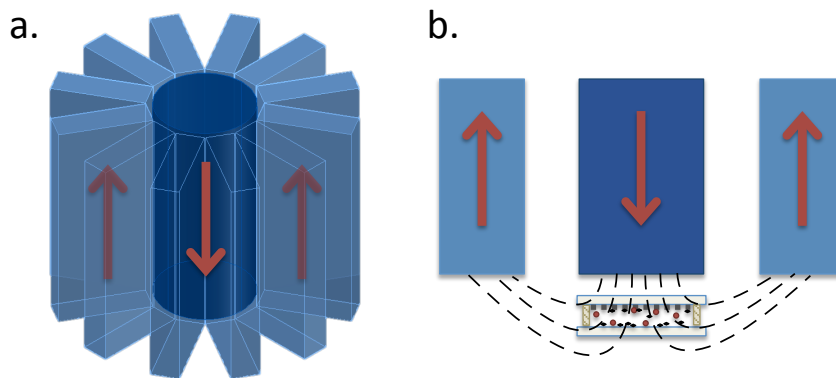
Figure 3.2: a. 3D Sketch of the external permanent magnets setup. Red arrows indicate the magnetization. **b.** Section view of external magnets and chip. Black dashed lines represent magnetic field lines, red arrows the magnetization.

3.2.3   Micrometric nickel concentrators

Coming to the ferromagnetic concentrators, in section 1.2.1 different magnetic separation setups with ferromagnetic wires magnetized by external permanent magnets were presented[21,48,49,53]. Following this idea, the first investigated geometry for the concentrators was an array of nickel bars, with a micrometric section and a length in the order of some millimeters. Despite this kind of structure was able to efficiently attract magnetic particles, it could not concentrate them in sufficiently localized areas. As a matter of fact, spatial concentration is crucial because, as discussed in section 2.4, the impedance signal is proportional to the volumetric fraction, i.e. the ratio between the volume of captured particles and the sensing volume above the electrodes. Without concentration, the electrodes should be too extended and the volumetric fraction for the same number of captured particles would significantly decrease, with detrimental impact on the sensitivity. Thus, concentrators with different shapes were simulated in order to obtain satisfactory results for both attraction and localized capture. The final geometry is an array of micrometric cylinders, with a 20 μm height and different values of diameter and spacing between them. Choosing specific geometrical parameters is not easy, since many (sometimes competitive) factors need to be considered. Indeed, reducing the spacing between cylinders allows a more effective attraction, but particles are concentrated in a higher number of points. The effective area of the electrodes needed to sense the particles on top of each concentrator would increase, thus reducing the electrical signal (see section 3.1). Moreover, using cylinders with higher aspect ratio (i.e. the ratio between height and diameter), capture efficiency can be increased but the pillars fabrication process becomes more complex (see section 5.2). Although different geometries were simulated and/or tested with real devices, the final layout will be optimized only after combined experiments of capture and detection, which are beyond the scope of this thesis. The numerical analysis presented here will be focused on geometries similar to the patterns of the samples used in magnetic capture experiments presented in section 5.3, i.e. pillars with a diameter d=20 μm arranged in a hexagonal lattice with spacing (i.e. distance between the centers of neighboring cylinders) s=60 μm or 80 μm. Also arrays of pillars with d=40 μm and s=160 μm have been considered. For all the concentrators the height h is 20 μm.

Nickel is a very soft material, i.e. it is easily magnetized and demagnetized. The application of a vertical uniform 0.9 T magnetic field, provided by external magnets, makes the magnetic moments of the nickel concentrators align in the vertical direction (out of plane), until complete saturation
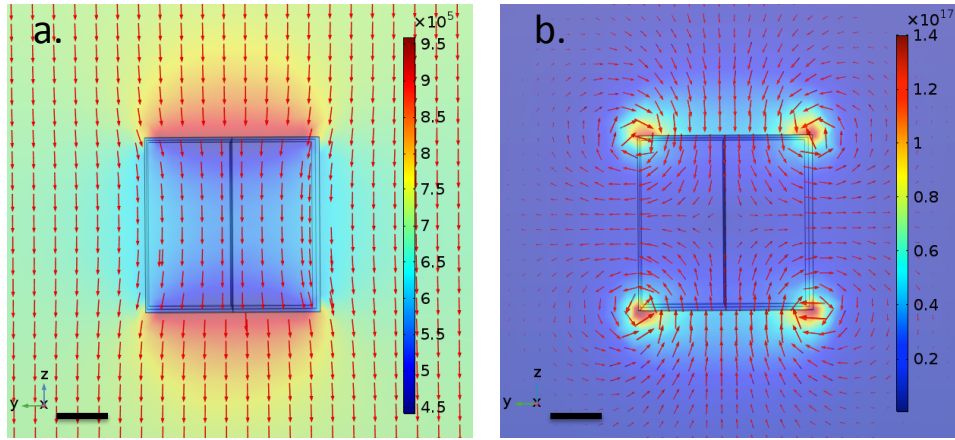
Figure 3.3: Representation with 2D color plots of the norm of **H** (**a.**) and ∇H^2 (**b.**) produced in an axial plane around a *Ni* pillar with $d=h=20$ μm, due to a uniform external field and the pillar itself. The arrows indicate the direction of the vectors and their lengths are in logarithmic proportion with the vector modulus. The scale bars are 5 μm. Images obtained with *COMSOL Multiphysics*

is reached. The minimum external field required to make the magnetization saturate along the hard axis due to shape anisotropy, i.e. $\mu_0 M_S$, is 0.6 T for nickel[48,49] but, since fabricated pillars do not have a well defined anisotropy axis, this threshold value is even lower. Thus, the applied field is sufficiently intense to reach complete saturation. The external field due to permanent magnets was considered uniform because, as a first approximation, its variation over the characteristic size of the concentrators (i.e. few μm) can be neglected. Although in the real field configuration produced by the external magnets in Figure 3.2 the applied field is not the same for all the pillars, their magnetic behavior is not strongly affected because saturation is achieved in all the concentrators within the active area of the chip. The total **H** field produced around a nickel pillar with $d=h=20$ μm due to the combined action of the external uniform field and the concentrator itself is shown in Figure 3.3a.

3.2.4 Magnetic field gradient

The purpose of the nickel microstructures and the external permanent magnets is to attract magnetic particles, thus an important parameter to investigate is ∇H^2, which is proportional to the magnetic force (see Eq. (2.14)). Its norm around a nickel concentrator is represented in Figure 3.3b. However, not only its norm but also value and direction of its components at different distances from the pillars are relevant quantities. A representation of how
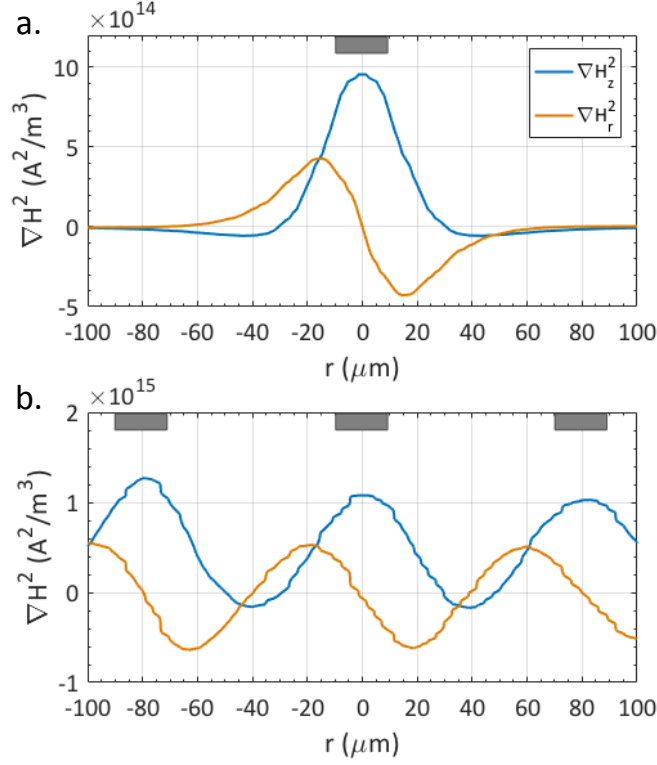
Figure 3.4: Variation of the components of ∇H^2 as a function of the radial distance, calculated for a single 20 μm element(**a.**) and for an array of the same elements with a 80 μm spacing (**b.**). The curves are plotted along horizontal lines intersecting the cylinders axis, at a vertical distance $z=30$ μm from the pillars. The gray boxes indicate the positions of the micro-concentrators.

its radial (∇H^2_r) and vertical (∇H^2_z) components change, moving in radial direction from the center ($r=0$) of a single nickel cylinder with $d=20$ μm up to $r=\pm100$ μm, at a fixed vertical distance from the chip surface ($z=30$ μm), is provided in Figure 3.4a. The positive z-component (blue line) indicates an attractive force towards the pillar up to r ≈ 30 μm, more intense closer to its center. The r-component (orange line) changes sign, indicating that it is directed towards the cylinder axis; in absolute value, it is more intese closer to the edges of the pillar. The effect of the addition of the contributions due to different concentrators is shown in Figure 3.4b, where the same quantities are calculated for an array of 20 μm-diameter pillars with a 80 μm spacing (center-to-center distance).

Another useful information is provided by the trend of ∇H^2_z as a function of the vertical distance from the chip surface z, represented in Figure 3.5 considering its value along a vertical line coincident with the cylinder axis
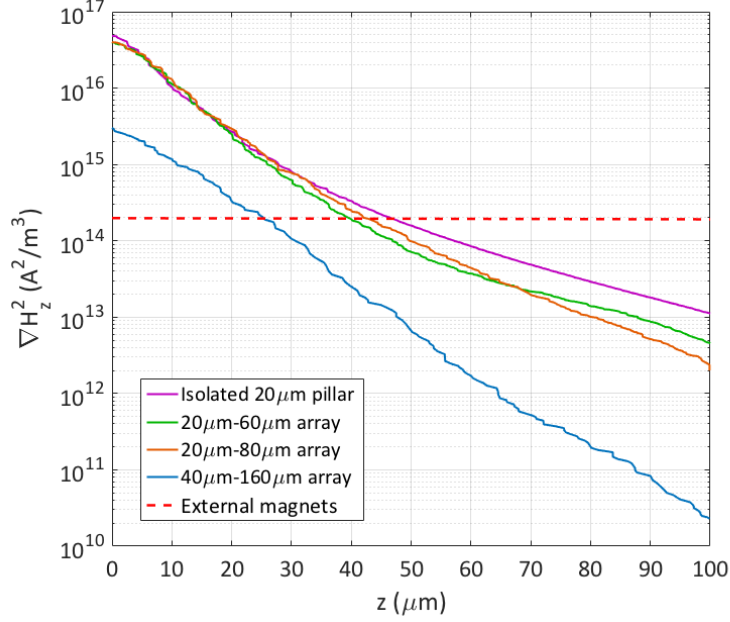
Figure 3.5: Variation of $\nabla H^2{}_z$ as a function of the vertical distance from the chip surface, calculated along the cylinder axis (i.e. r=0), for an isolated element and for pillars inside different arrays, as indicated in the legend. Data for the system of external magnets are obtained along a direction perpendicular to the plane, at the chip center.

(i.e. r=0). Within 100 μm from the chip surface the value of $\nabla H^2{}_z$ due to the concentrators changes of almost four orders of magnitude for the 20 μm pillars and around six orders of magnitude for the 40 μm ones; indeed, the z component of the gradient provided by the concentrators has a relevant role only close to the microstructures. The contribution due to a single cylinder with d=20μm (magenta line) and the ones due to arrays of the same pillars with a 60 μm (green line) and 80 μm spacings (orange line) are similar up to $z \approx$40 μm, then the arrays result slightly less effective. On the contrary, the array of pillars with d=40μm and spacing 160 μm (blue line) shows a much different behavior. Not only ∇H^2 decreases more intensely over the analyzed region, it has also an initial value more than one order of magnitude smaller with respect to the other structures. Indeed, these pillars have an aspect ratio ($h : d$) of 1:2, which results less effective with respect to the 1:1 associated to the 20μm structures.

Conversely, $\nabla H^2{}_z$ generated by the system of permanent magnets (dashed red line) can be considered constant in z, as a first approximation, within a distance form the chip surface of a few hundreds of μm. Indeed, its variation

Properties	Hemozoin	i-RBCs	Beads
$\Delta\chi$	$3.20 \cdot 10^{-4}$	$1.80 \cdot 10^{-6}$	~ 1
Radius (μm)	0.18	2.78	0.15
Volume (μm^3)	$2.20 \cdot 10^{-2}$	90.0	$1.41 \cdot 10^{-2}$
Mass density (kg/m^3)	1490	1125	1490
Mass (pg)	$3.28 \cdot 10^{-2}$	101	$2.11 \cdot 10^{-2}$

Table 3.1: Magnetic, geometrical and physical properties of hemozoin crystals, red blood cells and superparamagnetic beads considered in *COMSOL Multiphysics* simulations.

is extremely small if compared to the concentrators', as the order of magnitude does not change. This consideration is valid not only for the vertical distances examined in Figure 3.5, but in the whole region of interest for the detection, i.e. z=0–500 μm from the chip surface. Moreover, $\nabla H^2{}_z \approx \nabla H^2$ because the radial component (not represented), basically constant as well, is four orders of magnitude smaller. Therefore, the magnetic force due to permanent magnets $\mathbf{F}_M{}^{ext}$ acting on particles inside the blood sample can be considered constant, due to its relation with ∇H^2 (see Eq. (2.14)).

The value of magnetic force is largely dependent on the properties of the targets, while ∇H^2 is a more objective parameter that can be used to quantify the attraction capabilities of different magnetic structures. For example, Chen et al.[46] used a system similar to ours, with a permanent magnet and an array of nickel microstructures (200 nm-thick parallelepipeds), to separate cancer cells labeled with superparamagnetic particles. The maximum $\nabla H^2{}_z$ they achieved at z=5 μm from the surface is $\approx 10^{12}$ A^2/m^3, more than four orders of magnitudes lower with respect to the one provided by our system, and nearly null for larger distances. Thus, the magnetic structure we designed can be of great interest not only for malaria detection, but also for other devices where magnetic separation is required.

3.2.5   Magnetic force

On the other hand, calculating the magnetic force may be useful in order to compare it with other contributions, like gravity and drag forces. Thus, using Eq. (2.14), we calculated the vertical component of the magnetic force provided by micrometric concentrators and external magnets simply multiplying $\nabla H^2{}_z$ (Figure 3.5) by a factor $\frac{\mu_0}{2} V_p \Delta\chi_p$, depending on geometric and magnetic properties of the particles. These properties are summarized in Table 3.1, together with others that may be relevant when comparing mag-
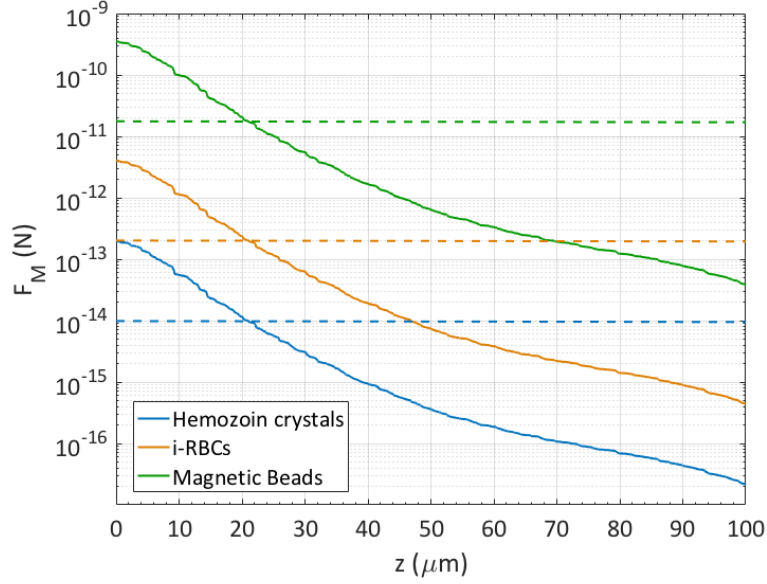
Figure 3.6: Magnetic force variation as a function of the vertical distance from the chip surface for hemozoin crystals, infected red blood cells and superparamagnetic beads. Continuous curves refer to a pillar inside an array (d=20 μm, s=60 μm) and are plotted along a vertical line coincident with the cylinder axis; values were calculated starting from of $\nabla H^2{}_z$ represented in Figure 3.5. Dashed lines refer to the force produces by the external gradient used in simulations, i.e. $2{\cdot}10^{15}$ A^2/m^3.

netic force with other contributions. Besides hemozoin crystals and infected red blood cells, the particles of interest for the detection systems, magnetic force was calculated also for 300 nm superparamagnetic beads because they were used in capture experiments to study the magnetic attraction capability of the designed system, as described in section 5.3. The variation of the magnetic force produced by a micrometric concentrator (continuos lines) on these three kinds of particles as a function of the vertical distance from the chip surface z is represented in Figure 3.6. Magnetic force on the considered superparamagnetic beads is more than a thousand times higher than the force on hemozoin crystals and almost a hundred times higher than the one on i-RBCs.

Micrometric concentrators contribute in a negligible way to the magnetic force at large distances from the chip, so in this region magnetic force due to external magnets ($\mathbf{F}_M{}^{ext}$) alone must be sufficiently intense to make the particles move towards the chip. Then, once close enough to be affected by the presence of nickel microstructures, they should be concentrated and captured in specific areas of the pillars. In section 2.3 a condition for the

minimum ∇H^2 needed to have a positive velocity of the particles in the upward direction was calculated (Eq. (2.18)). Since this condition should be valid for all the particles in the region of the analyzed samples, i.e. up to a distance of 500 μm from the chip surface, it results in a requirement for the minimum ∇H^2 that needs to be provided by the external magnets. The system of permanent magnets used in capture experiments is able to create a gradient of $\sim$2$\cdot$10^{14} A^2/m^3, higher than the minimum required for lifting hemozoin crystals ($\sim$2$\cdot$10^{13} A^2/m^3) but lower than the minimum for i-RBCs ($\sim$9$\cdot$10^{14} A^2/m^3). Therefore, a different external system of magnets should be designed to achieve sufficiently intense values of ∇H^2. In the simulations performed to investigate the feasibility of the capture system in reverse configuration a higher ∇H^2, i.e. 2$\cdot$10^{15} A^2/m^3, was used. This value, which is about double with respect to the minimum needed for i-RBCs, allows to obtain also reasonable times (around 10 minutes) for the lifting of the most distant particles up to a region where the nickel concentrators contribute in a relevant way to attraction ($\sim$50μm). The horizontal dashed lines in Figure 3.6 correspond to the magnetic force generated on hemozoin crystals, RBCs and beads considering the external gradient value used in simulations. According to this graph, the magnetic force due to the concentrators at 50 μm is less that 10% of the one related to the gradient provided by the external magnets and even lower at further distances, thus the action of nickel pillars can be considered negligible, as a first approximation, for z>50 μm.

3.2.6 Particles motion

The 500 μm-height sample can be separated in two different areas, represented in Figure 3.7: a region extending up to z=50 μm from the chip surface, with a relevant contribution due to nickel pillars, and the remaining volume, where only the other forces (i.e. $\mathbf{F}_M^{ext}$, $\mathbf{F}_{G-B}$ and $\mathbf{F}_D$) can be considered. While the magnetic force produced by the nickel microstructures is strongly dependent on z, the other terms are basically constant in the whole volume. Therefore, the dynamic problem in the region far from the pillars (i.e. z=50–500 μm) can be solved analytically, as a first approximation, considering a constant value of ∇H^2=2$\cdot$10^{15} A^2/m^3 in Eq. (2.16). Under these assumptions and with a sufficiently high external ∇H^2, magnetic particles (i.e. hemozoin crystals and i-RBCs) are lifted up, moving at their steady-state velocity $\bar{\mathbf{v}}$ until the contribution of nickel pillars becomes relevant.

Conversely, numerical simulations are required to analyze in detail the particle trajectories close to the chip surface (i.e. z=0–50 μm). Due to the
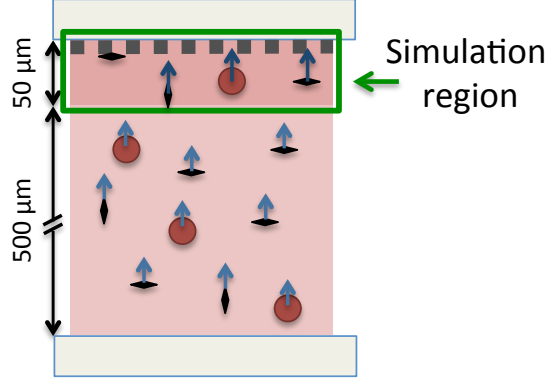
Figure 3.7: Sketch of the two regions considered within the blood sample. Light blue and dark blue arrows indicate the net force acting on hemozoin crystals and i-RBCs, respectively far from the chip and in its proximity. Dimensions are not in scale.

periodicity of the nickel pillars array, it is possible to understand the behavior of the system studying just a portion of it instead of the whole chip area, i.e. considering a reduced number of cylinders. Thus, simulation environment can have micrometric dimension. Also the effects of the other constant forces need to be taken into account inside the *Particle tracing* simulations. There is a specific section for drag force, while the net contribution of the magnetic force due to external magnets $\mathbf{F}_M^{ext}$ and $\mathbf{F}_{G-B}$ can be considered through a constant acceleration $\mathbf{a}_{TOT}$, used instead of $\mathbf{g}$ in the gravitational force section. It can be expressed as:

$$\mathbf{a}_{TOT} = \frac{\mathbf{F}_{TOT}}{m_p} = \frac{\mathbf{F}_M^{ext} - \mathbf{F}_{G-B}}{m_p} \tag{3.1}$$

where $\mathbf{F}_{TOT}$ is the net force acting on a magnetic particle with mass m_p due to gravity, buoyancy and magnetic force provided by external magnets. The value $\mathbf{a}_{TOT}$ depends on ∇H^2 and it will be much higher for hemozoin crystals because their sedimentation contribution $\mathbf{F}_{G-B}$ is a thousand times smaller than the one of RBCs.

At the beginning of the analysis, i-RBCs and hemozoin crystals are dispersed inside the whole blood sample volume, i.e. some close and other distant from the surface. Using the model previously described and illustrated in Figure 3.7, we were able to simulate the behavior of both categories of particles, considering their trajectory from $z=50$ μm up to the chip surface. For particles already in the proximity of the chip surfaces (i.e. $z<50$ μm) at the beginning of the test a null initial velocity was considered, while for

the more distant ones, lifted up due to the contribution of external magnets, an initial velocity $\bar{\mathbf{v}}$ was assumed. The results of the simulations performed under these conditions (i.e. initial velocity equals to 0 or to $\bar{\mathbf{v}}$) for hemozoin crystals and i-RBCs are shown in Figure 3.8a and Figure 3.8b, respectively. The analyzed structure is a HCP (hexagonal close packed) array of 20 μm diameter pillars with a 60 μm spacing. The condition on the initial velocity does not affect significantly the attraction mechanism or its timing, indeed in both situations almost all hemozoin crystals are captured within 5 minutes and almost all i-RBCs in less than 10 minutes. Considering also the lifting time required to attract the distant particles in the proximity of the concentrators (i.e. $\sim$10 minutes), the maximum capture time is in the order of 15–20 minutes.
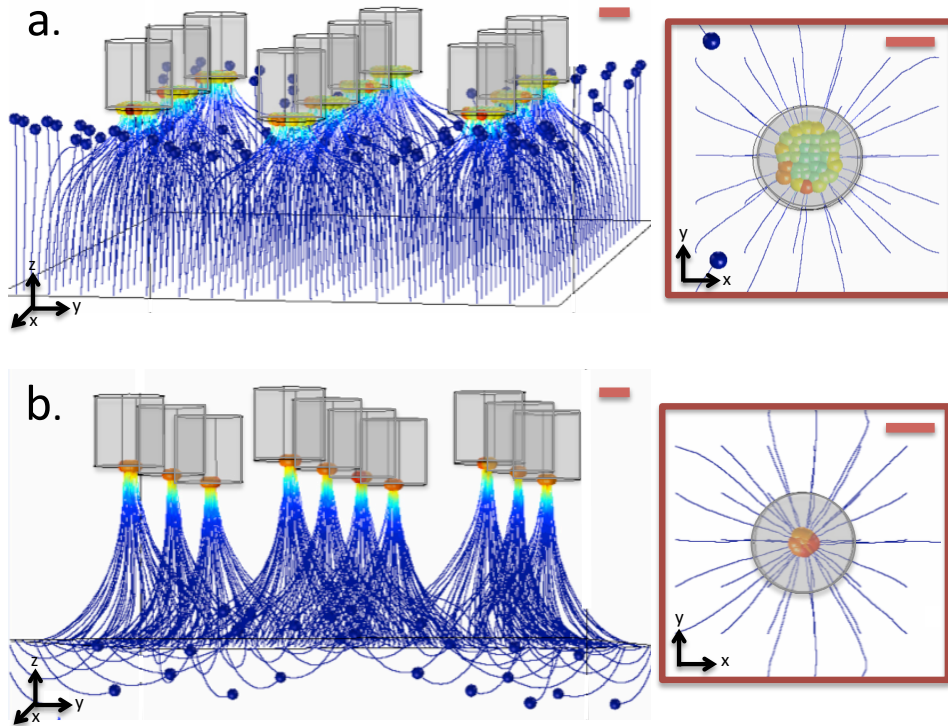
Figure 3.8: Representation of the trajectories of hemozoin crystals (**a.**) and infected red blood cells (**b.**), released at z=50 μm from the chip surface. Figures on the left present a 3D view, figures on the right a detail of a pillar top view. The scale bars are 10 μm; particle dimensions are not in scale. Images obtained with *COMSOL Multiphysics*.

The simulation platform used to study the feasibility of the capture system was validated by simulating structures used in real experiments, considering a direct geometry (chip and external magnets below the blood sample) and a value for $\mathbf{F}_M{}^{ext}$ corresponding to the ∇H^2 actually provided by the system of external magnets currently in use (i.e. $2 \cdot 10^{14}$ A^2/m^3). This second set of simulations is discussed in more details in section 5.3.

3.3 Design of the chip layout

In the final device, magnetic capture elements and electrodes are integrated to allow the detection of hemozoin crystals and infected erythrocytes. As discusses in section 3.1, the maximum sensing area of the electrodes on the chip that allows to detect the number of malaria biomarkers corresponding to the limit of detection is $1.69 \cdot 10^2 \mu$m^2 for i-RBCs and $8.25 \cdot 10^2 \mu$m^3 for hemozoin crystals. In order to attract and concentrate these particles in specific areas, the external system of permanent magnets (for long-distance attraction) and the micrometrical nickel concentrators (to create an intense and directional ∇H^2 in the proximity of the surface) are used, as described in section 3.2. The sensing area of the electrodes must correspond to the region where hemozoin crystals and i-RBCs are magnetically concentrated. According to the simulations, particles are attracted in the center of the pillars, therefore in the initial phase interdigitated electrodes with a sensitive area corresponding to these regions were considered. However, since tests on real devices showed a preferential capture localized mainly along the edges of the pillars, the design of the electrodes geometry has been changed accordingly. Indeed, circular electrodes like the one represented in Figure 3.1 were adopted.

The constrain on the maximum sensing area of the electrodes is closely related to magnetic capture, mainly to number and dimension of the attraction regions. Indeed, the total dimension of the nickel concentrators and the extent of their surface upon which particles are captured determine the geometrical parameters of the electrodes, which are located along the pillars edges. Furthermore, arrays with different spacings between the pillars can be considered. To guarantee an attraction of all the particles, the spacing must be less or equal to the double of the capture radius of the concentrators, i.e. the maximum distance in the horizontal plane starting from their center within which all particle are captured. Thus, the total number of attraction spots (i.e. Ni pillars) changes according to the distance between the array elements. Many dependent parameters can be modified, thus different design solutions respecting the constrains on maximum sensing area can be found.
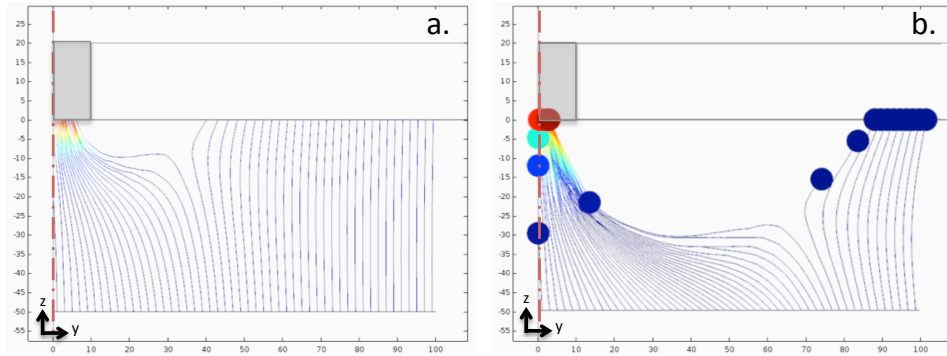
Figure 3.9: View of the radial capture efficiency of a *Ni* pillar for hemozoin crystals (**a.**) and infected red blood cells (**b.**) released at $z=50$ μm from the chip surface. The images are radial sections of the 3D structures and are obtained with *COMSOL Multiphysics*.

In one of these possible solutions, a total chip sensing area of 0.5 cm^2 (i.e. total area 1 cm^2) and a 500 μm-thick blood drop are considered, thus resulting in 25 μl of volume above actual measurement electrodes. For nickel cylinders with a 20 μm diameter, the sensing area of circular electrodes with $W=S=H=2$ μm, located along the pillars edges, is 264 μm^2. Moreover, the maximum capture radius of pillars with this diameter and a 20 μm height is around 40 μm from the cylinder axis for hemozoin crystals and around 80 μm for i-RBCs, as results from simulations showed in Figure 3.9. Thus, the maximum period of the array that guarantees a complete particle capture is ∼80 μm for hemozoin crystals and ∼160 μm for i-RBCs. Capture radius is reduced for hemozoin crystals due to the intense almost uniform magnetic force provided by the external magnets. Despite even a lower gradient would allow to move these particles upwards, the associated time required for the lifting of hemozoin crystals far from the chip surface would be too long.

The minimum number of concentrators required to have a 100% capture is obtained dividing the total chip sensing area by the area of the cell associated to each pillar. Thus, at least 9.02·10^3 and 2.26·10^3 nickel concentrators must be present to capture all hemozoin crystals and i-RBCs, respectively. Multiplying this value by the sensing area of each pillar, total electrodes sensing areas of 2.38·10^6μm^2 for hemozoin crystals and of 5.95·10^5μm^2 for i-RBCs are obtained. Using Eq. (2.25), the resulting $\Delta R/R_0$ is 0.003% for hemozoin crystals and 2.8% for i-RBCs. Unfortunately, an amount of hemozoin crystals corresponding to the limit of detection cannot be measured in these conditions, as the estimated $\Delta R/R_0$ is lower than the minimum value that can be obtained with the experimental conditions used so far (∼0.1%).

Thus, capture and electrical systems need to be further optimized in order to reach the minimum detectable signal also for hemozoin crystals. Indeed, some geometrical parameters can be varied, as electrodes geometry, nickel concentrators dimension and spacing. Moreover, also the magnetic capture mechanism can be improved, e.g by using an additional in-plane magnetic field to further concentrate particles in two spots located at the opposite sides of the pillar diameter. This configuration would result in a different shape of the electrodes, with a reduced sensitive area. Therefore, the next steps of the TID MEKII project are related to the investigation of the feasibility of these alternative solutions with the developed simulation platforms and tests on fabricated devices.

Chapter 4

Experimental techniques

In this chapter an overview of the experimental techniques exploited for the microfabrication of the devices developed in this thesis is presented, together with the characterization techniques used to analyze the properties of hemozoin crystals. In addition, the experimental setup and the treatment protocol for red blood cells used in capture experiments are described.

4.1 Microfabrication techniques

This section presents the microfabrication techniques exploited in the development phase of the device: optical lithography to properly pattern the sample, reactive ion etching to create deep cavities, electron beam evaporation to deposit nickel and silicon dioxide, electroplating to grow nickel pillars and sputtering to deposit gold electrodes.

4.1.1 Photolithography

Photolithography or optical lithography is a microfabrication method that allows to pattern a sample, exploiting the change in solubility of a suitable polymer, called photoresist, when it is exposed to UV light. Images on the sample can be created using a photomask or a maskless system. Photomasks are typically fabricated from a chromium film on a transparent quartz substrate. The desired pattern is defined because the resist areas below Cr are protected from the UV light, while the others are exposed. Instead of masking the areas that must not be exposed, a focused laser beam with proper wavelength can be exploited to directly write the image into the photoresist. This kind of maskless lithography allows to change patterns in a more flexible way, without the cost of generating a new photomask, but can be much slower if large areas need to be exposed. In both cases, after UV
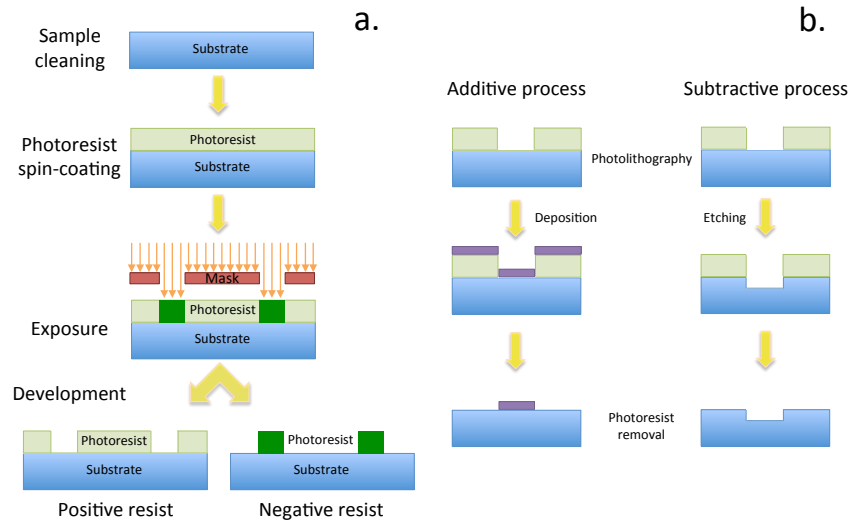
Figure 4.1: a. Optical lithography steps for positive and negative photoresists. **b.** Pattern transfer processes.

irradiation the resist presents soluble and non-soluble areas. In the development step, a suitable solvent called developer removes the soluble zones without affecting the non-soluble ones, thus reproducing the pattern on the sample. Finally, to efficiently fabricate a structure with the desired pattern, the areas unprotected by the resist can be covered with additional material (additive process) or etched away (subtractive process). The main steps of a lithographic process and the following pattern transfer are represented in Figure 4.1.

Sample cleaning. It is fundamental to have a clean surface, otherwise quality of the pattern and photoresist adhesion can be negatively affected. The standard cleaning procedure consists in an ultrasonic bath in acetone and a subsequent isopropyl alcohol rinsing.

Photoresist spin-coating. To properly spread the photoresist on the whole sample and produce a uniform layer, spin coating is used. Then, to allow the complete evaporation of the solvent containing the polymer and the enhancement of resist adhesion on the sample surface, a soft baking is performed.

The devices presented in this thesis have been fabricated exploiting three photoresists: AZ5214E (Microchemicals-USA), a fluid resist with image reversal capability, AZ40XT (Microchemicals-USA), a viscous thick positive resist, and SU8 2005, a permanent negative epoxy resist.

AZ5214E is spin coated at 6000 rpm for 60 s and baked at 110°C for 90 s; the resist thickness obtained with this procedure is 1.2 μm. AZ40XT is spin coated at 2750 rpm for 45 s and baked at 120°C for 7 minutes, thus obtaining a thickness around 20 μm. Baking is a critical step for thick photoresists. Heating has to be gradual otherwise too strong temperature gradients would imply the creation of bubbles or cracks in the resist; for the same reason a 10-15 minutes rest is required after each baking. Finally, SU8 2005 is spin coated at 4000 rpm for 30 s and baked at 95°C for 3 minutes; the resist thickness obtained is 5 μm. To improve the resist adhesion to the substrate, a primer can be previously applied. For AZ40XT on nickel surface, we used a Ti prime primer (Microchemicals-USA), deposited on the sample surface with spin coating at 4500 rpm for 45 s and then baked for 120 s at 120°C.

Exposure. UV radiation alters the photoresist chemical properties, resulting in a different solubility of the exposed and non-exposed areas. Two different kinds of photoresists can be distinguished: positive resists, where exposed zones are made more soluble and can be removed using a proper developer, and negative resists, where the areas the mask lets exposed are made less soluble and will be preserved. However, some resists may have image reversal capability, i.e. they can behave as positive or negative resists according to the performed process[83]. For positive resists the UV light provides the energy required to break the polymeric chains, enhancing the solubility of the photoresist in the exposed area and consequently favoring its removal during the development step. Conversely, in negative resists exposure to UV radiation initiates a chemical cross-linking reaction (i.e. polymerization), that requires also a subsequent baking to be concluded. As a result, the exposed cross-linked areas become less soluble in developer with respect to the unexposed ones. To obtain the same result with image reversal resists, a flood exposure (without a mask) is required before the development. Light that penetrates through the resist layer is attenuated due to the absorption of the photoactive compound; the result is a higher intensity at the top and a lower one at the bottom of the resist. Thus, a positive photoresist profile usually has a positive slope of 75-85°, only sub-micron resists get close to 90°. For negative resists (or image reversal resist properly processed), the process is inverted, as higher exposed areas will be cross-linked to a higher degree than those with lower dose; thus, the final result will be a negative wall profile ideally suited for lift-off[83].

AZ5214E can show image reversal capability, with exposure dose 23 mJ/cm^2, reversal bake (most critical step) at 115°C for 90 s and a flood exposure of 500 mJ/cm^2 (uncritical). AZ40XT has an exposure dose of 369 mJ/cm^2 and requires also a post exposure bake at 105°C for 100 s to complete the photoreaction and make the resit developable. Also in this case the heating needs to be gradual and the cooling in air must be sufficiently long, otherwise the resist would crack coming in contact with the developer. SU8 2005 has an exposure dose of 700 mJ/cm^2 and requires also a post exposure bake at 95°C for 2 minutes to allow cross-linking.

The machines employed in this work are *Karl Suss Mask Aligner MA6*, where UV radiation is provided by the I-line (at 365 nm) of a mercury lamp with an intensity around 5 mW/cm^2, and *Heidelberg Instruments Maskless Aligner MLA100*, that has a LED source with a power of 10 W at 365 nm. They both allow for the exposure of wafers up to 6 inches diameter.

Development. An appropriate solvent, called *developer*, is used to remove the soluble part of resist, without affecting the non-soluble ares. For positive resist the exposed areas are dissolved, while the zones protected by the mask during exposure remain on the substrate; for a negative resist the mechanism is the opposite (non-exposed areas are more soluble). Both AZ5214E and AZ40XT are developed in AZ726MIF (Microchemicals-USA), respectively for 90 s and 35 s, and subsequently rinsed in water. SU8 2005 development phase is peculiar, since there is not a specific duration of the procedure: after an actual few-seconds development phase, the sample should be rinsed with isopropyl alcohol and then developed again if it shows a white film due to the presence of underdeveloped unexposed photoresist. This operation must be repeated until the white film is not produced any more.

Pattern transfer. After the development, the pattern can be fixed on the sample through the removal (etching procedures) or addition (deposition) of material on the areas not covered by the photoresist. Finally, the resist is completely removed from the sample; this procedure is called *lift-off* if it follows an additive process. Resist removal is performed in acetone or in different solutions (e.g. AZ100 remover, Microchemicals-USA) for AZ photoresists. Conversely, SU8 2005 is really difficult to remove, thus it is particularly suited for permanent applications.

4.1.2 Reactive Ion Etching
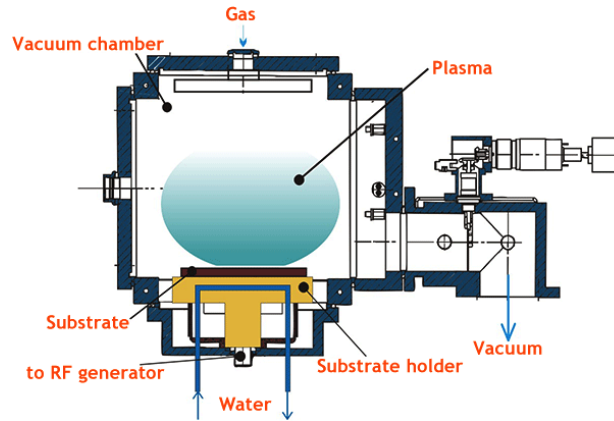
Figure 4.2: Sketch of a Reactive Ion Etching machine[84].

Reactive-ion etching (RIE) is a dry etching technology that uses chemically reactive plasma, generated in vacuum by an electromagnetic field, to remove material from a sample. Unlike wet etching, this process is very directional, it is strongly performed in the vertical direction (downward) and purposefully minimized in the horizontal one to leave clean accurate corners.

In a typical RIE system (Figure 4.2) a wafer is situated in the bottom portion of a cylindrical vacuum chamber and it is electrically insulated from the chamber itself. Gas enters through small inlets in the top of the chamber and exits to the vacuum pump system through the bottom. Different types and amounts of gas are used according to the process, while the pressure is typically maintained in a range between a few mtorr and a few hundred mtorr. Plasma is initiated in the system by applying a strong RF (radio frequency) electromagnetic field to the wafer platter, usually with a frequency of 13.56 MHz and a power of a few hundred W. The oscillating electric field ionizes the gas molecules by stripping them of electrons, thus creating a plasma. In each field cycle electrons are electrically accelerated up and down in the chamber, while the movement of much more massive ions is relatively little influenced by the RF electric field. Electrons that are absorbed into the chamber walls are fed out to ground and so removed from the system; conversely, the ones that impinge on the wafer platter cause it to build up charge due to its DC isolation and so a large negative voltage is developed on the platter. Therefore, since the plasma itself develops a slightly positive charge due to the higher concentration of positive ions compared to free electrons, a large voltage difference arises. This voltage difference makes the positive ions drift toward the wafer platter, where they collide with the

sample surface and etch it. This process combines a physical etching (high-energy ions can transfer some of their kinetic energy to the surface atoms and sputter them) with a chemical etching, i.e a selective erosion caused by the chemical interaction between the ions in the plasma and the surface to be etched. Indeed, according to the gas used in the process, reactive ions of different species are accelerated towards the sample and etch its surface at different rates according to the materials present. Usually the portion of the sample that doesn't need to be etched is masked with a material with a much smaller etching rate, like metals or photoresists.

When deep steep-sided holes and trenches, typically with high aspect ratios, need to be created inside substrates, a highly anisotropic etch process called deep reactive-ion etching (DRIE) is required. One of the possible technologies to perform DRIE is the so-called *Bosch process*, where a standard nearly isotropic plasma etch is alternated with the deposition of a chemically inert passivation layer, that protects the entire substrate from further chemical attack and prevents further etching. However, during the etching phase, the directional ions that bombard the substrate attack the passivation layer at the bottom of the trench (but not along the sides), colliding with it and sputtering it off, thus exposing the substrate to the chemical etchant. These etch/deposit steps last for several seconds and are repeated many times, resulting in a large number of very small isotropic etch steps taking place only at the bottom of the etched pits.

Reactive Ion Etching processes on the samples used to fabricate the devices described in section 5.2.3 were performed at *INtegrated PHOtonic TEchnologies Center* (INPHOTEC) in Pisa. Cylindrical holes, with 20 μm depth and different diameters (20-30-40 μm), have been etched, while the rest of the sample surface was masked using a 20 μm layer of AZ40XT photoresist. Erosion on the resist surface was not so intense, indeed a 15 μm layer was left at the end of the process.

4.1.3   Electron beam evaporation

Electron beam evaporation is a physical vapor deposition (PVD) technique used to grow different materials. The process is illustrated in Figure 4.3. The material of interest is heated thanks to the energy transferred by a focused electron beam, which causes it to start evaporating once the required vapor pressure is reached. Atoms in gas phase travel from a crucible, containing the material, to the sample surface, where they deposit to form a solid coating. The process needs to be performed in a high-vacuum chamber to let the atoms of the evaporated material follow an almost linear trajec-

tory, without undergoing collisions. This technique is strongly directional with low capacity of step coverage. These features make it an ideal process for the deposition of a material only in regions not covered by photoresist.

The machine used for this kind of deposition in *PoliFab* is an *Evatec BAK 640* evaporator, equipped with a six-pocket revolving crucible holder that allows multilayer deposition. To maintain the desired evaporation rate, strongly connected with the quality of the evaporated layer, the electron beam power needs to be controlled with a feedback system, that checks the current evaporation rate through the deposited thickness. For this purpose, a system of microbalances measures the increase in weight related to the growing film's thickness, monitoring the oscillation frequency of a quartz crystal exposed to evaporation flux; the feedback loop allows almost instantaneous adjustments, thus it is possible to regulate the speed of evaporation and the vapor tension in real time. During the fabrication of the devices presented in this work, two materials were deposited with this technique:

- Nickel (Ni), with a deposition rate of 0.1 nm/s and a power of 9% of the full scale;

- Silicon Dioxide (SiO_2), with a deposition rate of 0.3 nm/s and a power of 5% of the full scale.

For both of them, the starting pressure of the deposition was $2 \cdot 10^{-6}$ mbar.
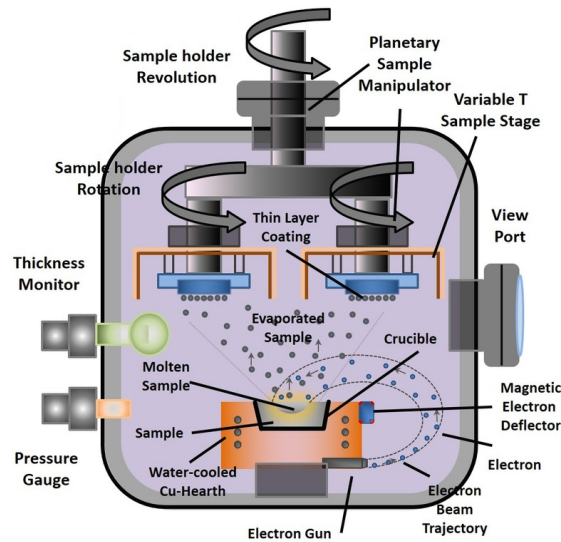
Figure 4.3: Scheme of operation of an electron beam evaporator [85].

4.1.4   Electroplating
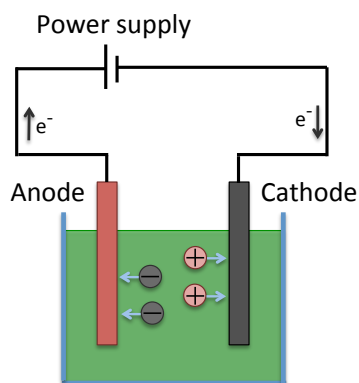
Figure 4.4: Sketch of an electrolytic cell.

Electrochemical deposition is a growth process which consists in the formation of a metallic coating onto a substrate occurring through the electrochemical reduction of metal ions from an electrolyte. The corresponding technology is often called electroplating. To perform this process an electrolytic cell is required; it is an electrochemical cell that drives a non-spontaneous redox reaction through the application of electrical energy, analogous to a galvanic cell acting in reverse.

The main components of the cell, represented in Figure 4.4, are two electrodes, a cathode (or working electrode) and an anode (or counter electrode), and an electrolyte, a solution which can conduct electricity due to the presence of positive and negative ions. To allow the current flow in the circuit, the two electrodes are connected to a power supply: the anode is connected to the positive terminal, while the cathode is connected to the negative one. When a voltage is applied across the cell, the negatively charged ions migrate to the anode and the positively charged ions migrate to the cathode. At the interface between the solution and the cathode the metal ions are reduced to metal atoms, which eventually form the deposit on the surface. The general reaction occurring at the cathode is:

$$M^{n+} + ne^- \rightarrow M \tag{4.1}$$

where n is the number of electrons involved. Metal ions can be provided by the anodic dissolution of the so called *sacrificial anodes* (made of the same metal to deposit on the cathode), due to the oxidation of metal atoms. Alternatively, they can derive from metal salts added to the electrolyte solution when non-consumable anodes are used; in this situation, ions of the metal

to be plated must be periodically replenished in the bath as they are drawn out of the solution[86].

In the typical electroplating process, current is supplied to the bath as straight DC current, but is also possible to use a pulsed current, i.e. a series of short pulses (typically with frequencies from 500 to 10000 Hz). This deposition method, called *pulse plating*, favors the initiation of grain nuclei and greatly increases the number of grains per unit area, resulting in a finer-grained deposit with improved properties with respect to conventionally plated films. Indeed, typical advantages of pulse plating include better distribution, lower porosity, higher density, greater throwing power (i.e. uniformity), improved hardness and less metal usage.

Not only the quality of the plated material, but also its thickness is a crucial parameter. According to a law formulated by Michael Faraday[86], thickness of the deposited material, current and time are related according to the following equation:

$$T = \frac{A}{nF\rho}\frac{it}{S} = \frac{A}{nF\rho}jt \qquad (4.2)$$

where T is the thickness of deposited metal, i is the current, t is the time, S is the surface area of the deposit, j is the current density, ρ is its density, A is the atomic weight, n is the valence of the dissolved metal in solution expresses in eq/mol and F is Faraday's constant (i.e. 96485.309 C/eq). Once a specific reaction is considered, $A/(nF\rho)$ has a fixed value, so thickness of the deposited material is directly proportional to current density and deposition time. In the case of nickel this constant is $3.4 \cdot 10^{-5}$ cm^3/C, considering A=58.6934 g/mol, n=2 eq/mol and ρ=8.908 g/cm^3. Thus, expressing the current density j in mA/cm^2, the resulting deposition rate T/t in μm/hour is:

$$\frac{T}{t} = 1.22j \qquad (4.3)$$

Electroplating is primarily used to cover objects to change their surface properties (such as abrasion and wear resistance, corrosion protection, lubricity, aesthetic qualities), but can be exploited also for micro- and nano-structures growth[86]. During this thesis work this deposition process was exploited to grow nickel pillars in cylindrical cavities of micrometrical dimensions, obtained inside a thick photoresist suitable for electroplating (AZ40XT) or inside a doped silicon substrate etched with Reactive Ion Etching. Thus, different cathodes were used: silicon substrates uniformly coated with 20 nm of nickel, patterned with AZ40XT to mask a portion of the surface, and highly p+ doped silicon substrates (ρ=0.005–0.025 Ωcm) with 20 μm deep

cylindrical cavities obtained with RIE. The anode was an AISI316 stainless steel slab (with typical dimension of around 3 cm x 5 cm) and the electrolyte a nickel sulfate bath. Both standard electroplating and pulse plating were performed. Details of the optimization process and main growth parameters are discussed in section 5.2.

4.1.5 Magnetron Sputtering
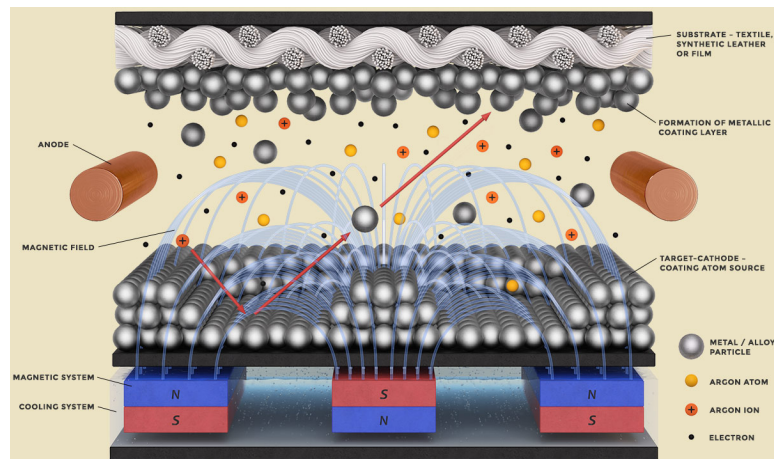
Figure 4.5: Scheme of operation of a magnetron sputtering system [87].

Sputtering is a physical vapor deposition technique used to deposit thin films on a surface, i.e. the substrate. A gaseous plasma is created and ions from this plasma are accelerated onto a a source material, called target, which is eroded by the incoming ions due to energy transfer. Neutral particles (individual atoms, clusters of atoms or molecules) are thus ejected and effuse towards the substrate, which is then coated with a thin film of the source material. To create the plasma, atoms of an inert gas (typically argon) are introduced into the high vacuum chamber and a negative bias voltage is applied to the target (cathode). Free electrons are immediately accelerated by the electric field in proximity to the target and ionize by collision the Ar atoms, leaving Ar^+ ions. Plasma is ignited thanks to this cascade process. Then, positively charged Ar^+ ions are accelerated towards the negatively biased electrode (target), striking the surface and releasing source material and more free electrons by energy transfer. To sustain a situation like this, an energy source is required. A DC bias can be used for metals, while a RF networks is required for insulators, otherwise the cathode etching would stop due to target charging; RF is also used for some metals, where it provides a better deposition with respect to DC sputtering.

In magnetron sputtering (Figure 4.5), permanent magnets are located behind the target in order to confine the free electrons in a magnetic field directly above the cathode surface. This configuration is advantageous because it prevents the free electrons from bombarding the substrate, which would cause overheating and structural damage. At the same time, the circuitous path carved by these same electrons when trapped in the magnetic field enhances their probability of ionizing neutral Ar atoms by several orders of magnitude. This increment in available ions significantly increases the rate at which target material is eroded and subsequently deposited onto the substrate. A magnetron sputtering source consists of a water cooled target holder with an embedded magnet array and appropriate grounded shielding.

During the fabrication of the devices described in section 5.4, a *Leybold-Heraeus LH Z400 MS* system was used to deposit a 30 nm Cr adesive layer and 100 nm of Au for the electrical contacts, with a base pressure below $2 \cdot 10^{-5}$ mbar. Argon flow during Cr sputtering is 70 SCCM (Standard Cubic Centimeters per Minute), which corresponds to 20 nm/min, so the sample must be left over the Cr target for 1 minute and 20 seconds. The flow for Au deposition is 50 SCCM instead, resulting in a deposition rate of 26 nm/min and a 4 minutes deposition to get the desired 100 nm. Before the sputtering deposition, the sample surface was treated with monoatomic oxygen plasma, created by exposing oxygen gas at a low pressure (typically 0.5–1.5 mbar) to high power radio-frequency, which ionizes it. This operation was performed in vacuum with a *Plasma Asher PVA Tepla 200*, kept for 8 minutes at 200 W. Thanks to this pretreatment, which should be performed right before the deposition, the surface bonds breaks and the Cr adhesion to the clean substrate improves.

4.2 Characterization

This section presents the main techniques used to characterize hemozoin crystals from a magnetic and electrical point of view.

4.2.1 Vibrating Sample Magnetometer

A Vibrating Sample Magnetometer (VSM) is an instrument able to measures magnetic properties of materials in an external magnetic field. The sample under study is introduced between the poles of an electromagnet and two pick-up coils (Figure 4.6a). First it is magnetized inside a uniform field $\mathbf{H}_0$ and then is sinusoidally vibrated (thanks to piezoelectric materials or
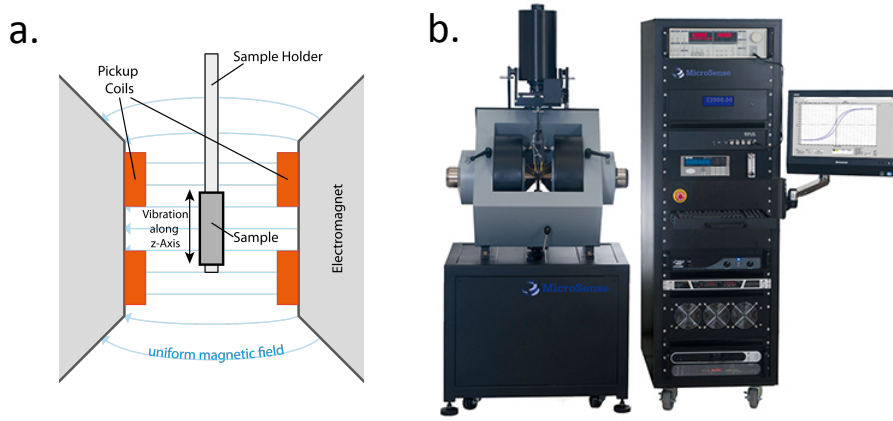
Figure 4.6: a. Sketch of the Vibrating Sample Magnetometer working principle **b.** *Microsense EZ9* Vibrating Sample Magnetometer [88].

modified audio speakers), introducing perturbations in the external magnetic field. The magnetic flux density near the sample is $\mathbf{B} = \mu_0 \left(\mathbf{H}_0 + \mathbf{M} \right)$ and its flux across the pickup coils changes in time due to the vibration. Therefore, according to Faraday's law of induction, a sinusoidal electromotive force is induced in detection coils:

$$V = -\frac{d\Phi_{\mathbf{B}}}{dt} = -\frac{d \iint_S \mathbf{B} \cdot d\mathbf{S}}{dt} \tag{4.4}$$

where $d\mathbf{S} = \mathbf{n}dS$ and $\mathbf{n}$ is the vector normal to the surface S. Considering the relation between magnetic flux density, magnetization and external magnetic field and exploiting the linearity of integral and differential operators, Eq. (4.4) can be written as:

$$V = -\iint_S \mu_0 \frac{d\mathbf{M}}{dt} \cdot d\mathbf{S} \tag{4.5}$$

where $\mathbf{H}_0$ doesn't appear because it is uniform.

If sample dimensions are small compared to the distances between the sample and the detection coils, magnetized sample can be approximated with a magnetic dipole with a uniform magnetic moment (and so magnetization). Thus, the amplitude of the electromotive force generated in the detection coils is proportional to the magnetization of the sample and, due to the scalar product with a vector normal to the surface S, only the component along the field is selected; so the magnetic moment of the sample along the field direction can be measured. The induced voltage is measured with a lock-in amplifier, using the sinusoidal vibration signal as reference.

The instrument used to measure magnetic properties of hemozoin crystals in this thesis work (see section 5.1.1) is a *Microsense EZ9* Vibrating Sample Magnetometer (Figure 4.6b), that can reach fields up to 2.25 T and measure magnetic moments down to 1 μemu. This model can measure liquid, powder, solid, bulk and thin film samples, in a temperature range from 4.2 K to 1050 K. VSM is controlled by a software, that sets a constant magnitude of the uniform magnetic field applied by the poles to the vibrating sample, measures the signal, averages and translates it into a value for the magnetic moment. This procedure is repeated for different values of the field, thus it is possible to record magnetization curves of materials.

4.2.2 Conductive Atomic Force Microscopy

Atomic force microscopy (AFM) is a very-high-resolution type of scanning probe microscopy (SPM), with lateral resolution up to fractions of a nanometer (depending on the tip dimensions and the scanning mode) and vertical resolution that can reach picometer in optimal conditions. A cantilever with a sharp tip (probe) at its end is used to scan the specimen surface such that the interaction between tip and sample, an atomic scale phenomenon, is transduced into changes of the motion of cantilever, a macro scale phenomenon. A laser beam is directed on the backside of the cantilever and reflected onto a position sensitive photodetector; thus, when the bending of the cantilever changes, the laser spot on the detector moves, allowing to convert the deflection into an electrical signal. A feedback loop keeps tip-sample interaction force or distance constant, acting on piezoelectric elements connected to the cantilever and/or the sample. AFM can operate in different modes, depending on the application. In general, possible imaging modes are divided into static (also called contact) modes and a variety of dynamic (non-contact or *tapping*) modes, where the cantilever is vibrated or oscillated at a given frequency.

Conductive atomic force microscopy (C-AFM) or current sensing atomic force microscopy (CS-AFM) is an AFM mode that allow to simultaneously measure the topography of a material (operating in contact mode) and the electric current that flows at the contact point of the tip with the sample surface when a voltage difference between them is present. It is also possible to keep the tip fixed in a certain position on the sample and study how the current changes when different voltages are applied, collecting I-V curves. The topography is acquired using the deflection signal of the cantilever, while the electric signal is measured through a current-to-voltage preamplifier. Indeed, the analogical current signal due to the imposed voltage difference needs to
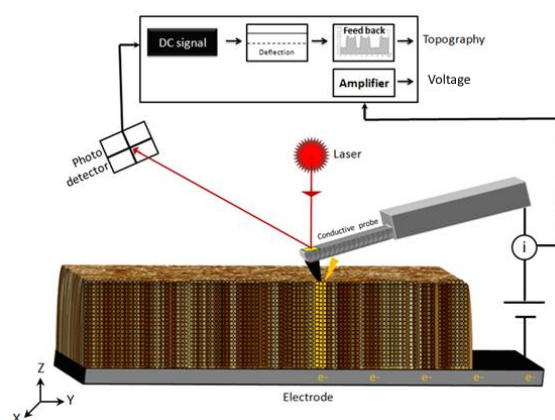
Figure 4.7: Scheme of operation of a CS-AFM.

be converted into a digital voltage that can be read by the data acquisition card of the computer. A sketch of the described CS-AFM system is represented in Figure 4.7.

To operate an AFM in the current sensing mode, the probe tip must be conductive. Usually, standard silicon nanoprobes (as those used in topographic AFM measurements) coated with thin metallic films are used. The metallic coating should be thick enough to withstand the large current densities and frictions and at the same time thin enough to not increase significantly the radius of the tip apex, maintaining its sharpness and ensuring a high lateral resolution. The lifetime of the metal-coated tips used for CS-AFM is much shorter than in any other AFM mode. Indeed, the high current densities flowing through the tip/sample nanojunction and the lateral frictions may damage the tip (metal layer melting or partial wear-off), affecting its conductive properties. In practical measurements, the sample is usually fixed on its holder using a conductive tape or paste (silver paint) and is isolated from external electrical interferences with a Faraday cage.

A *Keysight 5600LS* AFM system with *PtIr*-coated silicon tips (ANSCN-PT, AppNano-USA) was used to characterize hemozoin crystals dispersed on a gold coated substrate, as discussed in section 5.1.1.

4.3 Experimental setup for capture experiments

The ability of the devices developed in this thesis work to capture hemozoin crystals, red blood cells and superparamagnetic beads was tested in magnetic capture experiments, described in detail in section 5.3. The setup used for these tests is represented in Figure 4.8.
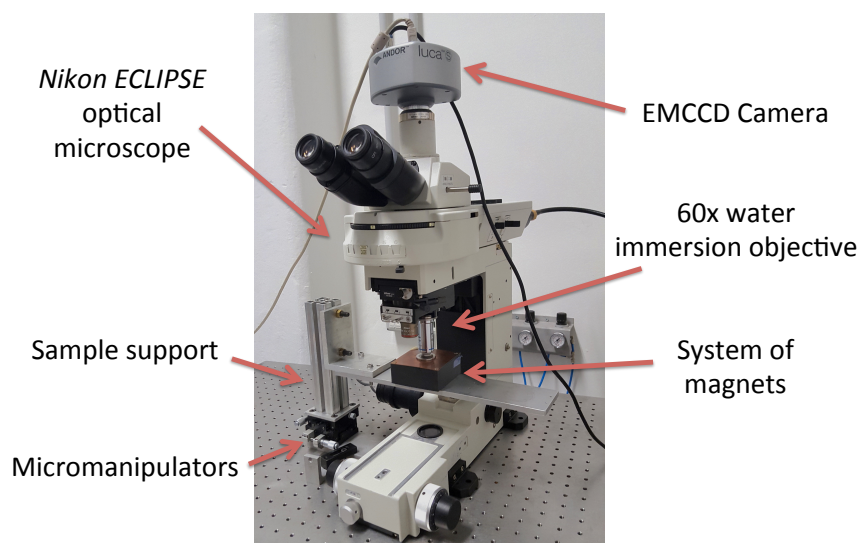
Figure 4.8: Setup used in magnetic capture experiments: a *Nikon ECLIPSE* optical microscope equipped with a 60x water immersion objective and an EMCCD camera, the designed system of magnets and a sample support endowed with micromanipulators.

The aim of these experiments was to see if, where, according to which mechanism and timing particles are attracted towards the ferromagnetic concentrators, when an external field is applied. To provide the required external magnetic field, the system of Neodymium Iron Boron ($Nd_2Fe_{14}B$) permanent magnets described in section 3.2.2 was used; it is located underneath the Petri dish containing the chip and the solution with the particles to analyze. All the Neodymium Iron Boron magnets are inserted in a support made by 3D printing of PLA (polylactic acid); to keep them in position a thin copper sheet is used, patterned to allow a proper alignment of the Petri dish with respect to the system of permanent magnets.

The experiments were monitored using a *Nikon ECLIPSE* optical microscope, equipped with a 60x water immersion objective and an EMCCD camera. Two additional filters are installed in the light pathway of this microscope: FITC (Fluorescine IsoThio-Cyanate), with an excitation bandpass of 465–495 nm (blue spectral region) and an absorption bandpass in the green spectral region from 515 nm to 555 nm, and TRITC (Tetramethyl Rhodamine Iso-Thiocyanate), that has an excitation bandpass of 525–540 nm (green spectral region) and absorbs in the red spectral region from 605 nm to 655 nm. Fluorescence has been employed in capture experiments to identify the position of magnetic nanoparticles and red blood cells, both functionalized with TRITC markers.

4.4 Red Blood Cells treatment protocol

In 1936 Pauling et al.[17] discovered that oxyhemoglobin (oxyHb) is diamagnetic, while deoxygenated hemoglobin (deoxyHb) and methemoglobin (metHb, the oxidized form of hemoglobin) are paramagnetic. Exposing RBCs to particular oxidizing drugs leads to an oxidation of their hemoglobin into metHb[21,70,71]; indeed, the ferrous ions (Fe^{2+}) are converted to the ferric (Fe^{3+}) state. As discussed in section section 2.2.2, the hemozoin heme electron configuration corresponds to the one present in metHb[9]. Thus, the conversion from diamagnetic oxyHb to paramagnetic metHb in treated RBCs (t-RBCs) can be regarded in the same way as the one that occurs in infected RBCs (i-RBCs) due to malaria parasite[21]. To obtain RBCs with magnetic properties similar to infected ones, a treatment with a solution of $NaNO_2$ was performed on bovine blood, according to the protocol described below. Blood samples were provided and treated by Annalisa Dimasi, Marco Piola and Prof. Gianfranco B. Fiore from *µBS Lab* of Politecnico di Milano.
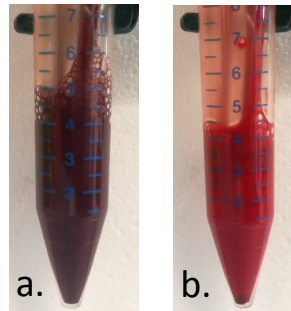
Figure 4.9: Solution of treated (**a.**) and untreated (**b.**) RBCs suspended in PBS.

Bovine blood, mixed with 5000 μl/ml of sodium heparin as an anticoagulant, is centrifuged such that red blood cells (RBCs) are separated from plasma and other blood components. Once insulated, they are resuspended in PBS (phosphate buffered saline) to reach a hematocrit around 45%. This solution must be conserved at 4°C; if it is not used just after the resuspension, a washing treatment to remove hemolized RBCs is required. After a 20 minutes oxygenation with a peristaltic pump, the suspension is divided in two samples: a negative control (untreated RBCs, ut-RBCs) and a positive one (treated RBCs, t-RBCs). The latter is treated with a 30 mg/ml $NaNO_2$ solution, such that a $NaNO_2$ concentration of 840 μg/ml ($NaNO_2$ mass/RBC suspension volume) is obtained. The suspension is stirred for 30 minutes and needs to be used within the day, because the treatment effectiveness decreases in time[71]. The two samples exhibit very different colors, as showed

in Figure 4.9: the untreated sample has the typical bright red color of oxygenated blood, while the treated sample is dark red since metHb cannot carry oxygen. Note that metHb forms in low level also in vivo due to natural oxidative mechanisms[89,90], thus a low but not null percentage of metHb can be present also in the untreated sample. Then, both RBCs solutions were stained with a fluorescent marker *CellTracker^{TM} Red CMTPX Dye* (Thermo Fisher Scientific-USA), with maxima of excitation and emission at 577 nm and 602 nm, respectively. They were used to perform magnetic capture experiments, as described in section 5.3.3.

Chapter 5

Experimental results

The main experimental results obtained during this thesis work are presented in this chapter. First, a characterization of magnetic and electric properties of hemozoin crystals is reported. Subsequently, the fabrication process for the chip realization is described, with a focus on the optimization of nickel electroplating. Then, an application of the fabricated devices in magnetic capture experiments, performed with magnetic beads, hemozoin crystals and bovine RBCs treated to model infected RBCs, is shown. Finally, for the sake of completeness, the main results of impedance measurements performed by Prof. Marco Sampietro's group are presented.

5.1 Characterization of hemozoin crystals

Magnetic and electric properties of hemozoin crystals were characterized to determine the real parameters to be used for the design of the diagnostic chips. Hemozoin has been considered paramagnetic[6,16,18–20], but recently Inyushin et al.[64] proposed that it has a superparamagnetic behavior instead. Since hemozoin magnetic response to an applied $\mathbf{H}$ field, i.e. its magnetic susceptibility χ, is a crucial parameter in the design of the diagnostic test, we performed independent VSM measurement on the same synthetic crystal used by Inyushin and coworkers. Furthermore, no information about hemozoin conductivity can be found in literature, thus an electrical characterization was fundamental, since this is a central property in impedance detection. A low frequency (DC) characterization was performed with CS-AFM, while high frequency properties were analyzed in impedance measurements, as described in section 5.4.
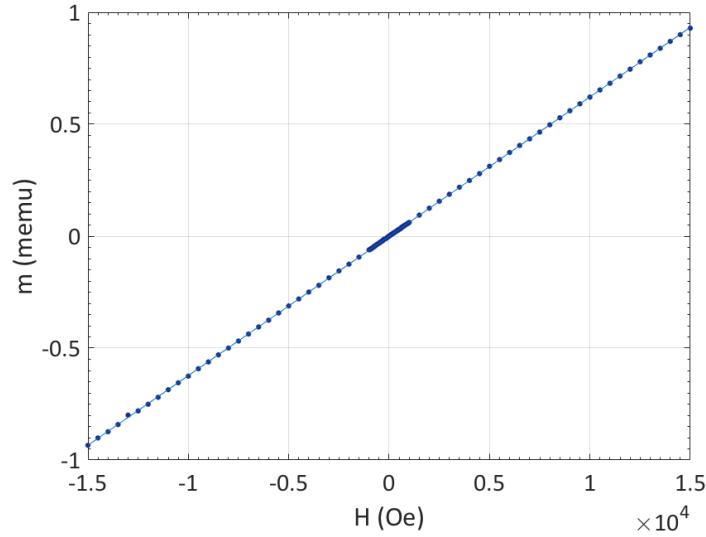
Figure 5.1: Magnetization curve of hemozoin crystals measured with a *Microsense EZ9* Vibrating Sample Magnetometer. m represents the total magnetic moment of the sample.

5.1.1 Magnetic characterization

Volume magnetic susceptibility χ of synthetic hemozoin crystals (InvivoGen-USA) was evaluated measuring their magnetization curve (i.e. $\mathbf{m}$ vs $\mathbf{H}$) with a Vibrating Sample Magnetometer (VSM). Hemozoin, provided as a black powder, was inserted in a plastic cuvette, fixed to a quartz stick connected to the oscillating system. A (3.3 ± 0.2) mg hemozoin sample was tested, varying the external field $\mathbf{H}$ between -1.5·10^4 Oe and 1.5·10^4 Oe. The average net signal resulting from three measurements, after the subtraction of the background signal arising from the sample support (i.e. cuvette, stick and tape to fix them), is shown in Figure 5.1. Blue points are the measured data, denser close to the origin to investigate the behavior in a more precise way, while the interpolating curve is a straight line with angular coefficient 6.2234·10^{-5} memu/Oe.

The straight line with positive angular coefficient and passing through the origin indicates a paramagnetic behavior; saturation is not achieved in the analyzed $\mathbf{H}$ field interval. Starting from the relation $\mathbf{M} = \chi\mathbf{H}$ and considering that magnetization $\mathbf{M}$ is the magnetic moment $\mathbf{m}$ per unit volume, the volume magnetic susceptibility χ can be calculated as:

$$\chi = \frac{\Delta m}{\Delta H \, V_{HC}} \tag{5.1}$$

where $\Delta m / \Delta H$ is the angular coefficient of the straight line interpolating the measured point and $V_{HC} = 2.21 \cdot 10^{-3}$ cm^3 is the analyzed hemozoin volume. Considering the proper conversion factors to express all the measured quantity in SI units, the obtained volumetric susceptibility for hemozoin crystals is $(3.5 \pm 0.2) \cdot 10^{-4}$.

This value is very close to the one calculated by Coronado et al.[6], starting from experimental results acquired by Hackett et al.[16], i.e. $\chi = 3.20 \cdot 10^{-4}$. Conversely, measuring synthetic crystals produced by the same company we used as a supplier, Inyushin et al.[64] obtained a much larger value, i.e. $\chi = 3845$. Thus, due to the high value of susceptibility, Inyushin and coworkers suggested that hemozoin crystals have a superparamagnetic behavior. However, our independent VSM measurements do not confirm this conclusion. Moreover, magnetic capture experiments of superparamagnetic beads ($\chi \sim 1$) and hemozoin crystals with similar dimensions (i.e. 200–300 nm) were performed, as discussed in detail in section 5.3. While for beads an almost instantaneous capture was observed, the dynamics of hemozoin crystals was much slower. Therefore, according to our results, it is unlikely that hemozoin may have a susceptibility more than one thousand times higher than magnetic beads. Additional measurements to check our results on a different batch of hemozoin crystals have been planned, but these data are not available at the time of writing of this thesis.

5.1.2 Electrical characterization

Hemozoin DC conductivity was measured by Current Sensing Atomic Force Microscopy (CS-AFM). As described in section 4.2.2, with CS-AFM allows to acquire both topographic images of the sample and I-V curves in specific points. Topography was used to identify the position of hemozoin crystals, while their conductivity was measured thanks to I-V curves. To spread the particles to analyze on a proper support, a few μl of a solution of hemozoin crystals in deionized water were poured on a gold-coated silicon substrate, which was left on a hot plate until complete water evaporation. Measurements of I-V curves were performed on several points of the surface, both on the gold substrate and on hemozoin crystals, applying to the $PtIr$-coated Si tip a voltage bias up to $\pm$ 10 V, by performing a sweep from 0 V to 10 V, then to -10 V and finally again to 10 V. During tests on hemozoin crystals, a current lower than a few pA was recorded, thus indicating an insulating behavior. Conversely, on the Au substrate, as soon as the applied tension reached a few mV, the current flowing between the tip and the conductive substrate saturated to 10 nA (the maximum readable value). I-V curves

on gold were taken before and after measurements on hemozoin crystals, to check the tip status, i.e. if it was still conductive or not due to a partial removal of the metallic coating (i.e. wear off). I-V curves recorded on the gold layer and a hemozoin crystal are showed in Figure 5.2.
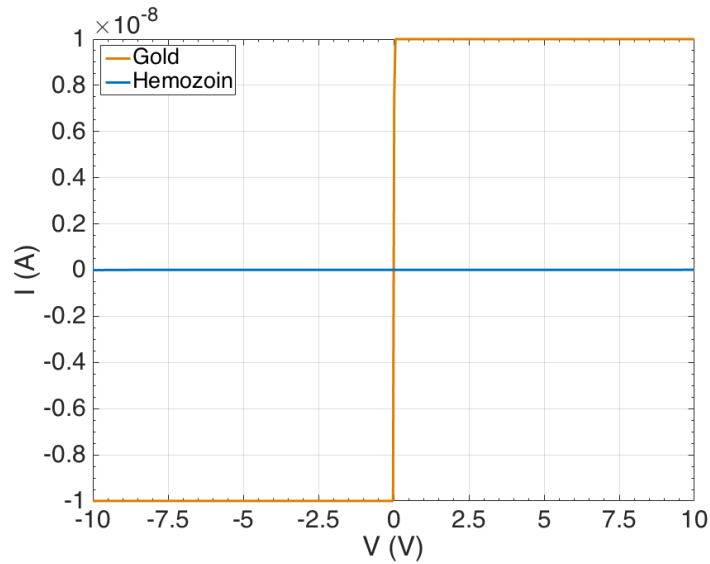
Figure 5.2: I-V curves of gold and hemozoin crystals.

5.2   Optimization of the electrodeposition process

The purpose of the detection system developed in the TID MEKII project is to attract hemozoin crystals and infected red blood cells exploiting their paramagnetic properties, concentrate them in specific areas and quantify their number through an impedance detection. To achieve this result, a system made of an array of nickel concentrators with gold electrodes above them has been designed, taking into account the results of the simulations described in section 3.2. Then, a suitable fabrication process has been implemented for the two components, i.e. the magnetic pillars and the electrodes, while their integration on the real chip is still under development. A partial integration of the two parts for preliminary experiment of capture and detection is presented in section 5.4. As far as device fabrication is concerned, the focus in this thesis work has been mainly on the magnetic layer, whose central process is the growth of 20 μm-height nickel pillars via electroplating. The optimization of this technique is described in detail in the following sections.

5.2.1 General parameters

Nickel electroplating is typically used to deposit thin films on macroscopic metal objects to provide corrosion and mechanical resistance or for decorative purposes. However, this technique is applied also in microfabrication, mainly for coatings depositions[91–98]; there are just a few examples of electroplating for the growth of structures inside pattens[99–103], usually defined by a photoresist mask. In case of non-metallic substrates (e.g. silicon wafers), a seed layer with a thickness of few nm is typically evaporated before the electrochemical process, to provide a uniform current to the sample and improve the adhesion of electrodeposited nickel, usually not optimal on silicon. Although electrodeposition is a relatively low cost and in principle simple technique, it has many parameters that need to be controlled. Indeed, the deposition rate and the quality of the plated material are strongly dependent not only on the composition of the plating bath and the conditions used for the deposition (i.e. temperature, stirring, pH, anode), but also on the current provided to the circuit (absolute value and type, i.e. DC or pulsed). The choice of these parameters is crucial for the growth of microstructures like the ones designed for the magnetic layer of the detection device. During my thesis I developed from scratch the process of nickel electroplating within micrometric patterned cavities in silicon wafers. This is the first example of growth by electroplating performed in the *Polifab* cleanroom. The magnetic attraction capabilities of the deposited *Ni* microstructures have been proved in capture experiments, as described in section 5.3.

A *Watts bath* (ASTRO ROTO PLUS, Tecnochimica-Italy), containing nickel sulfate (180-200 g/l) together with nickel chloride (70-90 g/l) and boric acid (40-45 g/l), has been used for *Ni* electroplating. The solution was agitated with a magnetic stirrer and kept at a temperature around 55°C during the process. The anode mainly used for the process was an AISI316 stainless steel slab, with dimensions around 3 cm x 5 cm. Some tests were performed using a grid of MMO (mixed metal oxides), but its discontinuous shape strongly affected the uniformity of the deposited material inside the pattern. Two different kinds of cathodes were used, as discussed afterwards, with dimensions around 2.5 cm x 3.5 cm. They were bigger than the final chip area (1 cm x 1 cm) because an electrical contact between the sample and the circuit needs to be established (through silver paste and a metallic clamp); in addition, sample dimensions must be sufficient to allow a proper immersion in the plating bath. Moreover, kapton tape was used to cover the edges of the sample, to prevent unwanted *Ni* deposition in these areas, originating from tip effect.

Electrodepositions with DC current were performed using a current generator, monitoring the constant applied current with an amperometer. Moreover, the corresponding voltage drop, measured by the generator itself, was kept under observation because a too intense increase of its value would damage both the cathode and the plating solution. The applied current was ≈1 mA and the measured voltage around 1 V, so the resistance of the plating bath R_{pl} was ≈1 kΩ. Conversely, for pulse plating a voltage generator was used. In order to provide a constant current to the circuit, despite the variations of the plating bath resistance, a 8.2 kΩ resistor was connected in series with the electrochemical cell. In this configuration the current was mainly determined by the external resistor and only slightly influenced by the small variations of R_{pl}. Moreover, a 0.1 μF was connected in parallel to the 8.2 kΩ resistor, to eliminate the effect of the capacitive component of the solution. Since the total resistance was in the order of 10 kΩ and the required current ≈1 mA, 10 V were applied for a 400 ms pulse, followed by 100 ms at 0 V. An oscilloscope was used to monitor the current flowing in the circuit. It was connected in series with the other elements of the circuit and a 50 Ω input impedance was set, such that it did not modify the current flow in a relevant way. A scheme of the total electrical circuit used for deposition with pulsed current is shown in Figure 5.3.
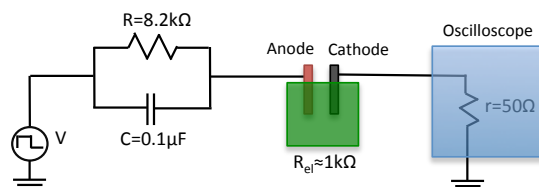
Figure 5.3: Scheme of the electrical circuit used to provide current during pulsed depositions.

5.2.2 Initial process

At first, electroplating has been performed with DC current on a silicon substrate with a continuos 20 nm nickel layer evaporated on the whole sample. To properly define the areas of pillar growth, a 20 μm layer of AZ40XT resist was patterned via photolithography, creating an array of cylindrical holes. Nickel was electrodeposited only inside these cavities, since the insulating resist layer prevented its growth in different areas. Then, the photoresist was removed in acetone, leaving nickel pillars above the uniform Ni seed layer.
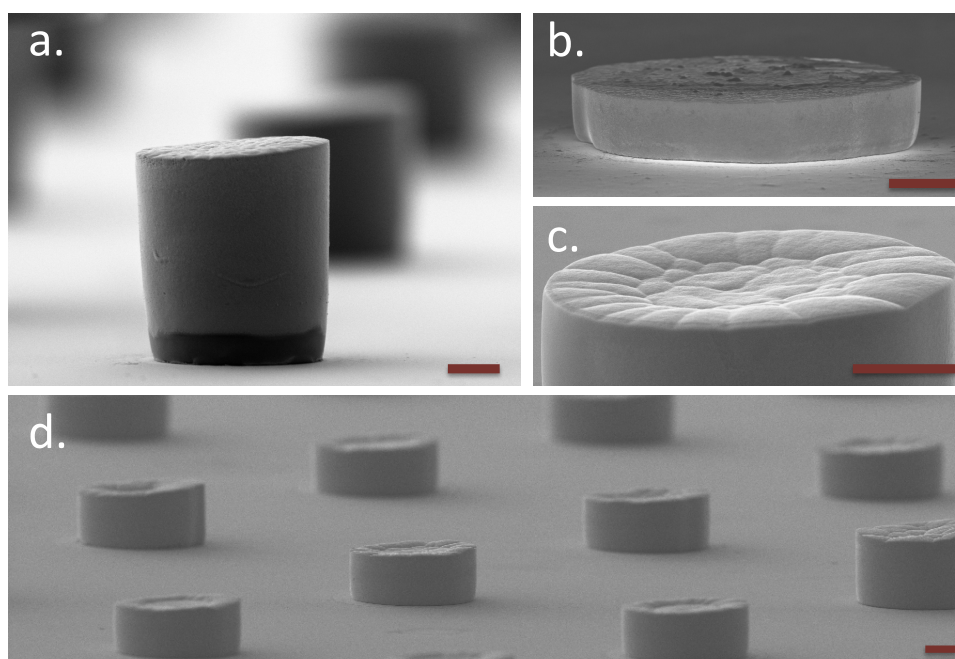
Figure 5.4: SEM images of nickel pillars with different dimensions. **a.** Cylinder with d=20 μm and h≈20 μm. **b.** Cylinder with d=20 μm and h≈4 μm. **c.** Detail of the upper surface of a 20 μm-diameter cylinder. **d.** Array of cylinders with d=20 μm and h≈8 μm, arranged in a hexagonal close-packed structure with a 80 μm spacing. The scale bars are 5 μm.

Since depositions on samples with different patterns have been performed, the relevant parameter used to compare them is not the current but the current density j, i.e. the current provided per unit surface. The typical DC currents we used (from 0.5 to about 1.5 mA) correspond to densities between 10 and 20 mA/cm^2. According to Eq. (4.3) presented in section 4.1.4, the deposition rate T/t is proportional to the current density j, with a proportionality constant of 1.22, considering j in mA/cm^2 and T/t in μm/hour. Thus, for the deposition conditions we used the rate should be around 12–24 μm per hour. Results slightly lower with respect to these values (i.e. ≈10 μm/h with $j = 10$ mA/cm^2) were obtained for deposition on unpatterned samples, while an accurate calibration for patterned samples was not achieved due to non-uniformity of the deposited cylinders. Indeed, the obtained wide distribution of the pillars height, due to a preferential growth in some regions, made impossible to properly determine the deposited thickness. In some cases the electroplated pillars became even higher than the 20 μm-thick resist, thus creating preferential spots for a more rapid further growth outside the cavities.

In Figure 5.4 some examples of microstructures fabricated with Ni electroplating are represented. As it can be noticed, both in the overview (Figure 5.4d) and in a zoom of the upper surface (Figure 5.4c), the deposited material is not perfectly uniform and planar, with some preferential growth closer to the edges. Apart from the unavoidable electrostatic edge effects, most of the height variability can be attributed to variability in the quality of the Ni seed layer surface prior to the electroplating process. Although AZ40XT is a photoresist suitable for electroplating[83], many problems related to sample surface cleaning arise, before and after the deposition. Indeed, the presence of the resist mask prevents the use of typical organic solvents (i.e. acetone and isopropyl alcohol) to remove impurities from the surface before the deposition. Additionally, the photoresist is affected by temperature variations when the sample is inserted in and extracted from the electrodeposition bath. These thermal gradients result in the creation of cracks in the resist mask, that prevent redeposition on the same sample (required when the deposited thickness is not enough); moreover, they make resist removal harder after the deposition.

5.2.3 Improved process

Using a Ni seed layer and a photoresist mask we were able to fabricate micrometric nickel pillars, tested in preliminary magnetic capture experiments after removal of the photoresist mask. However, this configuration cannot be applied in the final device because a planar surface is needed to fabricate the electrical layer (i.e. electrodes and electrical connections) above the magnetic one. Since a 20 μm planarisation is really hard to achieve, a different strategy was adopted. Instead of growing pillars above the surface in cavities defined with a photoresist, the Si substrate was etched to create 20 μm-deep cylindrical cavities, inside which Ni can be grown by electroplating. Thus, filling the cavities with nickel, a planar surface can be obtained.

The main steps of this new fabrication process are represented in Figure 5.5. Firstly a pattern is defined through photolithography with AZ40XT photoresist. Then the regions not covered by the resist are etched away by Reactive Ion Etching, that creates cylindrical cavities with a 20 μm depth. Without removing the photoresist, 15 nm of nickel are evaporated on the whole sample, but only the layer on the bottom of the cavities is left after resist lift-off. Subsequently, 20 μm of nichel are grown by electroplating inside the cavities, thus filling them up to the sample surface level. Finally, 100 nm of SiO_2 are evaporated as insulating layer.
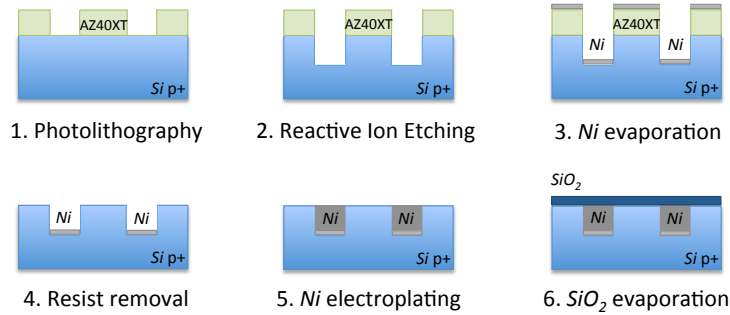
Figure 5.5: Sketch of the main fabrication step of the magnetic layer.

To allow a current flow across the whole sample without the need of a continuous metallic seed layer, a different substrate was used, i.e. highly p+ doped silicon with a resistivity $\rho = 0.005 - -0.025$ Ωcm. A thin nickel seed layer was evaporated on the bottom of the cavities before electroplating because the adhesion of electrodeposited Ni on Si was poor. Due to the high directionality of RIE and e-beam evaporation, this thin layer was not deposited on the lateral surfaces of the holes but only on their bases, thus resulting in an improved adhesion of the electroplated material and in the promotion of a growth starting from the bottom of the cavity. Furthermore, in this new configuration the photoresist can be removed after the seed layer deposition, as its role of insulating mask during deposition is no more needed. Indeed, the difference between the top Si surface and the bottom of the cavities covered by the Ni seed layer is enough to promote the selective growth in the cavities. Being able not to use the resist is a great advantage as far as sample cleaning is concerned.

As a consequence of the very directional etching performed with RIE, sharp edges were created on the substrate surface in correspondence of the deep cavities. The tip effect arising from these areas, together with the difficult penetration of the ions in the solution inside the holes, led to the formation of toroidal structures around the upper circumference of the cavities, as shown in Figure 5.6a. This problem was solved by using pulsed current instead of DC current. In samples deposited using current pulses, like the one illustrated in Figure 5.6b, initial nucleation occurred on the bottom of the holes and the further growth allowed to fill the cavities in a relatively uniform way. Additionally, to make the surface more hydrophilic and favor the penetration of the solution within the cavities, samples were treated with ethyl alcohol just before the deposition. Although it has been extremely reduced, an influence due the edge effect is still present; indeed, some pillars
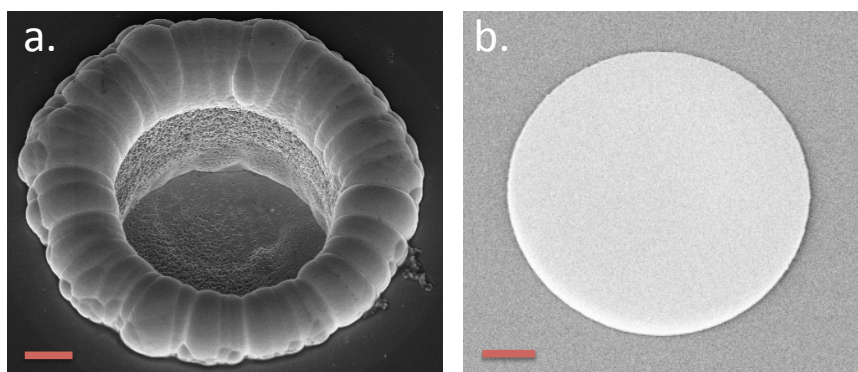
Figure 5.6: Top-view SEM images of *Ni* pillars deposited with DC (**a.**) and pulsed current (**b.**). Diameters are 30 μm and 25 μm, respectively, and both pillars grew in 20 μm-depth cavities. The scale bars are 5 μm.

grow preferentially closer to the lateral surface of the cavities, thus creating sometimes a slight depression in the central part of the cylinder.

As previously mentioned, current was applied with 400 ms pulses, followed by 100 ms intervals where no tension was provided by the generator. A proper correlation between the deposition time and the electroplated thickness has not been established so far, due to uniformity and repeatability problems. Nevertheless, pulsed current allowed to obtain a growth proceeding from top to bottom, as clearly visible in Figure 5.7, where a cavity inside the substrate, partially filled with electroplated nickel, is represented. Next step will be the control of the deposition conditions in order to improve the reproducibility and tune the deposition time to obtain the complete filling of the cavities over the whole chip. Indeed, a good surface planarity is needed to fabricate the electrodes on top of the pillars.

Electroplating was performed on arrays of circles with different diameters (from 20 to 40 μm) and spacings (from 60 to 160 μm). As expected, considering the same parameters and deposition conditions, better results were obtained for cavities with a larger diameter and thus a reduced aspect ratio. A portion of the three patterns used to test the influence of geometry on magnetic capture efficiency is shown in Figure 5.8. In the first pattern (Figure 5.8a) the cavities are not completely filled, while in the other two (Figure 5.8b,c) a slightly excessive growth led to the formation of a portion of *Ni* structure also outside the cavities. Indeed, the effective diameters of the deposited pillars on the sample surface is higher that the dimensions of the filled cavities. Note that, for all these samples, a hexagonal close packed (HCP) structure was chosen to maximize packing and improve capture efficiency.
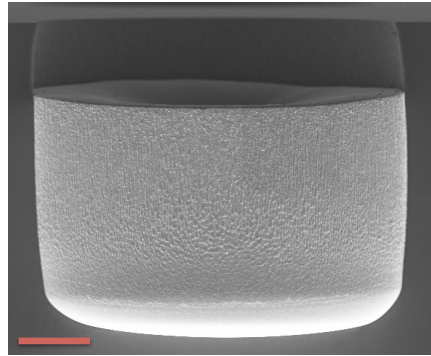
Figure 5.7: Cross-section SEM image of a *Ni* pillar grown inside a 20 μm-deep cavity with a 25 μm diameter. The scale bar is 5 μm.

To summarize, the best results obtained so far have been achieved by adopting the following procedures:

- Use a pulsed current;

- Promote the growth from the bottom of the cavities with a metallic seed layer;

- Cover the edges of the sample with kapton tape to avoid unwanted deposition of *Ni* outside the pattern;

- Do not use a photoresist mask during electroplating;

- Increase surface wettability with a treatment in ethyl alcohol just before the deposition, to favor the penetration of the ions in the bath within the cavities;

- Use silver paste to establish a more stable contact between the sample (cathode) and the rest of the electric circuit.

Despite the progresses reached so far, electroplating process has not been fully optimized yet. The major problems are related to the lack of complete repeatability in different depositions performed with the same nominal conditions and to the non-uniformity of the nickel pillars within the same samples. Indeed, good quality pillars have been fabricated, but not always on the whole pattern. Furthermore, efforts are still needed to obtain a planar surface to allow electrodes fabrication. Nevertheless, nickel pillars fabricated so far have shown good magnetic attraction capabilities, as described in the next section, thus allowing to demonstrate the feasibility of the diagnostic test proposed within the TID MEKII project.
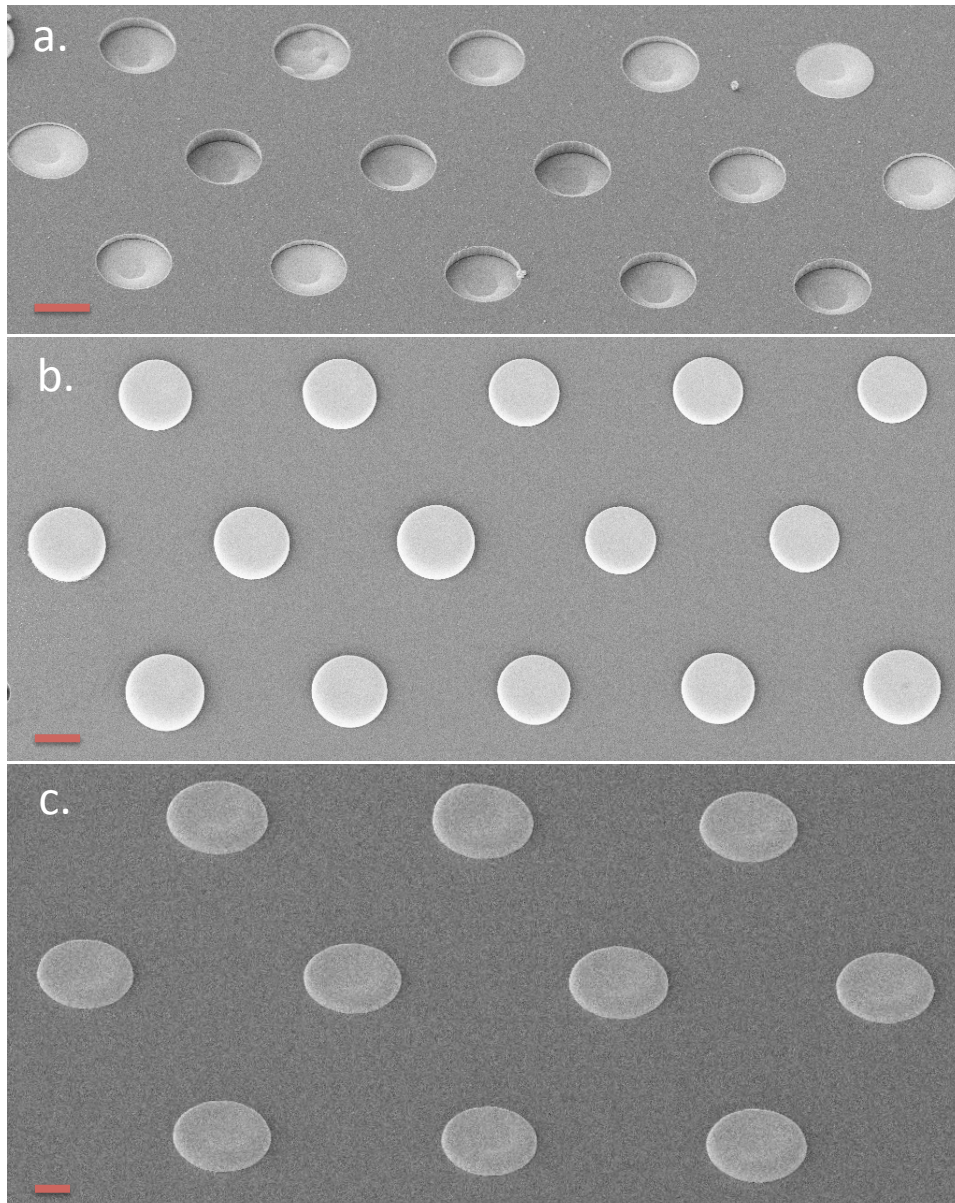
Figure 5.8: SEM images of the *Ni* pillars arrays used in capture experiments. **a.** Tilted view of a HCP array with d=25 μm and s=60 μm. **b.** Top view of a HCP array with d=30 μm and s=80 μm. **c.** Tilted view of a HCP array with d=45 μm and s=160 μm. The scale bars are 20 μm.

5.3 Magnetic capture experiments

The designed detection device should operate in reversed configuration, i.e. with magnetic force opposing gravity. Indeed, in this situation i-RBCs and hemozoin crystals are attracted upwards towards the electrodes, while non-infected erythrocytes and the other blood cells (i.e. white blood cells and platelets) sediment, as discussed in section 1.2.2. So far, preliminary experiments have been carried out in direct configuration (i.e. with magnetic force directed as gravity) to test the capture efficiency of the fabricated nickel concentrators and the magnetic properties of hemozoin crystals and RBCs treated to assume a behavior similar to the infected ones. Thanks to these experiments it was possible not only to test magnetic objects fabricated by electroplating, but also to verify the effectiveness of the treatment on RBCs and to acquire additional information on the magnetic properties of hemozoin crystals. Surely an important step in the next phase of the TID MEKII project will be to repeat the tests in reversed configuration, but the results acquired so far have been extremely useful.

Nickel concentrators fabricated according to the processes described in the previous section proved their capability to attract and concentrate magnetic particles in tests carried out on superparamagnetic beads, hemozoin crystals and red blood cells. During the experiments, each sample with electroplated magnetic concentrators was placed in a Petri dish above (i.e. in direct configuration) the permanent magnets system described in section 3.2.2, able to provide a $\sim 2\cdot 10^{14}$ A^2/m^3 gradient in the region around the sample. After pouring a solution with magnetic particles on the sample surface, capture mechanism was monitored with a *Nikon ECLIPSE* optical microscope, equipped with a 60x water immersion objective and a TRITC filter. The main results of these experiments, performed on the three samples represented in Figure 5.8, will be presented in the following sections.

5.3.1 Fluorescent superparamagnetic beads

Magnetic properties of the nickel pillars were first tested in capture experiments with magnetic nanoparticles (*nanomag-CLD-redF*, Micromod), even though they are not involved in malaria diagnosis. Indeed, as mentioned in section 3.2.4, the magnetic attraction system developed for malaria detection may be applied also to trapping or separation of magnetic particles for other purposes. Magnetic beads were considered for the experiments because they are typically used as label for other non-magnetic particles. Furthermore, they constitute well known and characterized magnetic particles, ideal for

assessing the capture capability of fabricated chips.

A solution of magnetic beads dispersed in PBS with a 5 μg/ml concentration was used. These particles are functionalized with a fluorescent marker in the far-red, thus they can be observed both in bright field and with the fluorescence signal acquired thanks to a TRITC filter. Since they have a high susceptibility ($\chi \approx 1$), magnetic force towards the Ni pillars (see Eq. (2.14)) is really intense, while the contribution of the forces acting in the opposite direction (i.e. drag and buoyancy forces) is weak due to the reduced dimensions of the particles (i.e. 300 nm). The resulting capture was basically instantaneous, thus in Figure 5.9 we present images of the samples before (t_0) and right after (t_f) the pouring of the solution of magnetic beads. The control tests were performed in the same way in absence of the external magnet.

All tested patterns had HCP structures, but pillars with different diameters and spacings (i.e. center-to-center distance) were considered, to study the influence of these geometrical parameters on capture efficiency. Each column in Figure 5.9 represents a sample with a different pattern: 25 μm-diameter pillars with 60 μm spacing in the left column (Figure 5.9a), 30 μm-diameter pillars with 80 μm spacing in the central one (Figure 5.9b) and 45 μm-diameter pillars with 160 μm spacing in the column on the right (Figure 5.9c). The number of pillars in the microscope field of view depends mainly on the spacing between the elements of the arrays. Therefore, many concentrators can be seen in Figure 5.9a and Figure 5.9b, while a single one is present in Figure 5.9c because its distance with the nearest neighbors is 160 μm.

Beads position can be identified thanks to the red fluorescence signal they emit when properly excited. In presence of the external magnet, a complete capture of the beads is obtained for all three pattern, due to the intense magnetic force particles are subjected to. Indeed, in Figure 5.9a-c(ii) there are no beads on the sample surface outside the patterns. Conversely, in absence of the external magnets (i.e. for the control samples), there is no magnetic force able to attract the beads, thus they can reach the sample surface only through sedimentation. This phenomenon is slow due to beads reduced diameter (i.e. 300 nm), so there are no particles visible in Figure 5.9a(iii),b(iii) and only a few of them floating in solution in Figure 5.9c(iii). However, pillars irregularities cause some unexpected fluorescence signals, mainly in correspondence of the external edges (Figure 5.9b) and the slight depressions in the central part of the cylinder upper base (Figure 5.9a,c). In particular, around the pillars in the control sample in Figure 5.9b(iii) a fluorescence signal not visible in the sample without beads (Figure 5.9b(i)) is present. It may
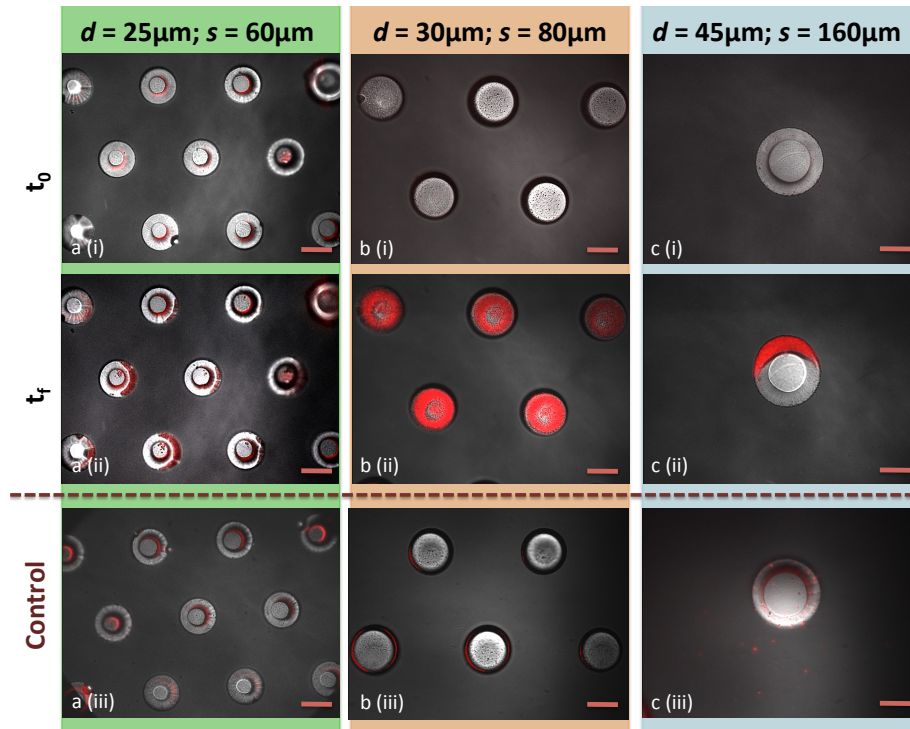
Figure 5.9: Results of the magnetic capture experiments performed on fluorescent magnetic beads, obtained as a superposition of bright field and TRITC images. Each column corresponds to a sample with a different pattern, while the first two rows indicate the observation time: before (t_0) and right after (t_f) the pouring of the beads solution. The last row presents the control samples after the pouring of the beads solution. Scale bars are 20 μm.

be due to pillars irregularities, as previously discussed, or a weak attraction may result from the remanence magnetization present in Ni concentrators after the removal of the external magnet.

While for the pattern in Figure 5.9b(ii) the particles are almost uniformly captured on the whole pillar (mainly on the edges), for the other two (i.e. Figure 5.9a(ii),c(ii)) they are localized in specific regions close to the edges. This asymmetry may result from non uniformities of the pillar surface or of the local magnetic field gradient. Additionally, many particles accumulate on top of the capture areas, forming three-dimensional structures. Thus, it is not possible to have a clear estimate of the amount of beads captured on each pillar considering just the area. It is not possible to count them neither, since single particles cannot be differentiated when gathered. Nevertheless, the almost total absence of beads on the sample surface outside the pillars is a clear indication of the capture efficiency of the tested structures.

5.3.2 Hemozoin crystals

Hemozoin crystals are among the particles that the designed malaria detection device aims to capture. Therefore, test the developed magnetic attraction system on these objects is fundamental. Magnetic properties of the synthetic hemozoin crystals (InvivoGen-USA) used in capture experiments have been characterized via VSM measurements, as described in section 5.1.1. The obtained susceptibility value is $3.5 \cdot 10^{-4}$, i.e. four orders of magnitudes lower than the superparamagnetic beads considered in the previous section. Since the dimensions of these two particles (i.e. hemozoin crystals and beads) are similar, sedimentation and drag contribution are almost the same, while the magnetic force is around 10^4 times higher for magnetic beads due to the larger χ. Thus, since magnetic force is much less intense, attraction of hemozoin crystals is not instantaneous like for beads, longer times are required. Capture dynamics was monitored for around 60 minutes from the pouring of the solution of hemozoin crystals in PBS (concentration $\sim 100 \mu g/ml$). Images of the samples at the beginning of the observation and after 30 and 60 minutes are shown in Figure 5.10. As for magnetic beads, control tests were performed in the same conditions but in absence of the system of permanent magnets; observation time was reduced to 30 minutes because the behavior of the tested particles was clear. As in the previous section, each column in Figure 5.10 represents a sample with a different pattern: 25 μm-diameter pillars with 60 μm spacing in the left column (Figure 5.10a), 30 μm-diameter pillars with 80 μm spacing in the central one (Figure 5.10b) and 45 μm-diameter pillars with 160 μm spacing in the column on the right (Figure 5.10c).

Magnetic concentrators result to be good attractors also for hemozoin crystals, even though with a slower dynamic with respect to superparamagnetic particles. Indeed, after 60 minutes all the particles are captured on the Ni pillars in the 60 μm-spaced array (Figure 5.10a(iii)) and an almost complete capture is achieved also for the other patterns (Figure 5.10b(iii),c(iii)). Furthermore, even after 30 minutes (Figure 5.10a-c(ii)) there are nearly no hemozoin crystals on the sample surface outside the concentrators. Thus, the vast majority of the particles that reach the proximity of the sample surface is captured and, as the time goes on, more hemozoin crystals are in this condition. Indeed, the time required to reach this situation is longer for more distant particles. However, note that the solution volume needed to observe the system with the immersion objective ($\sim 300 \mu l$) and so the thickness of the droplet are much larger than the ones we planned to use in the designed malaria detection device. Therefore, in the final device all
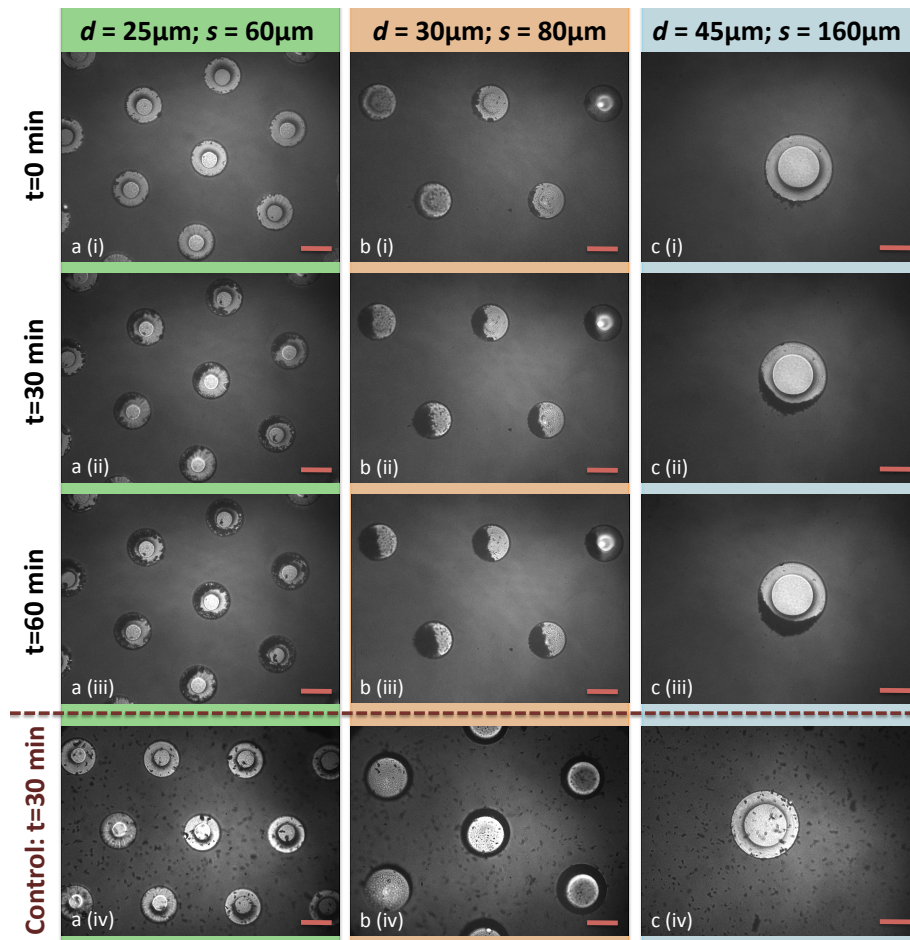
Figure 5.10: Results of the magnetic capture experiments performed on hemozoin crystals. Each column corresponds to a sample with a different pattern, while the first three rows indicate the observation time, i.e.0-30-60 minutes from the beginning of the experiment monitoring. The last row presents the control samples after 30 minutes from the beginning of the observation in absence of the magnet. Scale bars are 20 μm.

the hemozoin crystals in the analyzed blood sample (i.e. $\sim$50 μl) should be captured in a shorter time.

Observation time does not start as soon as the solution is poured on the sample, because some operations need to be performed to properly visualize it, i.e. insert the immersion objective in the solution and focus on the sample surface. Some hemozoin crystals can be seen also in the images at t=0 minutes (Figure 5.10a-c(i)) because they have been captured in this short time interval. Moreover, as observed for magnetic beads, capture seems to occur preferentially along the edges of the pillar surface also for hemozoin crystals.

Similarly to beads, in absence of the permanent magnets system hemozoin crystals move downwards only due to sedimentation. The monitoring time is long enough to observe a uniform sedimentation of the particles on the whole sample surface, without any specific attraction towards the pillars.

The simulation platform developed in *COMSOL Multiphysics* to study the feasibility of the detection device, described in section 3.2, has been validated considering the conditions of real experiments on hemozoin crystals, i.e. with the system of permanent magnets underneath the sample providing $\nabla H^2 \approx 2 \cdot 10^{14}$ A^2/m^3. A HCP array of 20 μm-diameter *Ni* cylinder with a 60 μm spacing has been simulated, considering particles released at 50 μm from the sample surface. The result of the *Particle tracing* simulation after 30 minutes is shown in Figure 5.11. Almost all the particles released at 50 μm from the surface are captured within this amount of time. Despite an accurate comparison of the capture times between simulation and tests on real devices cannot be performed because in the latter particles are dispersed at different distances from the sample surface, the order of magnitude of the capture mechanism duration is the same. Furthermore, almost all particles are captured in both cases. However, in simulations particles are attracted in the center of the surface of the pillars, while in tests on real devices capture occurred preferentially close to the edges. Although additional tests on pillars with a more regular surface are required, also some simulation conditions should be reconsidered. Indeed, as a first approximation it was imposed that the particles stop when reaching the sample surface. Removing this constrain and giving them the possibility to move may result in different outcomes, considering the contribution of the radial force due to the magnetic field gradient produced due to the *Ni* microstructures (see section 3.2.4).
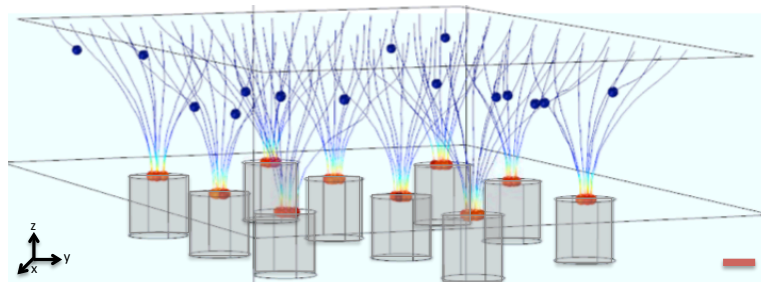

Figure 5.11: 3D view representation of the trajectories of hemozoin crystals, released at z=50 μm from the chip surface. Scale bar is 10 μm; particle dimensions are not in scale. Image obtained with *COMSOL Multiphysics*.

5.3.3 Treated and untreated red blood cells

Magnetic capture experiments have been carried out also on red blood cells, treated according to the protocol described in section 4.4 to become paramagnetic and stained with a TRITC marker (*CellTracker^{TM} Red CMTPX Dye*, Thermo Fisher Scientific). The relative susceptibility of RBCs whose hemoglobin has been completely converted in metHb is $3.9 \cdot 10^{-6}$ [21,67], but a quantification of the extent of the conversion within the samples we tested has not been possible so far. Capture dynamics is slower with respect to beads but faster than hemozoin crystals, indeed the magnetic force is lower but the contribution related to sedimentation is much more relevant, considering RBCs micrometric dimensions. Therefore, capture dynamics was monitored for a shorter time, i.e. around 20 minutes from the pouring of the solution of RBCs in PBS (concentration 0.012%). A longer observation is not required, since within this period of time all erythrocyte have reached the sample surface. Experiments were carried out both on treated RBCs (t-RBCs) and untreated ones (ut-RBCs), in order to check the effectiveness of the treatment. In addition, control tests in absence of the system of permanent magnets were performed for both particles (i.e. t-RBCs and ut-RBCs), using the sample with the closest pillars (i.e. spacing 60 μm) because it proved to have the highest attraction capabilities in the experiments carried out with the other particles (i.e. magnetic beads and hemozoin crystals).

The examined patterns are the same considered in the previous sections, i.e. 25 μm-diameter pillars with 60 μm spacing (Figure 5.12), 30 μm-diameter pillars with 80 μm spacing (Figure 5.13) and 45 μm-diameter pillars with 160 μm spacing (Figure 5.14). For each pattern, images of the sample during the capture experiments with t-RBCs and ut-RBCs are shown respectively in the first and second rows, at the beginning of the observation and after 10 and 20 minutes. Moreover, for the sample with a spacing 60 μm images of the tests performed in absence of the external magnets are shown in the last two rows (Figure 5.12). Some RBCs are present also in the images at t=0 minutes due to sedimentation or magnetic capture that occurred in the short amount of time during which the operations needed to properly visualize the sample after the pouring of the solution were performed, as it happened for hemozoin crystals.

In the samples with closer pillars, i.e. the ones in Figure 5.12 and Figure 5.13, all the treated RBCs are captured on the concentrators in presence of the external field, while a uniform sedimentation occurs for ut-RBCs. In addition, a uniform sedimentation, with no significant differences between treated and untreated RBCs, is present also in the control tests carried out
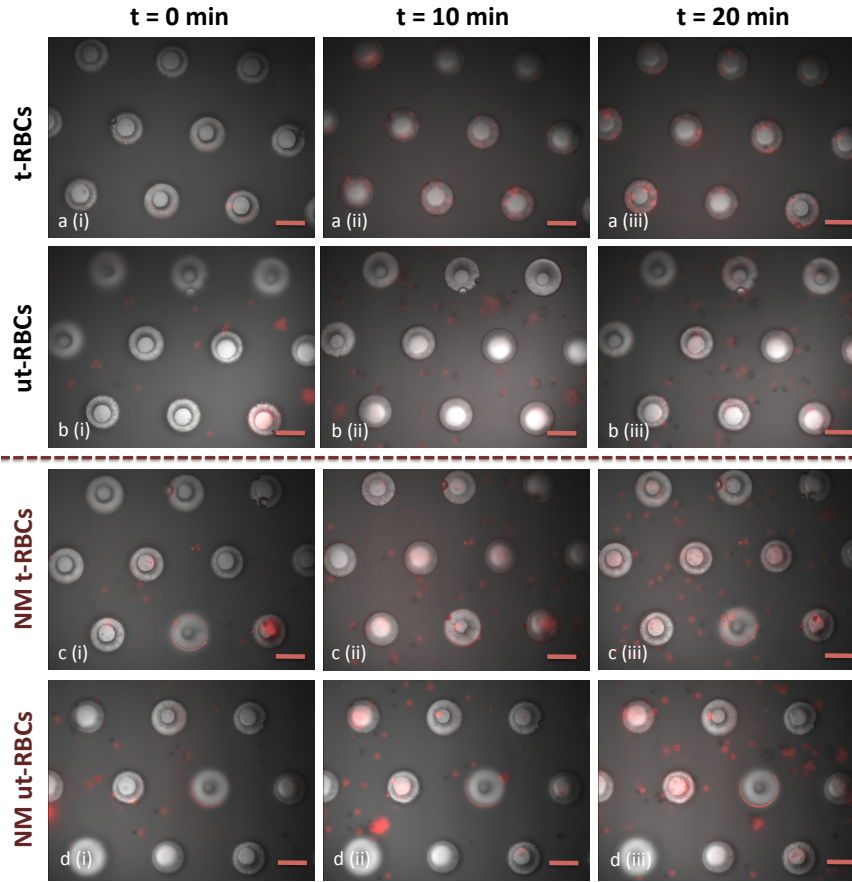
Figure 5.12: Results of the RBCs magnetic capture experiments carried out on the HCP array with d=25μm and s=60μm. Rows correspond to the different tested particles, i.e. t-RBCs and ut-RBCs; NM indicates the control tests without the external magnets. Each column represents a different time, i.e.0-10-20 minutes from the beginning of the observation. Scale bars are 20 μm.

in absence of the external magnets (Figure 5.12c-d). However, the presence of clusters of particles, like the ones in Figure 5.12d(ii) and Figure 5.13b(iii), can affect uniformity. Cluster formation might be a consequence of the staining with the fluorescent marker, since this phenomenon was not present when unmarked RBCs were tested in preliminary experiments.

Conversely, the capture efficiency of t-RBCs in the 160 μm-spaced array with 45 μm diameter pillars (Figure 5.14) is slightly lower. Indeed, some t-RBCs outside the concentrator can be seen in Figure 5.14a(iii). Nevertheless, there is a clear difference with the uniform distribution that results from the test on ut-RBCs (Figure 5.14b(iii)). Also in this case a preferential capture of t-RBCs along the edges occurs, similarly to beads and hemozoin crystals.
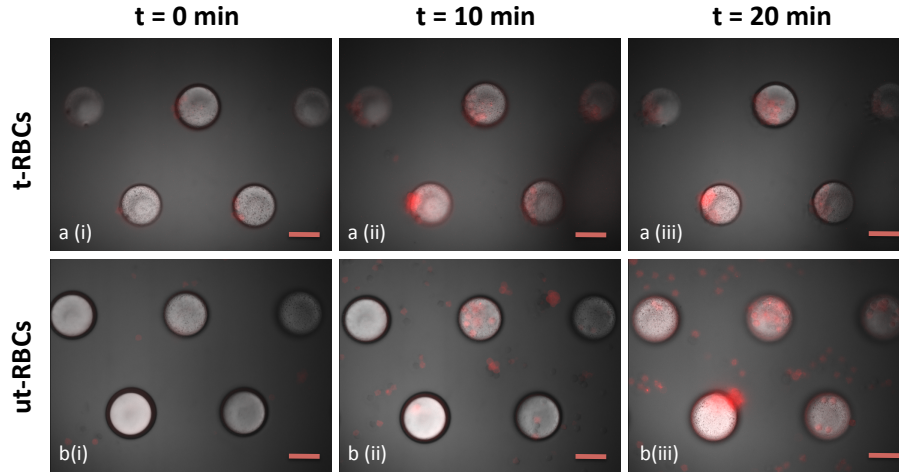
Figure 5.13: Results of the RBCs magnetic capture experiments carried out on the HCP array with d=30μm and s=80μm. Rows correspond to the different tested particles, i.e. t-RBCs and ut-RBCs. Each column represents a different time, i.e.0-10-20 minutes from the beginning of the observation. Scale bars are 20 μm.

Figure 5.14: Results of the RBCs magnetic capture experiments carried out on the HCP array with d=45μm and s=160μm. Rows correspond to the different tested particles, i.e. t-RBCs and ut-RBCs. Each column represents a different time, i.e.0-10-20 minutes from the beginning of the observation. Scale bars are 20 μm.

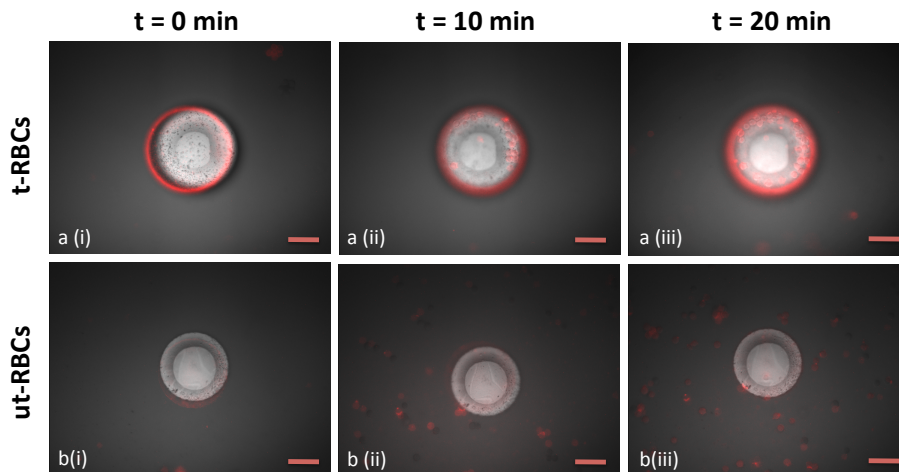| d (μm)	s (μm)	**Magnet**	η_{t-RBC}	η_{ut-RBC}	$\Delta\eta/\eta$
25	60	Yes	100%	31%	5%
25	60	No	33%	17%	5%
30	80	Yes	100%	37%	5%
45	160	Yes	55%	0%	20%

Table 5.1: Capture efficiency of t-RBCs and ut-RBCs for different patterns, in presence or in absence of the system of permanent magnets.

Contrary to beads and hemozoin crystals, red blood cells can be distinguished and counted. Thus, considering the number of RBCs captured (n_C) or not captured (n_{NC}) by nickel pillars in the field of view of the analyzed optical microscopy image, it is possible to estimate capture efficiency η of the microstructures, defined as:

$$\eta = \frac{n_C - \frac{n_{NC}}{A_{out}} A_{in}}{n_C + n_{NC}} \qquad (5.2)$$

where A_{IN} is the area of the cylinder base and A_{OUT} is the bare substrate area outside the pillars. This definition allows to subtract the contribution related to the natural sedimentation of the cells. Indeed, sedimentation is supposed to give a uniform density of particles over the entire chip, which is estimated as n_{NC}/A_{out}, i.e. the number of RBCs not captured divided by the area surrounding the pillars.

The amount of RBCs on the samples used in capture experiments was evaluated at the end of observations, i.e. after 20 minutes. An estimate of the capture efficiency for the different analyzed samples is indicated in Table 5.1, together with the uncertainty arising from the unavoidable error in the count of the number of RBCs. A complete capture, corresponding to 100% capture efficiency, is achieved for the patterns where *Ni* pillars are more packed and have an aspect ratio closer to 1 (i.e. samples with d=25μm, s=60μm and d=30μm, s=80μm), while it is only partial for the 45 μm-diameter concentrator in the pattern with 160 μm spacing, leading to a capture efficiency on the order of 55%. Indeed, a lower efficiency was expected for the latter pattern, considering the reduced aspect ratio and the larger spacing. On the other hand, the larger relative uncertainty for this sample is simply due to the reduced number of pillars (just one) in the field of view, thus worsening the statistical quality of data. In agreement with the behavior of the patterns in tests with treated RBCs, when the untreated sample was analyzed no capture occurred for the 45 μm-pillars sample but,
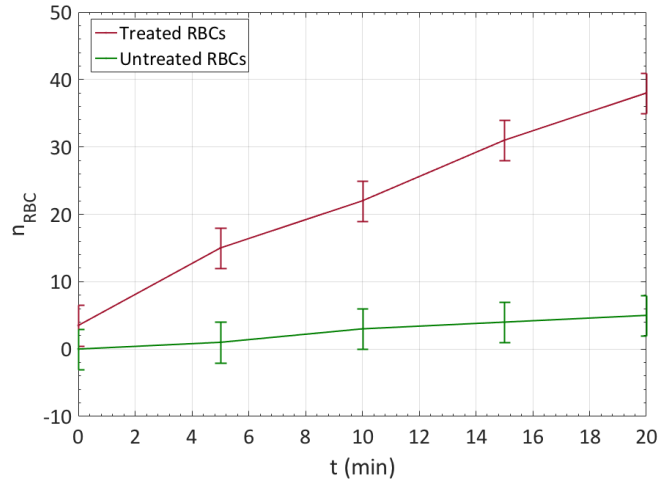
Figure 5.15: Temporal evolution of the the number of RBCs on top of a 45 μm-diameter *Ni* pillar.

surprisingly, a capture efficiency >30% resulted for the other two. This unspecific attraction of untreated RBCs may be related to the operations required for the blood sample preparation (i.e. resuspension and staining), as well as the presence of clusters. Note also that, even in absence of the external magnets, the capture efficiency is non null and higher for the treated blood sample. As a matter of fact, weak attraction of t-RBCs may results from the remanence magnetization present in *Ni* concentrators even after the removal of the external magnet. Finally, the variability on the number of RBCs captured by different concentrators is high, due to irregularities of the pillar surface and possibly to non uniformity of the biological sample. Thus, a further optimization both on blood sample preparation and pillars fabrication is required to improve the repeatability of the experiments.

The temporal evolution of the number of RBCs on top of a 45 μm-diameter *Ni* pillar for both treated and untreated blood samples is shown in Figure 5.15. Despite a contribution related to sedimentation is present in both cases, for the treated sample the increase is steeper and the reached value higher. This definitely confirms the selective capture of t-RBCs by magnetic pillars.

Also in the case of treated erythrocytes, some simulations of capture experiments in the direct geometry compatible with optical microscopy observation, i.e. with the external magnets underneath the chip, have been carried out. A HCP array of 20 μm-diameter *Ni* cylinder with a 60 μm spacing has been simulated, reproducing a situation similar to the case of

Figure 5.12. As observed in experiments, RBCs have a capture dynamics that is much faster with respect to that of hemozoin crystals. This is partially due to a more relevant sedimentation, but also to the fact that bigger particles move faster in the same field of forces. This is evident, for instance, considering that the steady state velocity (see Eq. (2.17) in section 2.3) is proportional to the square of the particle radius. Simulation result, shown in Figure 5.16, indicates that all the particles released at 50 μm from the sample surface are captured on the pillars. Capture time is on the order of 5 minutes, much shorter than that observed in experiments on fabricated devices. This can be easily explained, because RBCs are dispersed in a larger volume with a few mm thickness.
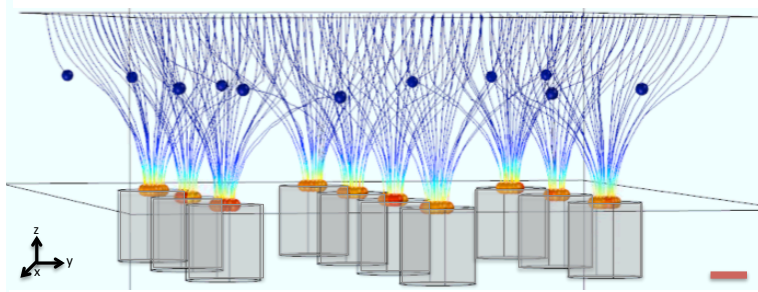
Figure 5.16: 3D view representation of the trajectories of t-RBCs, released at z=50 μm from the chip surface. Scale bar is 10 μm; particle dimensions are not in scale. Image obtained with *COMSOL Multiphysics*.

5.4 Impedance detection measurements

The designed diagnostic device combines magnetic capture and electrical impedance detection. Thus, for the sake of completeness, the main results of electrical tests, performed to measure the impedance variation caused by the presence of particles on top of micrometric gold electrodes, are presented. These tests were carried out by Prof. Marco Sampietro's group; I contributed to the fabrication of simplified test devices integrating nickel microstructures and electrodes, as described afterwards.

Preliminary measurements were carried out on the deeply studied interdigitated electrodes, then also circular electrodes like the ones described in section 3.1 have been used used. Different particles were tested, i.e. 1 μm magnetic beads (*MyOne-Dynabeads*, Thermo Fisher Scientific-USA), red blood cells and hemozoin crystals, all dispersed in a PBS solution. Before electrical tests, preliminary operations were carried out on the device. A

tank in PDMS (Polydimethylsiloxane), a silicon-based organic polymer, was bonded on the sample surface to allow the pouring in a limited region above the electrodes of the solutions containing the particles to test. Moreover, an electrical contact between the device and the electronic setup was set up by welding copper cables to electrodes pads with silver paste. During tests, a sinusoidal voltage with a frequency of 2 MHz was provided with a lock-in amplifier and then the current flowing through device under test (DUT) was measured, both in presence and in absence of the particles, after being converted into a voltage with a transimpedance amplifier.

Different strategies were adopted to measure the impedance of the solution with and without particles in the proximity of the electrodes. A possible way is to measure first the buffer solution (PBS for these tests) and only after some time inject the particles with a micropipette. However, particle injection itself causes an impedance variation, thus its contribution needs to be removed from the total signal to calculate only the variation related to the particles. Alternatively, a PBS solution already containing the particles can be poured on the electrodes. At the beginning of the test the system is in reversed configuration (i.e. with electrodes above the solution), such that particles sediment in the opposite direction with respect to the electrodes, thus allowing a measure of the solution resistance alone. Once a stable signal is reached, the system can be turned in direct configuration (i.e. with electrodes below the solution), this time favoring particle sedimentation towards the electrodes to measure their contribution. This technique was used in measurement performed on red blood cells and hemozoin crystals, with the additional contribution of a permanent magnet for the latter.

A similar strategy can be adopted also to measure magnetic particles, exploiting magnetic force instead of sedimentation. Indeed, by keeping the system in reversed configuration for the whole test and inserting a permanent magnet when PBS impedance is sufficiently stable, magnetic particles can be attracted upwards towards the electrode, thus allowing to measure how their presence affects the impedance. These detection conditions are similar to the one designed for the final device, but so far they have been used only on magnetic beads because the currently used permanent magnet is not sufficiently strong to attract hemozoin crystals and treated RBCs. Moreover, a complete integration with nickel concentrators has not been achieved yet because, currently, electrodeposition is not able to guarantee a sufficiently planar and smooth surface to allow a precise definition of the micrometric features of the electrodes.

To achieve a first integration of magnetic capture and electrical detection, simplified test devices were fabricated, where much thinner (50 nm) Ni pillars

were grown by electron-beam evaporation instead of electroplating. The main steps involved in the fabrication of the simplified test device are the following:

- Direct photolithography with AZ5214E to define the circles pattern;

- E-beam evaporation of a 50 nm Ni layer on the whole sample;

- Lift off of the photoresist, such that 50 nm-height Ni pillars are left;

- E-beam evaporation of 100 nm of SiO_2 as capping layer;

- Inverse photolithography with AZ5214E to pattern the electrodes;

- Magneton sputtering of a 30 nm Cr adesive layer and a 100 nm Au layer;

- Lift off of the photoresist, such that Au electrodes are left;

- Direct photolithography with SU8-2005 to mask electrical connections.

Since the reduced thickness of the evaporated nickel concentrators is not sufficient to attract and concentrate hemozoin crystals or infected red blood cells, electrical tests were performed using 1 μm superparamagnetic beads. Indeed, with Ni pillars below the circular electrodes magnetic capture should be more localized in the sensing volume of the electrodes, i.e. close to the cylinder edges. In Figure 5.17 some Ni pillars with electrodes on top are shown, as they appear at the end of an electrical test in which magnetic beads have been attracted towards the electrodes with a magnet. Unfortunately, magnetic particles were not completely concentrated in the sensing area of the electrodes, due to reduced height of Ni concentrators.
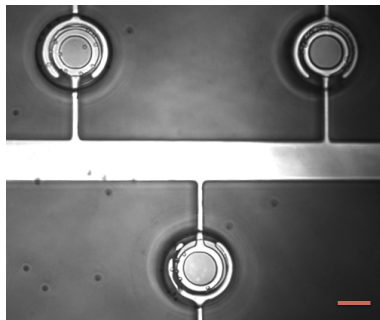
Figure 5.17: Portion of a simplified test device with Ni pillars fabricated below circular electrodes, at the end of an electrical test in which magnetic beads have been attracted towards the electrodes with a magnet. Scale bar is 10 μm.
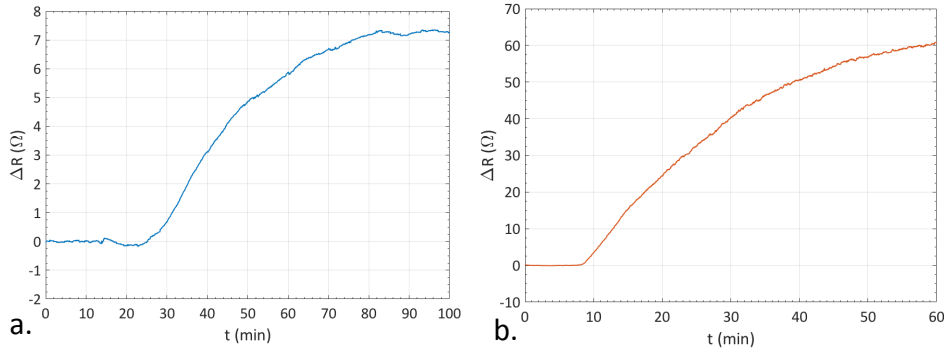
Figure 5.18: Temporal evolution of the resistance variation in a solution containing hemozoin crystals (**a.**) or RBCs (**b.**).

No matter the mechanism used to bring tested particles on top of the electrodes, every time they were in the sensing volume of the electrodes a lower current (and so a higher impedance) was measured. Therefore, all the tested particles (i.e. beads, RBCs and hemozoin crystals) have a conductivity lower than PBS (i.e. 1.5 S/m at room temperature). However, the time required to detect an impedance variation was very different according to the analyzed particle. For magnetic beads 5 minutes-tests were sufficient, while around 1 hour and 2 hours-lasting measurements were needed for RBCs and hemozoin crystals. Indeed, a long period of time was required to have complete sedimentation of these particles due to the thickness (i.e. a few mm) of the tested solution droplet. Temporal evolution of the resistance variation in solutions containing of hemozoin crystals or RBCs is shown in Figure 5.18a and Figure 5.18b, respectively.

The number of hemozoin crystals, RBCs and 1 μm beads in the sensing area of the electrodes could be estimated by observing the sample surface at the end of the tests, using a *Nikon ECLIPSE* optical microscope with a 60x water immersion objective (the same exploited in capture experiments). Considering the sensing volume of the electrodes, the number of particles was converted in volumetric fraction (Φ). Then, the relative impedance variation caused by the presence of these particles with respect to the initial PBS solution (i.e. $\Delta R/R_0$) was plotted as a function of the volumetric fraction. The points obtained considering the results of different experiments performed using circular electrodes (with and without *Ni* concentrators below) are shown in Figure 5.19. The red dashed line is the theoretical curve arising from Eq. (2.25), $\Delta R/R_0 = 3/2\,\Phi$, which can be derived assuming that particles have null conductivity. Since the behavior of beads and RBCs
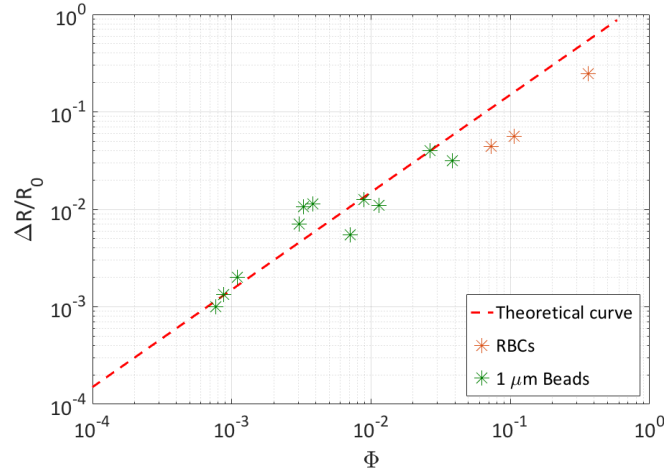
Figure 5.19: Relative impedance variation caused by the presence of different particles in PBS solution as a function of the volumetric fraction Φ.

follows the same trend, our data confirm the insulating behavior of these particles.

Conversely, an accurate estimate of the number of particles was not feasible for hemozoin crystals because single crystals could not be distinguished in the images acquired with the optical microscope. Therefore, with these tests it was not possible to state that hemozoin is insulating, but only that it has a conductivity lower than PBS. As discussed in section 5.1.2, hemozoin crystals show an insulating behavior for a DC current but tests at higher frequencies (like the 2 MHz used in impedance measurements) have not been performed yet. Thus, a further analysis is still required to reach a complete characterization of the electrical properties of hemozoin crystals.

5.5   Summary of the main results and future steps

In conclusion, the feasibility of the project has been validated by the obtained experimental results. The evaluation of hemozoin crystals magnetic susceptibility confirmed the paramagnetic behavior of the particles, in disagreement with the recent idea of a superparamagnetic character, proposed by Inyushin et al.[64]. Additional measurements to check our result on a different batch of hemozoin crystals have been planned, but the absence of a superparamagnetic behavior would have strong implication on the design of the diagnostic test. In addition, with the investigation of hemozoin electrical conductivity it has been possible to establish its insulating behavior at low frequency, even though a complete characterization in various frequency

ranges has not been performed so far. This is a very important result, as it makes feasible a quantification of red blood cells and possibly hemozoin crystals with an electrical impedance measurement.

Moreover, the fabrication process of micrometric nickel concentrators has been developed, with a particular focus on the growth by electroplating. The fabricated microstructures proved their magnetic attraction capabilities, that can be exploited also in different systems where a magnetic separation is required. The next step is a further optimization of the electrodeposition process, required in order to obtain a planar surface that allows the integration of gold electrodes with the magnetic microstructures.

It has been demonstrated that the external permanent magnets and the micrometric nickel concentrators are able to attract and concentrate magnetic particles in specific areas. Indeed, in magnetic capture experiments performed with superparamagnetic beads, hemozoin crystals and treated red blood cells, a 100% capture efficiency has been achieved for some patterns. A fundamental step in the future phase of the project is the development of an experimental setup to monitor capture tests carried out in reversed configuration (i.e. with external magnets above the chip), thus exploiting the competition between gravity ad magnetic force to specifically attract hemozoin crystals and infected RBCs towards the chip with sensing electrodes. In addition, a system of external magnets, able to provide a 10 times more intense field gradient with respect to the prototype realized in this thesis work, is required to attract the targeted particles towards the sensing electrodes, within a 500 μ-thick blood drop and in a reasonable time, on the order of 10–20 minutes.

Finally, preliminary experiments performed in cooperation with the group headed by Prof. Marco Sampietro have shown the feasibility of a combined magnetophoretic attraction and impedance detection on chip, at least in the case of synthetic magnetic beads.

Chapter 6

Conclusions and perspectives

The TID MEKII project aims at the development of an accurate, rapid, easy to use and low-cost detection system for malaria, exploiting magnetic capture of hemozoin crystals and infected red blood cells and a quantification of their concentration via an electrical impedance variation measurement. During this thesis work, the feasibility of the diagnostic device has been demonstrated with numerical simulations and preliminary experiments on test devices.

First, a multiphysics simulation platform has been developed, to study magnetic properties of both micrometric nickel structures and macroscopic permanent magnets, together with the effect of the magnetic force they produce on magnetic particles moving inside a fluid. Different geometries for the micrometric concentrators have been simulated, but the final layout will be optimized only after combined experiments of capture and detection, which will be performed in the next phase of the project. Nevertheless, attraction of hemozoin crystals and infected red blood cells at a distance up to 500 μm from the chip surface and concentration of these particles in localized areas have been proved. In addition, considering the main results of magnetic and electrical simulations, a suitable layout for a chip able to detect the amount of red blood cells corresponding to the targeted limit of detection has been designed. Conversely, a further optimization is still required to obtain a detectable signal also for a concentration of hemozoin crystals corresponding to the targeted limit of detection. A possible solution to reduce the sensing area of the electrodes, thus increasing the impedance variation, could be the use of an additional in-plane magnetic field to concentrate the captured particles in more localized spots. Another possibility would be to improve the electronic sensitivity, by increasing the integration time during measurements (i.e. reducing the low-pass filter band of the lock-in amplifier), as the

capture process is definitely slow.

Furthermore, a fabrication process able to create the designed micrometric nickel structures has been implemented. In particular, the growth by electroplating of nickel micrometric pillars has been developed. Despite a further optimization is still needed in order to obtain a planar surface that allows the fabrication of the electrodes on top of the concentrators, many progresses have been achieved so far. Indeed, this is the first example of microfabrication by electroplating performed in the *Polifab* cleanroom. The magnetic capture efficiency of these structures has been demonstrated in tests performed with hemozoin crystals, red blood cells and superparamagnetic beads. So far these tests have been carried out in direct configuration, i.e. with the external magnets underneath the sample. Since in the designed device a separation of malaria biomarkers from the other blood cells is obtained with magnetic force opposing sedimentation, tests in reverses configuration (i.e. with the external magnets above the sample) are fundamental. Therefore, a proper setup that allows to monitor experiments performed in this configuration and a different system of external magnets able to provide a more intense magnetic field gradient are required.

Moreover, capture experiments provided an additional tool to characterize the magnetic properties of hemozoin, thus confirming the order of magnitude of the magnetic susceptibility evaluated with a Vibrating Sample Magnetometer. In addition, they allowed to test the effectiveness of the erythrocytes treatment protocol developed by the $\mu BS\ Lab$, leaded by Prof. Gianfranco B. Fiore. Indeed, preliminary tests on a bovine blood model of infected erythrocytes are the first steps towards the analysis of human blood samples.

Finally, preliminary electrical tests carried out by the I^3N group, leaded by Prof. Marco Sampietro, proved that red blood cells are insulating and can be detected with an impedance variation. A complete characterization of hemozoin crystals in various frequency ranges has not been performed so far, but conductive AFM measurements proved that they show an insulating behavior in low frequency.

The next step is definitely the integration of the two processes for the fabrication of nickel concentrators and gold electrodes on the same chip. This is crucial to perform detection experiments of hemozoin crystals and infected RBCs, first in model bovine blood samples and then on human samples.

Bibliography

[1] Centers for Disease Control and Prevention, "Malaria Parasites." `https://www.cdc.gov/malaria/about/biology/parasites.html`. Accessed: November 2017.

[2] World Health Organization, "Malaria Fact Sheet." `http://www.who.int/mediacentre/factsheets/fs094/en/`. Accessed: November 2017.

[3] World Health Organization, "Malaria Rapid Diagnostic Test Performance," 2017.

[4] S. Kasetsirikul, J. Buranapong, W. Srituravanich, M. Kaewthamasorn, and A. Pimpin, "The development of malaria diagnostic techniques: a review of the approaches with focus on dielectrophoretic and magnetophoretic methods," *Malar. J.*, vol. 358, no. 15, 2016.

[5] "What is malaria?." `https://www.yourgenome.org/facts/what-is-malaria`. Accessed: November 2017.

[6] L. M. Coronado, C. T. Nadovich, and C. Spadafora, "Malarial hemozoin: from target to tool," *Biochim. Biophys. Acta - Mol. Basis Dis.*, vol. 1840, no. 6, pp. 2032–2041, 2014.

[7] D. A. Milner, "Pathogenesis of Malaria," *Parasitol. Today*, vol. 16, no. 10, pp. 451–454, 2000.

[8] B. Autino, Y. Corbett, F. Castelli, and D. Taramelli, "Pathogenesis of malaria in tissues and blood," *Mediterr. J. Hematol. Infect. Dis.*, no. 4, 2012.

[9] L. R. Moore, H. Fujioka, P. S. Williams, J. J. Chalmers, B. Grimberg, P. A. Zimmerman, and M. Zborowski, "Hemoglobin degradation in malaria-infected erythrocytes determined from live cell magnetophoresis," *FASEB J.*, vol. 20, no. 6, pp. 747–749, 2006.

[10] A. F. Cowman, D. Berry, and J. Baum, "The cellular and molecular basis for malaria parasite invasion of the human red blood cell," *J. Cell Biol.*, vol. 198, no. 6, pp. 961–971, 2012.

[11] L. Roberts, "Malaria wars," *Science*, vol. 352, no. 6284, pp. 398–405, 2016.

[12] K. A. De Villiers and T. J. Egan, "Recent advances in the discovery of haem-targeting drugs for malaria and schistosomiasis," *Molecules*, vol. 14, no. 8, pp. 2868–2887, 2009.

[13] J. Ziegler, R. Linck, and D. W. Wright, "Heme Aggregation Inhibitors: Antimalarial Drugs Targeting an Essential Biomineralization Process," *Curr. Med. Chem.*, vol. 8, no. 2, pp. 171–189, 2001.

[14] T. J. Egan, "Physico-chemical aspects of hemozoin (malaria pigment) structure and formation," *J. Inorg. Biochem.*, vol. 91, no. 1, pp. 19–26, 2002.

[15] C. Coban, M. Yagi, K. Ohata, Y. Igari, T. Tsukui, T. Horii, K. J. Ishii, and S. Akira, "The Malarial Metabolite Hemozoin and Its Potential Use as a Vaccine Adjuvant," *Allergol. Int.*, vol. 59, no. 2, pp. 115–124, 2010.

[16] S. Hackett, J. Hamzah, T. M. E. Davis, and T. G. St Pierre, "Magnetic susceptibility of iron in malaria-infected red blood cells," *Biochim. Biophys. Acta - Mol. Basis Dis.*, vol. 1792, no. 2, pp. 93–99, 2009.

[17] L. Pauling and C. D. Coryell, "The Magnetic Properties and Structure of Hemoglobin, Oxyhemoglobin and Carbonmonoxyhemoglobin," *Proc. Natl. Acad. Sci.*, vol. 22, no. 4, pp. 210–216, 1936.

[18] C. C. Kim, E. B. Wilson, and J. L. DeRisi, "Improved methods for magnetic purification of malaria parasites and haemozoin.," *Malar. J.*, vol. 17, no. 9, 2010.

[19] M. E. Ali and P. M. Oppeneer, "Unraveling the electronic structure, spin states, optical and vibrational spectra of malaria pigment," *Chem. - A Eur. J.*, vol. 21, no. 23, pp. 8544–8553, 2015.

[20] A. Butykai, A. Orbán, V. Kocsis, D. Szaller, S. Bordács, E. Tátrai-Szekeres, L. F. Kiss, A. Bóta, B. G. Vértessy, T. Zelles, and I. Kézsmárki, "Malaria pigment crystals as magnetic micro-rotors: key for high-sensitivity diagnosis," *Sci. Rep.*, vol. 1431, no. 3, 2013.

[21] J. Nam, H. Huang, H. Lim, C.-S. Lim, and S. Shin, "Magnetic separation of malaria-infected red blood cells in various developmental stages," *Anal. Chem.*, vol. 15, no. 85, pp. 7316–7323, 2013.

[22] N. Tangpukdee, C. Duangdee, P. Wilairatana, and S. Krudsood, "Malaria diagnosis: A brief review," *Korean J. Parasitol.*, vol. 47, no. 2, pp. 93–102, 2009.

[23] C. K. Murray, R. A. Gasser, A. J. Magill, and R. S. Miller, "Update on rapid diagnostic testing for malaria," *Clin. Microbiol. Rev.*, vol. 21, pp. 97–110, jan 2008.

[24] "PCR Cycling Parameters." `https://www.thermofisher.com/uk/en/home/life-science/cloning/cloning-learning-center/invitrogen-school-of-molecular-biology/pcr-education/pcr-reagents-enzymes/pcr-cycling-considerations.html`. Accessed: November 2017.

[25] D. Payne, "Use and limitations of light microscopy for diagnosing malaria at the primary health care level.," *Bull. World Health Organ.*, vol. 66, no. 5, pp. 621–626, 1988.

[26] D. C. Warhurst and J. E. Williams, "Laboratory diagnosis of malaria.," *J. Clin. Pathol.*, vol. 49, no. 7, pp. 533–538, 1996.

[27] A. Moody, "Rapid diagnostic tests for malaria parasites," *Clin. Microbiol. Rev.*, vol. 15, no. 1, pp. 66–78, 2002.

[28] C. Wongsrichanalai, M. J. Barcus, S. Muth, A. Sutamihardja, and W. H. Wernsdorfer, "A review of malaria diagnostic tools: Microscopy and rapid diagnostic test (RDT).," *Am. J. Trop. Med. Hyg.*, vol. 77, no. SUPPL. 6, pp. 119–127, 2007.

[29] G. Díaz, F. A. González, and E. Romero, "A semi-automatic method for quantification and classification of erythrocytes infected with malaria parasites in microscopic images," *J. Biomed. Inform.*, vol. 42, no. 2, pp. 296–307, 2009.

[30] D. K. Das, A. K. Maiti, and C. Chakraborty, "Automated system for characterization and classification of malaria infected stages using light microscopic images of thin blood smears," *Journal of Microscopy*, vol. 257, pp. 238–252, 3 2015.

[31] C. W. Pirnstill and G. L. Coté, "Malaria Diagnosis Using a Mobile Phone Polarized Microscope," *Sci. Rep.*, vol. 13368, no. 5, 2015.

[32] S. A. Khan, S. Ahmed, N. Mushahid, M. Anwer, S. Saeed, F. A. Khan, G. U. Shamshad, and Z. Joyia, "Comparison of real time polymerase chain reaction with microscopy and antigen detection assay for the diagnosis of malaria.," *J. Coll. Physicians Surg. Pak.*, vol. 23, no. 10, pp. 787–92, 2013.

[33] N. Steenkeste, S. Incardona, S. Chy, L. Duval, M.-T. Ekala, P. Lim, S. Hewitt, T. Sochantha, D. Socheat, C. Rogier, O. Mercereau-Puijalon, T. Fandeur, and F. Ariey, "Towards high-throughput molecular detection of Plasmodium: new approaches and molecular markers," *Malar. J.*, vol. 8, no. 1, p. 86, 2009.

[34] D. T. McNamara, L. J. Kasehagen, B. T. Grimberg, J. Cole-Tobian, W. E. Collins, and P. A. Zimmerman, "Diagnosing infection levels of four human malaria parasite species by a PCR/LDR fluorescent microsphere-based assay," *Am. J. Trop. Med. Hyg.*, vol. 73, no. 3, pp. 20–21, 2005.

[35] K. S. Hansen, E. Grieve, A. Mikhail, I. Mayan, N. Mohammed, M. Anwar, S. H. Baktash, T. L. Drake, C. J. M. Whitty, M. W. Rowland, and T. J. Leslie, "Cost-effectiveness of malaria diagnosis using rapid diagnostic tests compared to microscopy or clinical symptoms alone in Afghanistan," *Malar. J.*, vol. 217, no. 14, 2015.

[36] M. S. Alam, A. N. Mohon, S. Mustafa, W. A. Khan, N. Islam, M. Karim, H. Khanum, D. J. Sullivan, and R. Haque, "Real-time PCR assay and rapid diagnostic tests for the diagnosis of clinically suspected malaria patients in Bangladesh," *Malar. J.*, vol. 175, no. 10, 2011.

[37] L. Fransisca, J. Kusnanto, T. Satoto, B. Sebayang, . Supriyanto, E. Andriyan, and M. J. Bangs, "Comparison of rapid diagnostic test Plasmotec Malaria-3, microscopy, and quantitative real-time PCR for diagnoses of Plasmodium falciparum and Plasmodium vivax infections in Mimika Regency, Papua, Indonesia," *Malar. J.*, vol. 14, no. 1, 2015.

[38] V. Batwala, P. Magnussen, and F. Nuwaha, "Comparative feasibility of implementing rapid diagnostic test and microscopy for parasitological diagnosis of malaria in Uganda," *Malar. J.*, vol. 373, no. 10, 2011.

[39] I. M. Masanja, M. L. McMorrow, M. B. Maganga, D. Sumari, V. Udhayakumar, P. D. McElroy, S. Kachur, and N. W. Lucchi, "Quality assurance of malaria rapid diagnostic tests used for routine patient

care in rural Tanzania: microscopy versus real-time polymerase chain reaction," *Malar. J.*, vol. 14, no. 1, p. 85, 2015.

[40] N. Pamme, "Magnetism and microfluidics," *Lab Chip*, vol. 6, no. 1, pp. 24–38, 2006.

[41] G. J. Dolan and L. W. Terstappen, "Magnetic separation apparatus and methods employing an internal magnetic capture gradient and an external transport force," in *United States Pat.*, 1997.

[42] M. Carminati, G. Ferrari, S. U. Kwon, M. Sampietro, M. Monticelli, A. Torti, D. Petti, E. Albisetti, M. Cantoni, and R. Bertacco, "Towards the impedimetric tracking of single magnetically trailed microparticles," in *2014 IEEE 11th Int. Multi-Conference Syst. Signals Devices, SSD 2014*, pp. 1–5, 2014.

[43] Q. Ramadan, D. P. Poenar, and C. Yu, "Customized trapping of magnetic particles," *Microfluid. Nanofluidics*, vol. 6, no. 1, pp. 53–62, 2009.

[44] Q. Ramadan, V. Samper, D. Poenar, and C. Yu, "On-chip microelectromagnets for magnetic-based bio-molecules separation," *J. Magn. Magn. Mater.*, vol. 281, no. 2-3, pp. 150–172, 2004.

[45] C. W. Yung, J. Fiering, A. J. Mueller, and D. E. Ingber, "Micromagnetic microfluidic blood cleansing device," *Lab Chip*, vol. 9, no. 9, pp. 1171–1177, 2009.

[46] P. Chen, Y. Y. Huang, K. Hoshino, and J. X. Zhang, "Microscale Magnetic Field Modulation for Enhanced Capture and Distribution of Rare Circulating Tumor Cells," *Sci. Rep.*, vol. 8745, no. 5, 2015.

[47] L. R. Moore, F. Nehl, J. Dorn, J. J. Chalmers, and M. Zborowski, "Open gradient magnetic red blood cell sorter evaluation on model cell mixtures," *IEEE Trans. Magn.*, vol. 49, no. 1, pp. 309–315, 2013.

[48] K. H. Han and A. Bruno Frazier, "Continuous magnetophoretic separation of blood cells in microdevlce format," *J. Appl. Phys.*, vol. 96, no. 10, pp. 5797–5802, 2004.

[49] K. H. Han and A. B. Frazier, "Paramagnetic capture mode magnetophoretic microseparator for high efficiency blood cell separations," *Lab Chip*, vol. 6, no. 2, pp. 265–273, 2006.

[50] M. Zborowski, J. J. Chalmers, and W. G. Lowrie, "Magnetic Cell Manipulation and Sorting," in *Microtechnology Cell Manip. Sorting*, pp. 15–56, Springer International Publisher, 2017.

[51] J. Kim, M. Massoudi, J. F. Antaki, and A. Gandini, "Removal of malaria-infected red blood cells using magnetic cell separators: A computational study," *Appl. Math. Comput.*, vol. 218, no. 12, pp. 6841–6850, 2012.

[52] P. A. Zimmerman, J. M. Thomson, H. Fujioka, W. E. Collins, and M. Zborowski, "Diagnosis of malaria by magnetic deposition microscopy," *Am. J. Trop. Med. Hyg.*, vol. 74, no. 4, pp. 568–572, 2006.

[53] S. Vyas, V. Genis, and G. Friedman, "Computational study of a magnetic design to improve the diagnosis of malaria: 2D model," *J. Magn. Magn. Mater.*, vol. 423, pp. 301–305, 2017.

[54] S. C. Bhakdi, A. Ottinger, S. Somsri, P. Sratongno, P. Pannadaporn, P. Chimma, P. Malasit, K. Pattanapanyasat, and H. P. H. Neumann, "Optimized high gradient magnetic separation for isolation of Plasmodium-infected red blood cells," *Malar. J.*, vol. 38, no. 9, pp. 1–9, 2010.

[55] U. Tripathy, M. Giguère-Bisson, M. H. Sangji, M. J. Bellemare, D. S. Bohle, E. Georges, and P. W. Wiseman, "Optimization of malaria detection based on third harmonic generation imaging of hemozoin," *Anal. Bioanal. Chem.*, vol. 405, no. 16, pp. 5431–5440, 2013.

[56] A. Orbán, M. Rebelo, P. Molnàr, I. S. Albuquerque, A. Butykai, and I. Kézsmàrki, "Efficient monitoring of the blood-stage infection in a malaria rodent model by the rotating-crystal magneto-optical method," *Sci. Rep.*, vol. 23218, no. 6, pp. 1–9, 2016.

[57] D. M. Newman, J. Heptinstall, R. J. Matelon, L. Savage, M. L. Wears, J. Beddow, M. Cox, H. D. F. H. Schallig, and P. F. Mens, "A Magneto-Optical route toward the in vivo diagnosis of malaria:preliminary results and preclinical trial data," *Biophys. J.*, vol. 95, no. 2, pp. 994–1000, 2008.

[58] R. Bertacco, E. Albisetti, D. Petti, M. Giacometti, and G. Ferrari, "Dispositivo e metodo per la quantificazione di componenti corpuscolate e non corpuscolate del sangue," in *Italian Patent Application*, 2017.

[59] "COMSOL Multiphysics." `https://www.comsol.it/comsol-multiphysics`. Accessed: November 2017.

[60] J. M. D. Coey, *Magnetism and Magnetic Materials*. New York: Cambridge University Press, 2009.

[61] L. D. Landau, E. M. Lifshitz, and A. L. King, *Electrodynamics of Continuous Media*. Pergamon Press, 1961.

[62] S. Blundell, *Magnetism in condensed matter*. Oxford University Press, 2001.

[63] A. G. Roca, R. Costo, A. F. Rebolledo, S. Veintemillas-Verdaguer, P. Tartaj, T. González-Carreño, M. P. Morales, and C. J. Serna, "Progress in the preparation of magnetic nanoparticles for applications in biomedicine," *Journal of Physics D: Applied Physics*, vol. 42, no. 22, p. 224002, 2009.

[64] M. Inyushin, Y. Kucheryavih, L. Kucheryavih, L. Rojas, I. Khmelinskii, and V. Makarov, "Superparamagnetic Properties of Hemozoin," *Sci. Rep.*, vol. 6, no. 1, p. 26212, 2016.

[65] L. Sakhnini and R. Khuzaie, "Magnetic behavior of human erythrocytes at different hemoglobin states," *Eur. Biophys. J.*, vol. 30, no. 6, pp. 467–470, 2001.

[66] W. Spees, D. Yablonskiy, and M. Oswood, "Water proton MR properties of human blood at 1.5 Tesla: magnetic susceptibility, T_1, T_2, T_2^*, and Non-Lorentzian Signal Behavior," *Magn. Reson. Med.*, vol. 5, no. 4, pp. 533–542, 2001.

[67] M. Zborowski, G. R. Ostera, L. R. Moore, S. Milliron, J. J. Chalmers, and A. N. Schechter, "Red blood cell magnetophoresis," *Biophys. J.*, vol. 84, no. 4, pp. 2638–2645, 2003.

[68] T. Fook Kong, W. Ye, W. K. Peng, H. Wei Hou, Marcos, P. R. Preiser, N.-T. Nguyen, and J. Han, "Enhancing malaria diagnosis through microfluidic cell enrichment and magnetic resonance relaxometry detection," *Sci. Rep.*, vol. 5, no. 1, p. 11425, 2015.

[69] J. P. Savicki, G. Lang, and M. Ikeda-Saito, "Magnetic susceptibility of oxy- and carbonmonoxyhemoglobins." *Proc Natl Acad Sci U S A*, vol. 81, no. 17, pp. 5417–9, 1984.

[70] M. J. Matteucci, W. J. Reed, and D. A. Tanen, "Sodium thiosulfate fails to reduce nitrite-induced methemoglobinemia in vitro," *Acad. Emerg. Med.*, vol. 10, no. 4, pp. 299–302, 2003.

[71] R. O. Wright, B. Magnani, M. W. Shannon, and A. D. Woolf, "N-acetylcysteine reduces methemoglobin in vitro," *Ann. Emerg. Med.*, vol. 28, no. 5, pp. 499–503, 1996.

[72] A. Einstein, "Über die von der molekularkinetischen Theorie der Wärme geforderte Bewegung von in ruhenden Flüssigkeiten suspendierten Teilchen," *Annalen der Physik*, vol. 322, no. 8, pp. 549–560, 1915.

[73] M. Ibrahim, J. Claudel, D. Kourtiche, and M. Nadi, "Geometric parameters optimization of planar interdigitated electrodes for bioimpedance spectroscopy," *Journal of Electrical Bioimpedance*, vol. 4, no. 1, pp. 13–22, 2013.

[74] J. Macdonald, "Impedance spectroscopy," *Annals of Biomedical Engineering*, vol. 20, pp. 289–305, 1991.

[75] E. Du, S. Ha, M. Diez-Silva, M. Dao, S. Suresh, and A. Chandrakasan, "Electric impedance microflow cytometry for characterization of cell disease states," *The Royal Society of Chemistry*, vol. 13, no. 19, pp. 3903–3909, 2013.

[76] P. Simao, *Exploring impedance spectroscopy as a mean of malaria diagnostic.* PhD thesis, IST, 2014.

[77] T. Sun and H. Morgan, "Single-cell microfluidic Impedance cytometry: A review," *Microfluidics and Nanofluidics*, vol. 8, no. 4, pp. 423–443, 2010.

[78] J. Maxwell, *A treatise of Electricity and Magnetism*, vol. 1. Clarendon Press, 1881.

[79] R. DeBlois and C. Bean, "Counting and Sizing of Submicron Particles by the Resistive Pulse Technique," *The American Institute of Physics*, vol. 41, no. 7, pp. 909–916, 1970.

[80] M. Carminati, "Advances in High-Resolution Microscale Impedance Sensors," *Journal of Sensors*, vol. 2017, 2017.

[81] M. Donolato, P. Vavassori, M. Gobbi, M. Deryabina, M. F. Hansen, V. Metlushko, B. Ilic, M. Cantoni, D. Petti, S. Brivio, and R. Bertacco, "On-chip manipulation of protein-coated magnetic beads via domain-wall conduits," *Advanced Materials*, vol. 22, no. 24, pp. 2706–2710, 2010.

[82] M. Monticelli, A. Torti, M. Cantoni, D. Petti, E. Albisetti, A. Manzin, E. Guerriero, R. Sordan, G. Gervasoni, M. Carminati, G. Ferrari, M. Sampietro, and R. Bertacco, "On-chip magnetic platform for single-particle manipulation with integrated electrical feedback," *Small*, vol. 12, no. 7, pp. 921–929, 2016.

[83] "MicroChemicals Photoresists." `http://www.microchemicals.com/products/photoresists.html`. Accessed: November 2017.

[84] "Vacuum RIE machine." `http://www.made-in-zelenograd.com/products/mvu-tm-rit/`. Accessed: November 2017.

[85] "UHV Electron Beam Evaporator." `http://www.dualsignal.com.tw/electron-beam-evaporator-ebe.html`. Accessed: November 2017.

[86] S. A. Al-Bat'hi, "Electrodeposition of Nanostructured Materials," in *Electroplat. Nanostructures*, pp. 1–23, INTECH, 2015.

[87] "Technology - Magnetron Sputtering." `http://farotex.com/technology.html`. Accessed: November 2017.

[88] "EZ9 Vibrating Sample Magnetometer (VSM)." `http://www.microsense.net/products-vsm-ez9.htm`. Accessed: November 2017.

[89] O. Bodansky, "Methemoglobinemia and methemoglobin-producing compounds," *Pharmacological Reviews*, vol. 3, no. 2, pp. 144–191, 1951.

[90] J. W. Harvey, "The Erythrocyte: Physiology, Metabolism, and Biochemical Disorders," in *Clinical Biochemistry of Domestic Animals*, pp. 173–240, San Diego: Academic Press, sixth edition ed., 2008.

[91] M. Zhao, R. Balachandran, Z. Patterson, R. Gouk, S. Verhaverbeke, F. Shadman, and M. Keswani, "Contactless Bottom-Up Electrodeposition of Nickel for 3D Integrated Circuits," *RSC Adv.*, vol. 5, no. 56, pp. 45291–45299, 2015.

[92] A. M. Rashidi and A. Amadeh, "Effect of electroplating parameters on microstructure of nanocrystalline nickel coatings," *J. Mater. Sci. Technol.*, vol. 26, no. 1, pp. 82–86, 2010.

[93] A. Chenna, N. Benbrahim, and A. Kadri, "Electrochemical deposition of Nickel thin films onto monocristalline silicon," *African Rev. Phys.*, vol. 2, pp. 133–134, 2008.

[94] F. Nasirpouri, S. M. Janjan, S. M. Peighambari, M. G. Hosseini, A. Akbari, and A. S. Samardak, "Refinement of electrodeposition mechanism for fabrication of thin nickel films on n-type silicon (1 1 1)," *J. Electroanal. Chem.*, vol. 690, pp. 136–143, 2012.

[95] J. E. Hoffmann, K. Bedner, H. Clemens, R. Degen, C. Dhum, F. Giro, U. Kirsch, M. Schmitt, and M. Saumer, "The influence of the electroplating parameters on the conditions of deposited nickel-iron coatings," *Materwiss. Werksttech.*, vol. 39, no. 3, pp. 209–216, 2008.

[96] Y. Yao, J. Rodriguez, J. Cui, A. Lennon, and S. Wenham, "Uniform plating of thin nickel layers for silicon solar cells," *Energy Procedia*, vol. 38, pp. 807–815, 2013.

[97] Z. Ghasempour and S. M. Rozati, "Characterization of nanostructure black nickel coatings for solar collectors," in *World Renew. Energy Congr.*, pp. 3985–3990, 2011.

[98] D. P. Arnold, I. Zana, F. Cros, and M. G. Allen, "Vertically laminated magnetic cores by electroplating Ni-Fe into micromachined Si," *IEEE Trans. Magn.*, vol. 40, no. 4, pp. 3060–3062, 2004.

[99] L. D. V. Llona, H. V. Jansen, and M. C. Elwenspoek, "Seedless electroplating on patterned silicon," *J. Micromechanics Microengineering*, vol. 16, no. 6, pp. S1–S6, 2006.

[100] D. Sander, R. Hoffmann, V. Relling, and J. Mueller, "Fabrication of metallic microstructures by electroplating using deep-etched silicon molds," *J. Microelectromechanical Syst.*, vol. 4, no. 2, pp. 81–86, 1995.

[101] J. Gobet, F. Cardot, J. Bergqvist, and F. Rudolf, "Electrodeposition of 3D microstructures on silicon," *J. Micromechanics Microengineering*, vol. 3, no. 3, pp. 123–130, 1999.

[102] J. Kouba, M. Kubenz, A. Mai, G. Ropers, W. Eberhardt, and B. Loechel, "Fabrication of Nanoimprint stamps for photonic crystals," *J. Phys. Conf. Ser.*, vol. 34, pp. 897–903, 2006.

[103] X. Lin, X. Dou, X. Wang, and R. T. Chen, "Nickel Electroplating for Nanostructure Mold Fabrication," *J. Nanosci. Nanotechnol.*, vol. 11, no. 8, pp. 7006–7010, 2011.